Interactions between a solitary semi-arid forest
and the Atmospheric Boundary Layer

Zur Erlangung des akademischen Grades eines
DOKTORS DER NATURWISSENSCHAFTEN
von der Fakultät für
Bauingenieur-, Geo- und Umweltwissenschaften

des Karlsruher Instituts für Technologie (KIT)
genehmigte
DISSERTATION
von
M.Sc. Peter Brugger
aus Heilbronn

Tag der mündlichen
Prüfung: 26. November 2018

Referent: Dr. Matthias Mauder

Korreferent: Prof. Dr. Jan Cermak
Korreferent: Prof. Dr. Dan Yakir

Karlsruhe (2018)

Summary

Semi-arid forests are expected to become more important in the future due to predicted warming and drying trends for parts of the global land area and due to afforestation efforts in the Mediterranean region. To model the climate impact of these ecosystems correctly, it is important to understand their surface-atmosphere interactions. Therefore, the underlying driving mechanisms of the surface-atmosphere exchange for heat and momentum of semi-arid forests and their impact on the atmospheric boundary layer are explored within this PhD thesis. Meteorological field measurements at the isolated, semi-arid Yatir forest (length of 7 km in main wind direction, area 2800 ha) in Israel are used to achieve this goal.

The field campaign entailed three measurement sites: one located in the shrubland upwind of the forest, one at the center of the forest, and one downwind of the forest. The upwind and forest site were equipped with an ultrasonic anemometer and a Doppler lidar each. A ceilometer was deployed at the downwind site. Information about the turbulence structure, the turbulent transport efficiency and energetics, the wind speed and direction, and the boundary-layer height were extracted from those measurements.

The results showed that the canopy sublayer of the forest has a more isotropic turbulence structure compared to the surface layer of the upwind shrubland at the large turbulence-producing scales. While isotropic turbulence is expected to be less efficient at transporting momentum, the forest was observed to have a more energetic and more efficient momentum transport compared to the shrubland. This was explained with higher vorticity due to the larger roughness of the canopy leading to a larger velocity gradient. These turbulence properties of the forest lead to a sensible heat flux which is driven by stronger turbulence, but not a more efficient transport process of heat. This separation of processes contributing to the sustainment of a larger turbulent flux for a given mean gradient in the canopy sublayer compared to the surface layer (which was already known previously in literature) allows to identify the important processes for modelling purposes. In case of the sensible heat fluxes at the Yatir forest the effect of the modified turbulence structure was more than five times smaller than the effect of the more energetic turbulence.

The impact of the higher momentum and heat fluxes of the forest on the atmospheric boundary layer was investigated. It was observed that the forest increased the depth of the atmospheric boundary layer unless suppressed by a strongly stable stratification of the free atmosphere. This magnitude of the increase could be related to the forest dimensions, because the time for the atmospheric boundary layer to adapt depended on the wind speed and the size of the forest in upwind direction. Further, the results showed a wind speed maximum in the afternoon due to the sea-breeze, which delayed the peak time of the diurnal cycle for turbulence statistics associated with mechanical production. In contrast turbulence statists associated with buoyant production had their peak closer to the maximum surface heating from the net radiation at the local noon time. Lastly, indicators of an earlier formation of a residual layer above the forest compared to the shrubland were observed. This was explained with the importance of the mechanical turbulence production for the cooling of the forest in combination with the late wind speed maximum and the advection of a warmer boundary layer from the shrubland.

Zusammenfassung

Aufgrund von vorhergesagten Trends zur Erwärmung und Trockenheit für Teile der globalen Landoberfläche und Aufforstungsmaßnahmen im mediterranen Raum ist zu erwarten, dass semi-aride Wälder in Zukunft an Bedeutung gewinnen. Um die Auswirkungen dieser Ökosysteme auf das Klima korrekt zu modellieren, ist es wichtig, deren Wechselwirkungen zwischen Atmosphäre und Oberfläche zu verstehen. Daher wurden in dieser Doktorarbeit die zugrunde liegenden Mechanismen des Austausches von Wärme und Impuls zwischen Oberfläche und Atmosphäre für semi-aride Wälder untersucht und deren Auswirkungen auf die atmosphärische Grenzschicht. Meteorologische Messungen am isolierten, semi-ariden Yatir Wald in Israel (7 km Ausdehnung in Hauptwindrichtung, Fläche 2800 ha) werden verwendet, um diese Ziele zu erreichen.

Die Messkampagne beinhaltete drei Messstandorte: einer im Luv des Waldes in einer Dornensavanne, einer im Zentrum des Waldes und einer im Lee des Waldes. Der Luv- und Waldstandort waren jeweils mit einem Ultraschallanemometer und einem Doppler Lidar ausgestattet. Am Leestandort wurde ein Ceilometer eingesetzt. Aus diesen Messungen wurden Informationen über die Turbulenzstruktur, die turbulente Transporteffizienz und Energetik, die Windgeschwindigkeit und Richtung sowie die Grenzschichthöhe abgeleitet.

Die Ergebnisse zeigen, dass die großen turbulenzgenerierenden Skalen am Waldstandort eine isotropere Turbulenzstruktur im Vergleich zur Dornensavanne haben. Während zu erwarten ist, dass isotrope Turbulenz weniger effizient im Transport von Impuls ist, wurde am Waldstandort trotzdem ein energetischerer und effizienterer Impulstransport beobachtet. Dies wurde mit einer größeren Wirbelstärke aufgrund der größeren Rauigkeit des Waldes und daraus resultierendem größeren Windgeschwindigkeitsgradienten erklärt. Diese Turbulenzeigenschaften des Waldes führen zu einem fühlbaren Wärmestrom, der durch stärkere Turbulenz, aber nicht durch einen effizienteren Transportprozess erzeugt wird. Diese Separierung der Prozesse für die Erhaltung von größeren turbulenten Flüssen für einen gegebenen mittleren Gradienten am Waldstandort im Vergleich zur Dornensavanne (was in der Literatur schon bekannt war) erlaubt die Identifizierung der wichtigen Prozesse für Modellierungsanwendungen. Im Fall der fühlbaren Wärmeströme am Yatir Wald ist der Effekt einer modifizierten Turbulenzstruktur mehr als fünf mal kleiner als der Effekt durch energetischere Turbulenz.

Die Auswirkung des größeren Impuls- und fühlbaren Wärmestroms des Waldes auf die atmosphärische Grenzschicht wurde untersucht. Es wurde beobachtet, dass der Wald die Tiefe der Grenzschicht vergrößert, es sei denn, der Effekt wurde durch eine stark stabile Schichtung der freien Atmosphäre unterdrückt. Die Höhe der Grenzschichtvertiefung konnte zu den Ausmaßen des Waldes in Verbindung gesetzt werden, weil die Zeit zur Anpassung der Grenzschicht an den Wald von der Windgeschwindigkeit und der Größe des Waldes in Windrichtung abhing. Des Weiteren zeigten die Ergebnisse die höchsten Windgeschwindigkeiten am Nachmittag aufgrund eines Seewindes, welcher die Tagesgangspitzen von Turbulenzstatistiken, die der mechanischen Produktion nahestehen, verzögerte. Dagegen haben Turbulenzstatistiken, die der Produktion durch Auftrieb nahestehen, ihre Tagesspitzen dichter am lokalen Mittag während der maximalen Strahlungsbilanz und damit verbundener Bodenerwärmung. Zuletzt wurden Hinweise auf die frühere Bildung einer Restluftschicht über dem Wald im Vergleich zur Dornensavanne beobachtet. Dies wurde durch die Bedeutung der

mechanischen Turbulenzproduktion für den fühlbaren Wärmestrom am Wald in Kombination mit dem späten Windgeschwindigkeitsmaximum und der Advektion einer wärmeren Grenzschicht von der Dornensavanne erklärt.

Acknowledgments

I am very grateful to all the people who supported me with my work and during my time in Garmisch-Partenkirchen. In particular I want to address special thanks to:

Dr. Matthias Mauder for his excellent mentoring during my PhD and introducing me to the scientific community by allowing me to participate in conferences and field campaigns. You have been a great supervisor finding the balance between the freedom to pursue own ideas and keeping things on track.

Prof. Dan Yakir and Prof. Jan Cermak for reviewing this thesis. And to the CliFF project partners, Prof. Almut Arneth, Dr. Matthias Mauder, Dr. Eyal Rotenberg, Dr. Nadine Rühr, Prof. HaPe Schmid, and Prof. Dan Yakir, who made this PhD possible.

To my co-authors Dr. Tirtha Banerjee, Dr. Frederik de Roo, Konstantin Kröniger, Dr. Matthias Mauder, Dr. Eyal Rotenberg, Rafat Qubaja, Dr. Eyal Rotenberg, Shani Rohatyn, Dr. Feodor Tatarinov, Prof. Dan Yakir, and Dr. Matthias Zeeman for their thoughts and ideas, supporting the measurements and sharing data, and their comments that improved my manuscripts.

Prof. Gabriel G. Katul for his excellent advice and insightful discussions during his stay as visiting scientist at the IMK-IFU. I learned a lot from the exchange with you and gained a level of understanding in turbulence dynamics, which I would not have reached otherwise.

Konstantin Kröniger and Dr. Frederik de Roo for their valuable inputs throughout my PhD. Working together with you was a very enjoyable and enlightening experience.

Colleagues from the TABLe working group, the IMK-IFU, and from the the Ecophysiology group at the Department of Earth and Planetary Sciences of the Weizmann Institute of Science. This was an very inspiring environment to work in and being exposed to so many different research fields was very interesting.

My friends from the Hans-Freudenberger-Kolleg (HFK), former fellow students, and the cooking group for enriching the social aspects of my time in Garmisch-Partenkirchen.

An meine Familie, Anja and Klaus, die stets für mich da waren. Vorallem in schwierigen Zeiten, wenn alles turbulent und unsicher ist, gibt ein fester Bezugspunkt im Leben Halt, Geborgenheit und Sicherheit.

Contents

1 Introduction

Incoming solar radiation that is absorbed at the earth's surface is the driver for the global circulation (Barry and Chorley, 2003). The interface between the surface and the global circulation in the free atmosphere ist the atmospheric boundary layer (ABL). The ABL is also home to the land based flora and fauna, which gives rise to a complex system where the ABL both influences and responds to the ecosystem, while at the same time the ABL interacts with the global circulations patterns. This thesis will investigate the surface-atmosphere interactions of semi-arid forests and the following section will introduce important elements of this complex system and motivate the research questions.

1.1 Semi-arid forests

Forests in semi-arid regions influence the Earth's climate through modifying CO_2 and surface radiation budgets (Rotenberg and Yakir, 2010). Cooling effects by carbon sequestration and increased cloud cover are contrasted by warming effects due to higher surface radiation budgets and humidity (Betts, 2000; Rotenberg and Yakir, 2011), resulting in decades of carbon uptake needed to balance radiation effects (Rotenberg and Yakir, 2010). The significance of these semi-arid ecosystems could increase in the future due to predicted warming and drying trends for parts of the global land area (Burke et al., 2006) and due to afforestation efforts in the eastern Mediterranean (Sprintsin et al., 2009). However, these semi-arid forests are confronted with a large net radiation, due to high amounts of incoming radiation and a low albedo, while simultaneously the restricted water availability during the summer dry season prevents evaporative cooling. Their survival relies on generating a turbulent transport of heat to the overlying atmosphere, while maintaining a low surface (skin) temperature (Rotenberg and Yakir, 2011). A process coined canopy convector effect by Rotenberg and Yakir (2010) and hypothesized as an reduced aerodynamic resistance of semi-arid forest canopies. Therefore, a detailed investigation of the underlying physical processes, which contribute to the canopy convector effect, and their interaction with the environment conditions is important for understanding and modelling these dry ecosystems.

The evergreen Yatir pine forest, located in southern Israel to the west of the Dead Sea and north of the Negev desert, is an example of such a semi-arid ecosystem (Fig. 1). It is a planted forest covering an area of approximately 28 km^2, with a length of 7 km in the main wind direction, and *Pinus halepensis* as the predominant tree species (Rotenberg and Yakir, 2011). The climate is semi-arid with an annual mean precipitation of 285 mm and an annual positive net radiation of 238 W m^{-2} (Rotenberg and Yakir, 2011). The Yatir forest has a mean height of 662 m above sea level, with its lowest areas at 500 m and highest at 850 m. The older north-western parts of the forest with tree heights of around 11 m were planted from 1964–1969, and planting has continued since. Further, the forest is an isolated heterogeneity for albedo and roughness compared with the surrounding shrubland. The albedo of the forest is 0.13 compared with 0.34 for the shrubland (Rotenberg and Yakir, 2011). The shrubland consists of scattered herbaceous annuals and perennials (mainly *Sarcopoterium spinosum*) with heights ranging from 0.3–0.5 m. During the summer dry season, this leads to sensible heat fluxes of up to 600 W m^{-2} during midday, and friction velocities of 0.8 m s^{-1} over the forest canopy, which are twice as high as those of the surrounding shrubland (Eder et al., 2015).

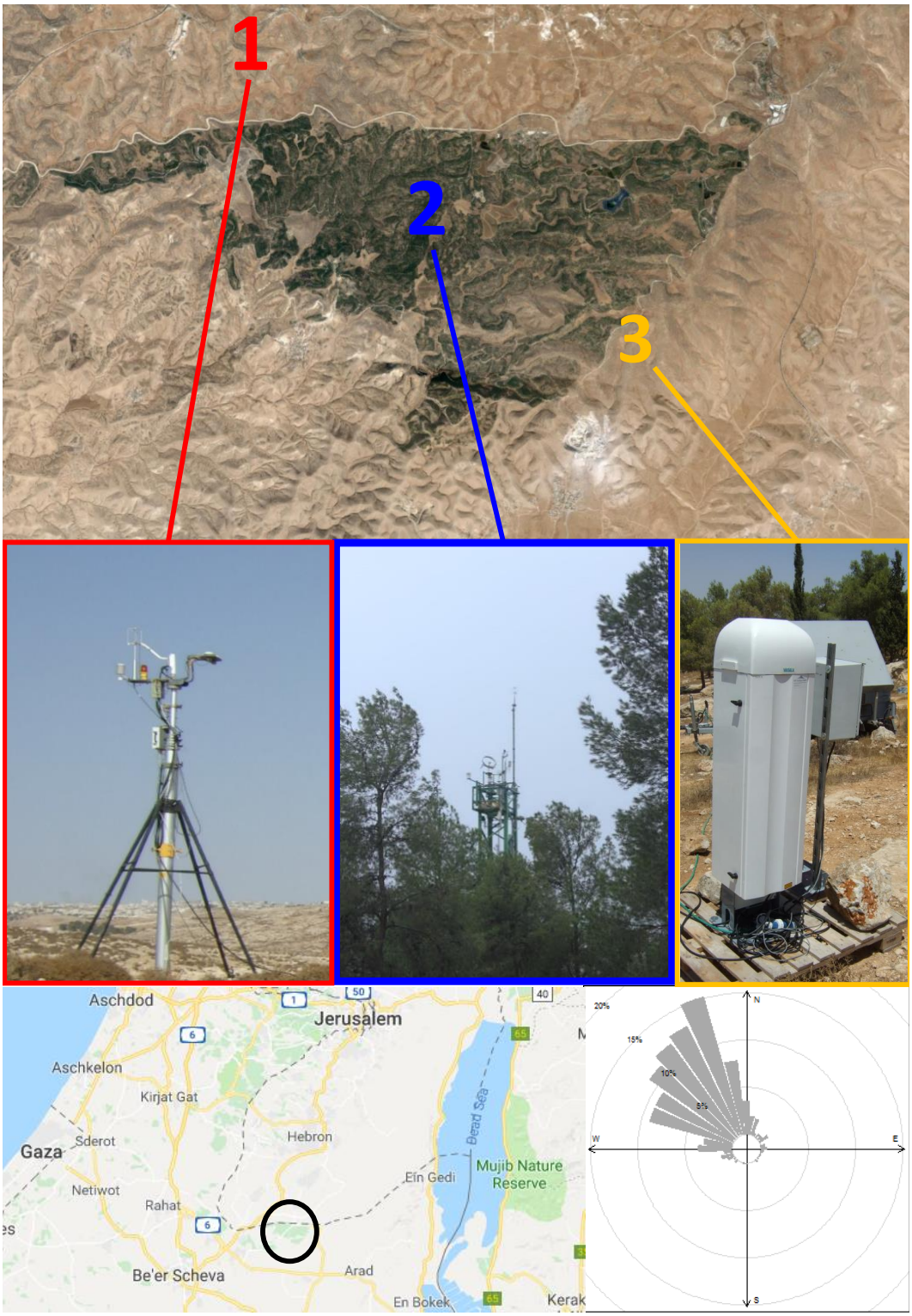

Figure 1: Top: Satellite image of Yatir forest in Israel at the northern edge of the Negev desert with the location of the shrubland site (1, red), forest site (2, blue) and downwind site (3, orange). Middle left to right: photos of the two eddy-covariance stations and the ceilometer. Bottom left to right: Map of the area between Dead Sea and Mediterranean Sea with the location of Yatir forest indicated with a black circle, frequency-of-occurrence wind-rose of the 300 m a.g.l. wind speed from Doppler lidar measurements at the forest site. Source of satellite image and map: Google.

1.2 Atmospheric boundary layer

The ABL is the lowest part of the troposphere that is directly influenced by the Earth's surface and responds to surface forcings with a time scale of about an hour or less (Stull, 1988). The ABL controls the exchange of heat, momentum and pollutants between the free atmosphere and the Earth's surface. Key characteristics distinguishing an ABL over land from the overlying free atmosphere are diurnal variations and turbulence, with the latter being responsible for most of the vertical transport within the ABL.

Concepts of the convective ABL distinguish three layers (Stull, 1988): the surface layer, the mixed layer, and the entrainment zone. The surface layer extends from the surface up to 10-15% of the ABL height, where fluxes are assumed in theory to be constant with height, which is also approximately the case in measurements, too (Aubinet et al., 2012). Further, the surface layer is the region, where the logarithmic wind profile applies and Monin-Obukhov similarity theory is assumed to be valid. The mixed layer is above the surface layer and makes up the bulk of the ABL. It has usually convective turbulence with warm air rising, driven by solar heating of the ground, which mixes heat, moisture, and momentum uniformly in the vertical. The upper most layer and interface to the free atmosphere is the entrainment zone with a statically stable stratification. It is characterised by entrainment of free atmosphere air downward and overshooting thermals upward, which lead to spatial and temporal variations of the top of the entrainment zone. The ABL height is defined as the level where on average 50% of the air has free atmosphere characteristics.

If the surface has a canopy, a fourth conceptual layer is introduced, the canopy sublayer, which is below the surface layer. The turbulent exchange within the canopy sublayer features a dominant eddy structure of two linked hairpin-vortices (Finnigan et al., 2009), which facilitates a more efficient transport of momentum and scalars, supported by weaker mean gradients compared to the atmospheric surface layer (Raupach, 1979; Raupach et al., 1996). Furthermore, the canopy sublayer is characterised by an inflection point in mean velocity profile at the canopy top (h_c) , a decay of second order moments within the canopy towards the surface, and larger streamwise and vertical skewnesses, compared to the surface layer, up to a height of $2h_c$ (Katul et al., 2013).

1.3 Turbulence and transport

Turbulent flows feature eddies of many scales, which lead to a velocity field that varies significantly and irregularly in both position and time (Pope, 2000). The random nature of turbulent flows requires a statistical description. Assuming a spectral gap that separates turbulence from diurnal and synoptical motions (Van der Hoven, 1957), a flow variable $x(\mathbf{r}, t)$ at a point $\mathbf{r}$ and time t can be decomposed into

$$x(\mathbf{r}, t) = \overline{x(\mathbf{r}, t)} + x'(\mathbf{r}, t), \tag{1}$$

where $\overline{x(\mathbf{r}, t)}$ is mean flow and $x'(\mathbf{r}, t)$ is the turbulent fluctuations (Reynolds, 1895). In the framework of this thesis, the ergodic hypothesis is assumed, i.e. the ensemble average is equal to the temporal and spatial average.

Applying the Reynolds decomposition and averaging on the Navier-Stokes equations yields the governing equations of the mean flow, which then include the Reynolds stress tensor $\overline{u_i' u_j'}$ with u_1

(or u), u_2 (or v), and u_3 (or w) the velocity components in direction of the Cartesian coordinate axes. (Reynolds, 1895). These Reynolds stresses act like an additional friction on the flow and are responsible for turbulent mixing and transport. The diagonal components are normal stresses (associated with the turbulent kinetic energy) and the off-diagonal components are shear stresses (associated with the momentum transport).

The distinction between shear stresses and normal stresses depends on the choice of coordinate system. A fundamental distinction can be made between isotropic and anisotropic turbulence. Anisotropy is the differences in the kinetic energy distribution among the velocity components comprising the stress tensor and only the anisotropic part of the turbulence is effective at transporting momentum (Pope, 2000). The production of turbulence at large scales is anisotropic: buoyant production acts on the vertical component and mechanical production on the horizontal components (or the streamwise component if the coordinate system is aligned with the mean wind direction). With progressing time (or towards smaller scales) the energy is redistributed to the other components by pressure perturbations until the turbulence becomes isotropic (Lumley and Newman, 1977). Further, Reynolds stresses arising from a vorticity free flow field have the same effect as isotropic stresses and, therefore, only stresses arising from a rotational flow field produce a turbulent transport and affect the mean velocity field (Pope, 2000). The main source of vorticity in the ABL is the wind shear that develops between the geostrophic wind above the ABL and the zero wind speed at the surface.

The vertical exchange in the ABL is nearly exclusively a turbulent transport (unlike horizontal transport, where advection is important) (Stull, 1988). Similar as for momentum, a conserved passive scalar ψ is transported and mixed by turbulence. Defining a plane parallel to a flat, level and homogeneous surface the turbulent flux through this plane given by the covariance $\overline{w'\psi'}$ (if the assumptions for the surface are met and there are no sources or sinks between the plane and the surface, then this flux is the surface-atmosphere exchange, which is the principle of the eddy-covariance technique (Kaimal and Finnigan, 1994)).

The turbulent fluxes appearing in the governing equations of the mean flow are giving rise to the closure problem: prescribing the turbulent fluxes with mean values. Based on experimental experience and in analogy to molecular diffusion in laminar flows, gradient-diffusion approximations assume this turbulent flux to be proportional to the gradient of the mean value (Kaimal and Finnigan, 1994). While shortcomings of this approach have been pointed out in literature (e.g. Pope, 2000), it is nevertheless a frequently used closure method in combination MOST for weather forecast models (e.g. the Integrated Forecasting System of the European Centre for Medium-Range Weather Forecasts). Further simplification with a constant flux approximation lead to aerodynamic resistance approaches in analogy to Ohm's Law (Liu et al., 2007). This approach yields in case of the kinematic sensible heat flux

$$\overline{w'T'} = \frac{\overline{T}_s - \overline{T}_a}{r_H}, \tag{2}$$

where $\overline{T}_s - \overline{T}_a$ is the difference between surface and air temperature, and r_H the aerodynamic resistance to heat transfer.

1.4 Research questions

The overarching objective of this thesis is to understand the drivers of the enhanced surface-atmosphere exchange of a semi-arid forest and their interactions with the ABL above the forest. This was investigated with three research objectives:

1. To what extent does the Yatir forest affect the local ABL, including changes in turbulence structure compared to non-forested area, boundary-layer height, and diurnal variations?

2. What are micrometeorological drivers of the canopy convector effect? Are they affected by locally characteristic sea breeze and associated high wind speeds?

3. Can the extent of the forest effects on the ABL characteristics be related to the forest dimensions?

Answers to those questions are provided by the two publications and a manuscript draft comprising this cumulative thesis (appendix B to D) and presented here in a bottom-up approach:
First, the turbulence structure at the forest and the shrubland is investigated in terms of anisotropy across scales, because the effectiveness of the turbulent momentum transport is connected to the deviatoric or anisotropic portion of the Reynolds stress tensor.
Second, the vertical transport of momentum and heat is analyzed in terms of efficiency and energetics (defined in section 2.3.3) for the Yatir forest and its surrounding shrubland to understand the micrometeorological mechanisms of the canopy convector effect and their interaction with the diurnal cycle and sea-breeze.
Third, the ABL height upwind, within, and downwind of the Yatir forest is analyzed to investigate if a forest of Yatir's size can modify the whole depth of the ABL and whether those effects can be related to the forest size or synoptic environment conditions.

2 Methods

The research questions are answered with results from field experiments conducted at the Yatir forest with Doppler lidars, a ceilometer, and ultrasonic anemometers. The instruments and post processing steps are introduced in this section.

2.1 Measurement setup at the Yatir forest, Israel

Three measurement sites were setup along the main wind direction (Fig. 1):

1. A site in the shrubland upwind of the Yatir forest (latitude $31.3757°$, longitude $35.0242°$, 620 m above sea level) to probe the ABL with a Doppler lidar and eddy-covariance station without disturbance from the forest.

2. A site in the oldest and densest past of the forest (latitude $31.3453°$, longitude $35.0522°$, 660 m above sea level) to investigate the effect of the forest on the ABL with a Doppler lidar and eddy-covariance station.

3. A site at the downwind edge of the forest (latitude $31.3258°$, longitude $35.0838°$, 780 m above sea level) to capture an advected ABL height increase with a ceilometer.

The measurements were conducted during the summer dry season (16–29 August 2015). The synoptic scales were controlled by the subtropical ridge, an area of large scale subsidence in the troposphere connected to the sinking branch of the Hadley cell (Barry and Chorley, 2003), and the Persian trough, a heat-induced surface low to the east (Dayan and Rodnizki, 1999). This lead to a main wind direction from the north-west and cloud free conditions, with a radiation-driven diurnal cycle of the ABL.

2.2 Instruments

2.2.1 Ultrasonic anemometer

The forest site was equipped with a R3-50 and the shrubland site with a R3-100 ultrasonic anemometers from Gill Instruments (Lymington, Hampshire, UK), which measure the sonic temperature (T) and the three components of the wind vector (u, v and w) from travel times of sound waves along the three transducer axes with a frequency of 20 Hz. The accuracy of both ultrasonic anemometers is given by the manucfacturer as $< 1\%$ for mean wind speeds below 32 m s^{-1}. Comparison to a hot-film anemometer in wind tunnel and atmospheric measurements showed an accuracy of 2% for the mean wind speed, 9% for variances, and 23% for covariances (Högström and Smedman, 2004). The ultrasonic anemometer at the forest site was mounted 19 m above the ground in the canopy sublayer (mean tree height at the site is 10 m, placing it 9 m above the canopy) and the instrument at the shrubland site was mounted in the surface layer 9 m above the ground until 23 August 2015 when it was raised to 15 m to increase the flux footprint.

2.2.2 Doppler lidar

Two Doppler lidars (Stream Line from Halo Photonics Ltd., Worcester, UK) were deployed together with the ultrasonic anemometer at the shrubland and the forest site. The systems emit lases pulses, which are scattered and Doppler shifted by aerosols in the atmosphere, and the backscattered radiation is detected (Werner, 2005). From the detected signal the line-of-sight velocity along the optical-axis is extracted. Both Doppler lidars were operated in a vertical stare mode, from which vertical velocity profiles with a frequency of 1 Hz and a resolution of 18 m were obtained, and every 30 min the system did a velocity-azimuth-display scan.

2.2.3 Ceilometer

A ceilometer (CL51 from Vaisala, Vantaa, Finland) was deployed at the downwind edge of the forest pointing vertically upwards to measure profiles of the backscatter coefficient. It was levelled with a spirit level and sampled at a temporal resolution of 16 s and a spatial resolution of 10 m.

2.2.4 Radiosonde

Temperature and pressure profiles from radiosonde launches at Beit Dagan (station number 40179; the distance from Yatir forest is approximately 75 km) were consulted via a web portal of the University of

Wyoming. The launches were done by the Israel Meteorological Service using a RS92/DigiCORA II radiosonde from Vaisala (Vantaa, Finnland). The accuracy of the radiosonde is 0.5 K for the temperature, 1 hPa for the pressure and 20 m for the height in the lower atmosphere based on the results of a World Meteorological Organization inter-comparison of radiosondes in Yangjiang, China.

2.3 Post-processing

2.3.1 Turbulence statistics

A quality control scheme was applied to the ultrasonic anemometer raw data and turbulence statistics at 30-min intervals were computed. This was done with the TK3 software (Mauder and Foken, 2015), which includes despiking (Mauder et al., 2013), unit conversions (Schotanus et al., 1983), a transformation of the coordinate system according to the planar-fit method (Wilczak et al., 2001), and block averaging. The quality control scheme included steady-state tests and integral turbulence characteristic tests (Foken and Wichura, 1996), after which we discarded low-quality 30-min intervals based on the flag system of Mauder et al. (2013).

In a second step, the high-frequency data of the intervals that passed quality control (after removing unphysical values, despiking, linear interpolation of gaps up to cummulative gap length of 1%, coordinate rotation, and demeaning) was further processed to compute measures of anisotropy (section 2.3.2) and turbulent transport efficiencies and energetics (section 2.3.3). Data which was used to study the anisotropy had to have a quality flag of zero and data used to study the diurnal cycle was accepted with quality flag of one as well.

2.3.2 Invariants of the Reynolds stress tensor

The anisotropy tensor is powerful framework to study the turbulence structure introduced by Lumley and Newman (1977). The normalized anisotropy tensor is given by

$$a_{ij} = \frac{\overline{u_i' u_j'}}{2k} - \frac{1}{3}\delta_{ij} \tag{3}$$

with $\overline{u_i' u_j'}$ the Reynolds stress tensor (introduced in section 1.3), $k = \frac{1}{2}\Sigma_i \overline{u_i' u_i'}$ the turbulent kinetic energy, and δ_{ij} the Kronecker symbol. The anisotropy tensor is a symmetric and positive semi-definite second-rank tensor and, therefore, has three real eigenvalues (λ_i) independent of the rotation of the reference system (Banerjee et al., 2007). The eigenvalues are obtained by diagonalizing a_{ij} and are ordered by their magnitude ($\lambda_1 > \lambda_2 > \lambda_3$). Using these eigenvalues all turbulence states can be mapped on a finite 2D area in terms of the three principle anisotropy states: 1-component (rodlike energy distribution), 2-component (disklike energy distribution), and 3-component (spherical energy distribution or isotropic state). These maps are called anisotropy invariant maps and can be visualized in a barycentric map (BAM) as shown in Fig. 2. The coordinates of a turbulence state within the BAM

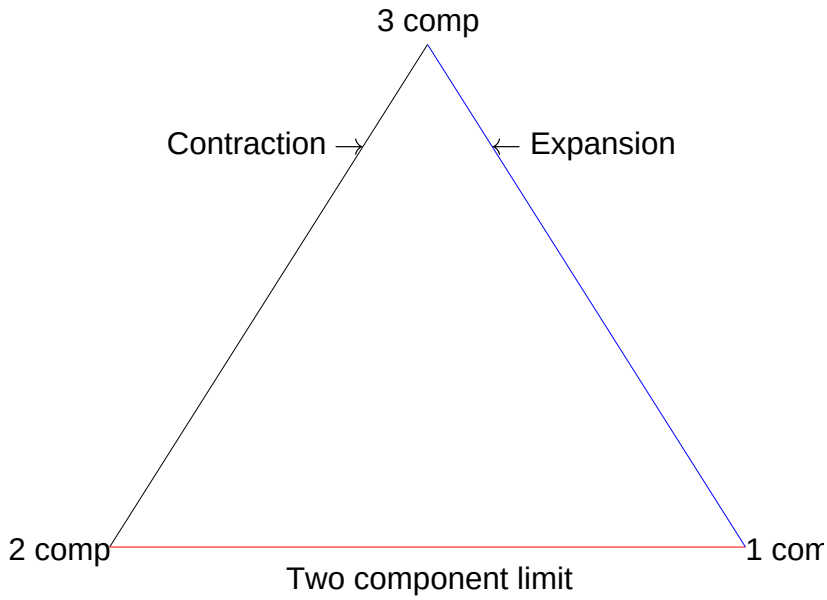

Figure 2: Barycentric map of invariants of the anisotropy tensor. The top of the triangle is the isotropic state (3 comp), the bottom left is 2D turbulence (2 comp), and the bottom right is the 1D turbulence (1 comp).

are computed with

$$C_{1c} = \lambda_1 - \lambda_2 \tag{4}$$

$$C_{2c} = 2\left(\lambda_2 - \lambda_3\right) \tag{5}$$

$$C_{3c} = 3\lambda_3 + 1, \tag{6}$$

and

$$x_{BAM} = C_{1c}x_{1c} + C_{2c}x_{2c} + C_{3c}x_{3c} \tag{7}$$

$$y_{BAM} = C_{1c}y_{1c} + C_{2c}y_{2c} + C_{3c}y_{3c}, \tag{8}$$

where $(x_{1c}, y_{1c}) = (1, 0)$, $(x_{2c}, y_{2c}) = (-1, 0)$, and $(x_{3c}, y_{3c}) = (0, \sqrt{3})$ are the coordinates of the three limiting states (Banerjee et al., 2007). The vertical distance to the isotropic state

$$C_{ani} = -3\lambda_3 \tag{9}$$

is a scalar measure to describe the deviation from the isotropy state. Both, the BAM representation of the turbulence and C_{ani} were computed across scales assuming Taylor's frozen turbulence hypothesis (Taylor, 1938). A more detailed description of this method is presented in Brugger et al. (2018b) (appendix C).

2.3.3 Turbulent transport efficiency and energetics

The phase difference ϕ_{xy} and the amplitude A_{xy} were computed as proxies for the turbulent transport efficiency and the energetics for small and large eddies separately. The decomposition of small and large eddies was done by computing the Fourier transform and the associated power spectrum. Subsequently, Fourier coefficients of frequencies with less energy than mean energy of the time series were set to zero and the time series of large eddies was gained by applying the inverse Fourier transform. The time series of small eddies was then obtained as the residual of between large eddies and the original time series. Then, ϕ_{xy} and A_{xy} were computed for small and large eddies separately from the Hilbert cross-spectrum HCS_{xy} of two turbulent quantities x and y with

$$A_{xy} = \overline{(\Im(HCS_{xy}(t))^2 + \Re(HCS_{xy}(t))^2)^{1/2}} \tag{10}$$

and

$$\phi_{xy} = \overline{|\arctan\left(\frac{\Im(HCS_{xy}(t))}{\Re(HCS_{xy}(t))}\right)|}, \tag{11}$$

where $\Im$ and $\Re$ denote the imaginary and real part respectively (a more detailed description is presented in the manuscript draft in appendix D). ϕ_{xy} is a proxy for the transport efficiency e_t defined as $e_t = |(F_{direct} - F_{back})F_{direct}^{-1}|$ where F_{direct} is the accumulation of all events in the flux contributing quadrants and F_{back} the accumulation of the opposing quadrants (Francone et al., 2012). $\phi_{xy} \neq 0$ introduces time lags between x and y, which increases contributions from opposing quadrants, and weakens the correlation (Gao et al., 2017). A_{xy} is correlated to $\sigma_x\sigma_y = \overline{x'y'}r_{xy}^{-1}$, where σ is the standard deviation and r is the correlation coefficient, and therefore a measure of the transport energetics or hypothetical strength, independent of the efficiency or the phase difference between x and y (Stull, 1988). Further details on this method are given in the manuscript draft in appendix D.

2.3.4 Horizontal wind and vertical velocity variance profiles

Half-hourly profiles of the horizontal wind speed and direction were computed from the velocity-azimuth-display scans of the Doppler lidars with the algorithm of Browning and Wexler (1968). Profiles of the vertical velocity variance at 30 min intervals were computed from vertical stares of the Doppler lidars. To remove low quality data 15000 pulses per estimate were averaged and range gates with a signal-to-noise ratio < -17 dB or below 60 m were discarded.

2.3.5 Atmospheric boundary-layer height detection

The ABL height (z_i) was detected from the backscatter coefficient profiles of the Dopper Lidars and the Ceilometer with the gradient method as outlined in Münkel et al. (2007). This method detects the ABL height by a drop of the backscatter coefficient between the aerosol laden ABL and the clean free atmosphere. The backscatter coefficient profiles were first range corrected, vertically smoothed and noise at large distances was cut off. Then the height of the largest three negative gradients above a threshold were computed for each backscatter profile. The most frequent heights within a ten minutes interval were detected as aerosol layer heights. In case of the Ceilometer data this processing was done with the BLMatlab software version 1.9 (by courtesy of C. Münkel). The time series of the

ABL heights was then computed by selecting the lowest detected aerosol layer for each time step, then filtering outliers by removing values smaller than 100 m or larger than 2500 m or differed more than 200 m from the moving average of one hour (Lotteraner and Piringer, 2016).

2.3.6 Static stability of the free atmosphere

Information of the thermal stratification of the free atmosphere above the ABL was extracted from radiosonde launches at Beit Dagan. After detecting the ABL height with the parcel method (Seibert et al., 2000), the vertical potential temperature gradient ($\Delta\theta$) of a 500 m layer above the ABL was computed (more details in appendix B). It is assumed that the $\Delta\theta$ at Beit Dagan is representative for the free atmosphere at the Yatir forest, because the horizontal variations of the free atmosphere on a distance of 100 km in the subtropics is small (Barry and Chorley, 2003).

3 Results and discussion

The surface-atmosphere interactions of the Yatir forest are investigated starting with the turbulence structure that controls the turbulent transports, followed by analysing the turbulent transports efficiency and energetics, and lastly, the impact of the forest on the ABL is investigated. This section compiles an overview of the results from the publications and manuscript draft in appendix B–D.

3.1 Turbulence structure at Yatir forest and the surrounding shrubland

The effectiveness of the turbulent momentum transport depends on the anisotropy of turbulence (section 1.3), which is presented in following with an extract of the results from Brugger et al. (2018b). A comparison of the normalized anisotropy tensor components (Eq. 3) of the canopy sublayer of the Yatir forest and the atmospheric surface layer of the surrounding shrubland is shown in Fig. 4. Both sites feature strong isotropy between the vertical component and the horizontal components with the larger anisotropy at the shrubland compared to the forest (Fig. 4a-c, note: $a_{11} + a_{22} = -a_{33}$). The scatter of a_{11} and a_{22} increases with unstable stratification, which can be explained with fluctuations of the wind direction for strongly unstable conditions leading to mechanical production in the cross-stream component. However, the anisotropy between both horizontal and the vertical components is not affected by the stratification and depends on the roughness only. The higher isotropy of the rougher forest is in agreement with direct numerical simulations (Isaza and Collins, 2009) and wind-tunnel experiments (Saddoughi, 1997). A (absolute) larger a_{13} with a significant stability dependency was observed at the Yatir forest, while a_{23} were around zero for both sites. The larger magnitude of a_{13} at the forest site are in agreement with the expectation for a rougher surface.

The anisotropy will be further investigated across scales. The starting points of the return-to-isotropy trajectories are consistent with the results of the bulk measures above (Fig. 4a and b). The return-to-isotropy across scales follows a contraction of the energy-ellipsoid towards the isotropic state. However, this process is not effective at all scales, which is an assumption of the frequently used Rotta model, but can be separated into three regimes (Fig. 4c and d). At large scales the turbulence remains at a constant level of anisotropy, which can be observed as a horizontal meandering of the

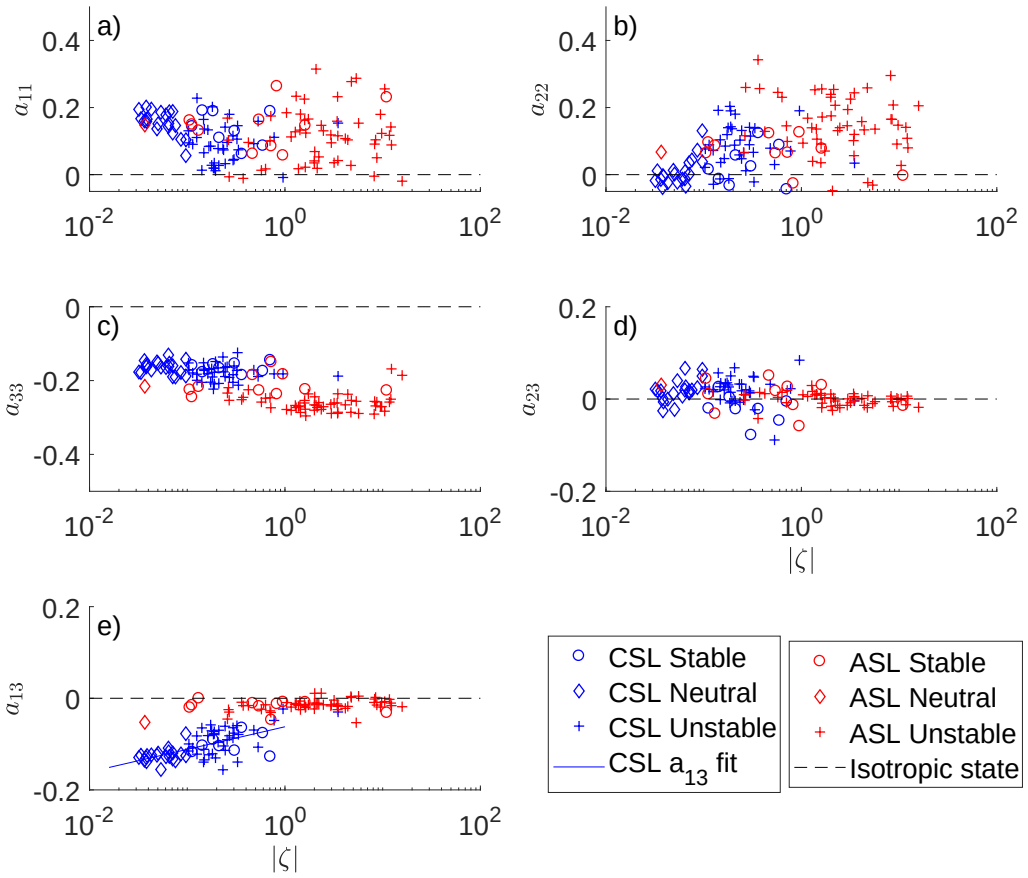

Figure 3: The measured components of the anisotropy tensor a_{ij} are shown as a function of the absolute value of the stability parameter $\zeta = zL^{-1}$ with L the Obukov length. Measurements of the shrubland site (ASL) are red and those of the forest site (CSL) are blue. Circles show stable conditions, diamonds are used for near neutral stratification conditions, and crosses denote unstable conditions. The a_{33} shown in panel (c) are significantly larger at the forest site compared to the shrubland site at a confidence level of 95%. The black dashed line shows the expected value for isotropic turbulence and the solid blue line in panel (e) shows a linear regression of a_{33} for the forest site. The ultrasonic anemometer data from 18–23 August 2015 was used, when both instruments were placed 9 m above the roughness elements. This figure is adapted from Brugger et al. (2018b) in appendix C.

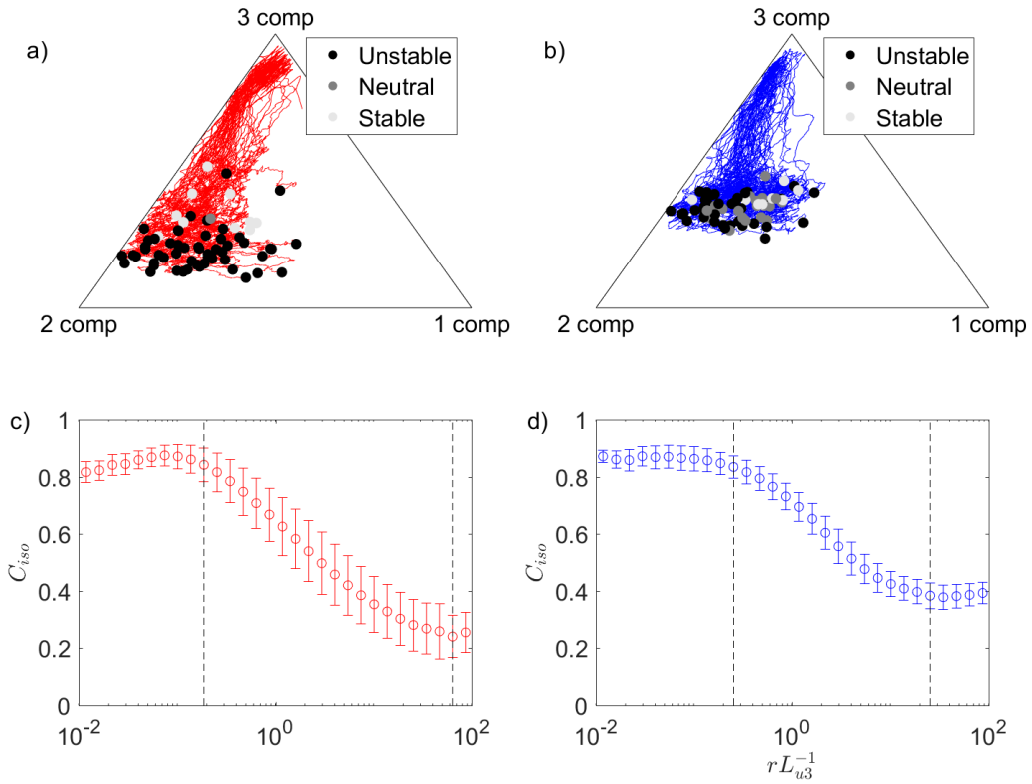

Figure 4: The top row shows the trajectories of the same 30 minute runs as in Fig. 4 for the shrubland (a) and the forest (b) together with starting points color coded according to their stability class (black is unstable, dark grey is near neutral, and light grey is stable). The bottom row shows C_{ani} (Eq. 9 – the vertical distance to the isotropic state in the BAM) as an ensemble average with standard deviation across all ζ for the shrubland (c) and the forest (d) to highlight the role of surface roughness. The black dashed lines show three regimes defined by reaching 90% of maximum isotropy or 10% of anisotropy. This figure is adapted from Brugger et al. (2018b) in appendix C.

trajectories in the BAM maps. At small scales the turbulence has constant, high levels of isotropy. An intermediate, finite scale range exists, where the return-to-isotropy takes place. This scale range is smaller for the forest site compared to the shrubland site.

3.2 Micrometeorological drivers of the canopy convector effect

The amplitudes (Eq. 10) and the phase differences (Eq. 11) of the vertical momentum and heat fluxes in the course of the diurnal cycle are investigated for small and large eddies. These results are extracted from the manuscript draft in appendix D. Here, the ultrasonic anemometer data from the 18–29 August 2015 was used to increase the ensemble size, because the results were not affected by the change in measurement height at the shrubland site. Superscripted s indicates small eddies and l large eddies.

For small eddies the turbulent transport of heat and momentum have the same efficiency at the shrubland and the forest, while the forest has the larger amplitudes (Fig. 5). The phase differences are explained by isotropic turbulence at small scales, which randomly distributes the phase shift be-

tween $0°$ and $90°$. It follows that larger fluxes at the forest site for small scales are generated by stronger turbulence, but not a more efficient transport process. This is in line with the similar small-scale anisotropy structure at both sites observed previously and follows the expectation of small-scale structures of turbulent motions being independent from large-scale structures and the mean velocity gradients if the Reynolds number is sufficiently high (Kolmogorov, 1941).

The diurnal cycles of amplitudes and phase differences for large eddies are shown in Fig. 6. The vertical transport of stream-wise momentum at large scales has larger amplitudes and smaller phase differences at the forest compared to the shrubland, indicating a more energetic and more efficient momentum transport over the forest canopy (Fig. 6a and 6b). Previously it was observed that the turbulence at the forest site is more isotropic at large scales, which opposes a more efficient momentum transport. Therefore, an explanation for this behaviour is sought in the vorticity, the second flow field quantity determining turbulent momentum transport (section 1.3). Assuming a logarithmic wind profile the mean wind shear ($\partial\overline{u}/\partial z$) increases with u_*, which is larger at the forest site (Fig. 7), and leads to higher shear vorticity at the forest site and then could explain the differences in ϕ^l_{uw} (stability effects not accounted yet). Further, a minor increase in ϕ^l_{uw} at the shrubland site around the local noon time (approx. 10 UTC) can be observed, while a minor decrease in ϕ^l_{uw} at the forest sites can be observed in the afternoon (Fig. 6b). This behaviour couldn't be explained, but a theory can be put forth considering that the turbulence production at the forest is strongly mechanical, while the production at the shrubland is carried by buoyant production (Banerjee et al., 2017): The decrease in ϕ^l_{uw} at the forest could be explained with a wind speed maximum in the afternoon (Fig. 10 and discussed in section 3.3.2) leading to a late u_* maximum (Fig. 7). The increase in ϕ^l_{uw} at the shrubland site could be explained with a stability effect on the curvature of the logarithmic wind profile, which would decrease $\partial\overline{u}/\partial z$ if the instrument was placed sufficiently high (Stull, 1988). These two effects would be exclusive to the respective site, because the large u_* at the forest site leads to more neutral stratification reducing a stability effect (compare Fig. 4). While at the shrubland site the mechanical turbulence production is less important (Banerjee et al., 2017), which reduces a response to the late wind speed maximum, but allowing for larger stability variations. However, wind speed measurements at multiple heights at the same time would be needed to verify this theory and the dead zone of the Doppler lidars is too large to be useful.

The sensible heat flux has larger amplitudes at the forest site, while the phase differences have similar values for both sites with a pronounced diurnal cycle (Fig. 6e and 6f). The decrease in ϕ^l_{wT} during the day could be explained by convective turbulence with rising warm air parcels, where positive w' and T' occur together. This result shows, that the canopy convector effect of the Yatir forest cannot be explained with a more efficient transport process for heat, but is solely generated by a more energetic transport due to stronger turbulence. Estimating the effect of the momentum transport energetics and efficiencies on the aerodynamic resistance r_H showed that the effect of energetics is more than five times larger compared to efficiency (details in the manuscript draft in appendix D). This finding allows to draw the conclusion, that stronger turbulence due to the higher roughness of the forest canopy is more important than changes in the turbulence structure.

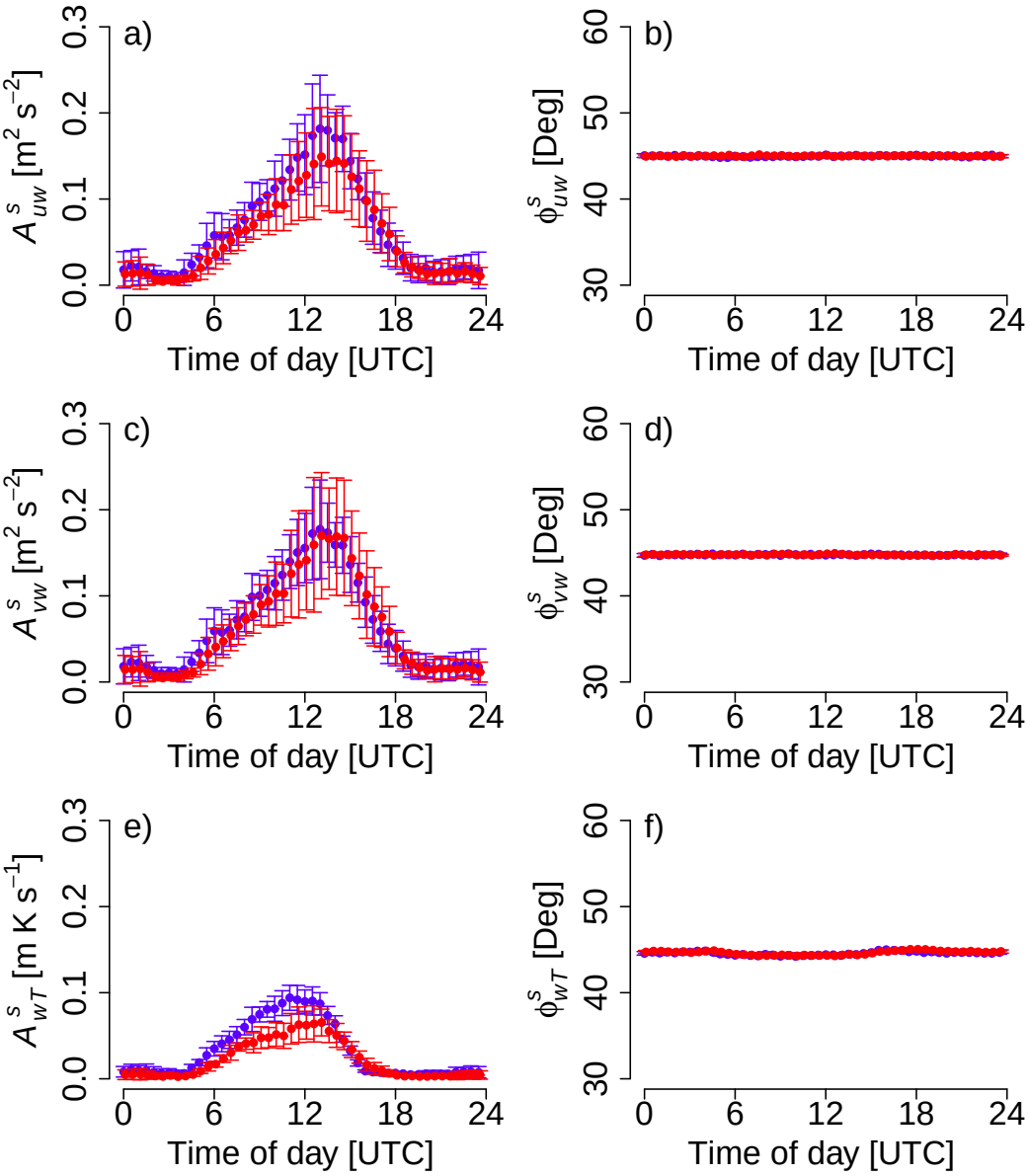

Figure 5: Comparison of the mean diurnal cycle of amplitude (left column) and phase difference (right column) for small eddies between forest (blue) and shrubland (red). The top row shows vertical transport of stream-wise momentum, the middle row the vertical transport of cross-stream momentum, and the bottom row the vertical transport of heat. The mean values are illustrated by points and the standard deviations (a measure of the day-to-day variability) are shown as error-bars. This figure is taken from the manuscript draft in appendix D.

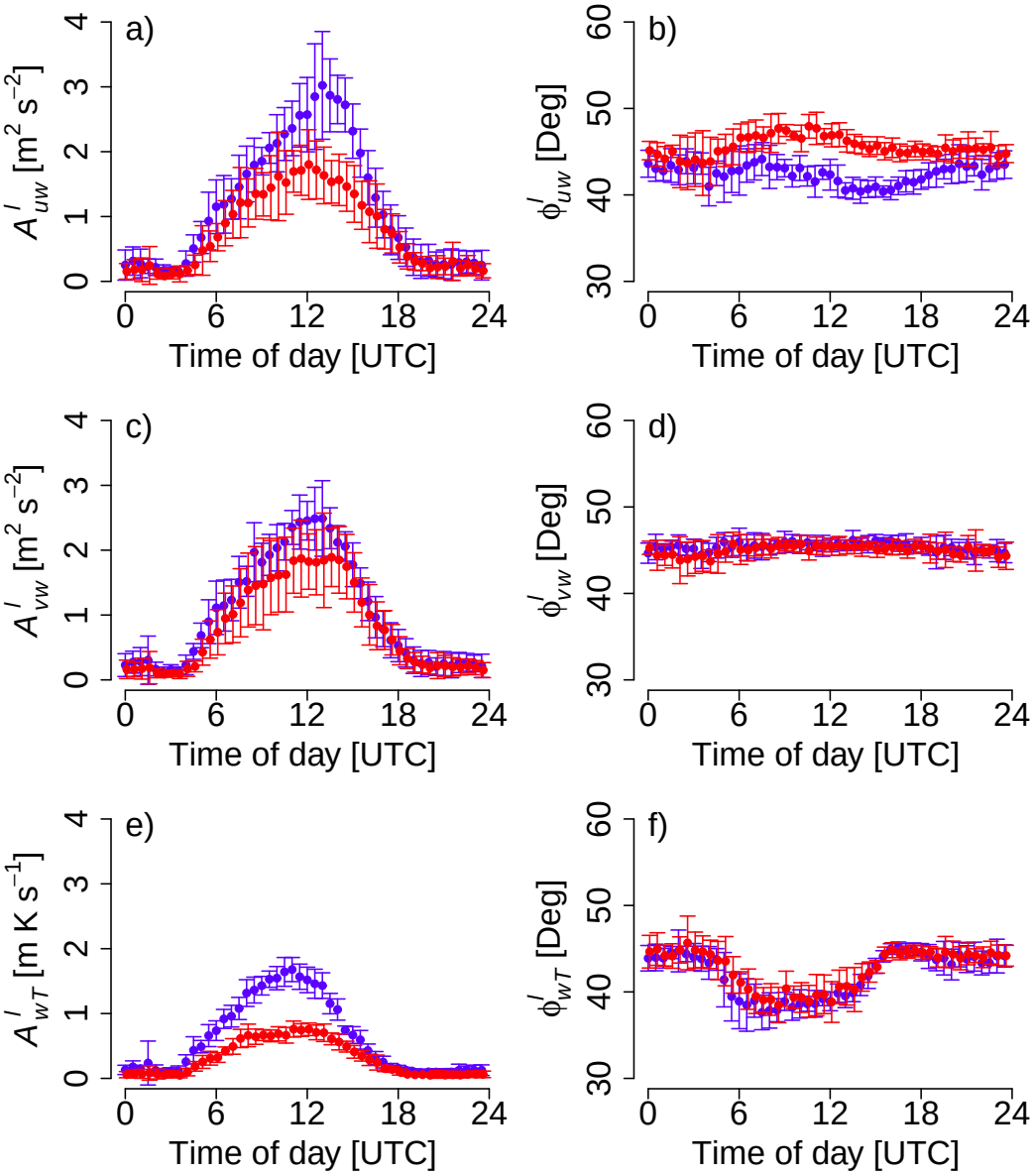

Figure 6: Comparison of the mean diurnal cycle of amplitude (left column) and phase difference (right column) for large eddies between forest (blue) and shrubland (red). In analogy to Fig. 5, the top row shows vertical transport of stream-wise momentum, the middle row the vertical transport of cross-stream momentum, and the bottom row the vertical transport of heat. The mean values are illustrated by points and the standard deviations are shown as an error-bar. This figure is taken from the manuscript draft in appendix D.

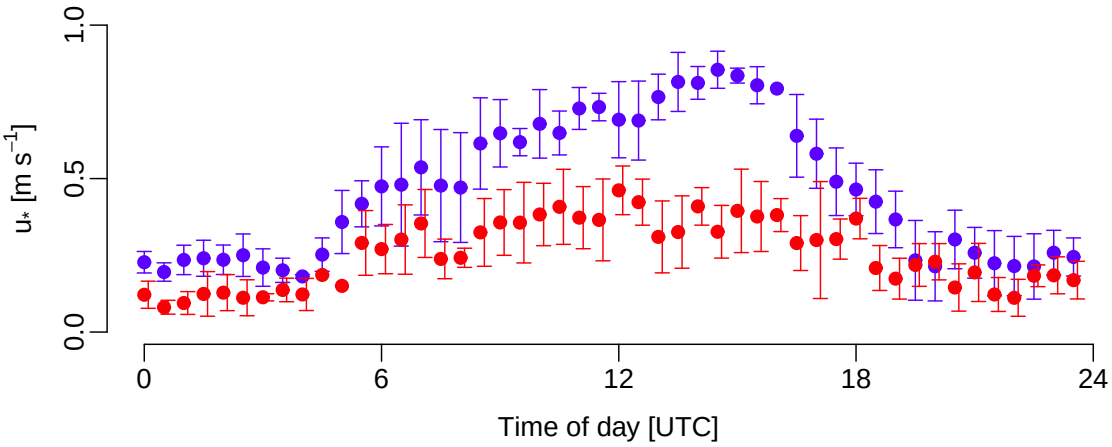

Figure 7: Comparison of the mean diurnal cycle of the friction velocity (u_*) between forest (blue) and shrubland (red). The mean values are illustrated by points and the standard deviation is shown as an error-bar.

3.3 Effect of the Yatir forest on the atmospheric boundary-layer

The effects of the Yatir forest on the ABL height and the diurnal cycle of the ABL is investigated in the following. These results summarize findings presented in Brugger et al. (2018a) and the manuscript draft in appendix D.

3.3.1 Atmospheric boundary-layer height

Brugger et al. (2018a) investigated whether the increased sensible heat and momentum fluxes of the Yatir forest increase the ABL height compared with that over the upwind site. The mean z_i value from 1000–1300 UTC (time of maximum values of z_i) for each day at each site is shown in Fig. 8a. The time series has two features: first, a general increase in the value of z_i from 22–28 August 2015 at all three sites and, second, a period from 22–25 August 2015 when the value of z_i is similar at the three sites, and a period from 26–29 August 2015 with an increase in z_i values from the upwind to downwind of the forest.

The potential temperature gradient of the free atmosphere above the ABL is shown in Fig. 8b. It has larger values corresponding to more stable stratification between 22 August 2015 and 25 August 2015 compared to smaller values from 26 August 2015 until 29 August 2015 corresponding to less stable stratification. The period with more stable stratification coincides with similar z_i values at all three sites, while the period with a less stable stratification coincides with an increase in z_i values over the forest. The change of the potential temperature gradient is presumably caused by the southern outreaches of a Rossby-wave passage in the westerlies (Global Forecast System reanalysis).

The change in stratification may explain the site differences in z_i, because the ABL requires energy to penetrate the free atmosphere against stable stratification, and the required energy increases with stability. The increase in ABL height from the upwind site to the forest or downwind site Δz_i is

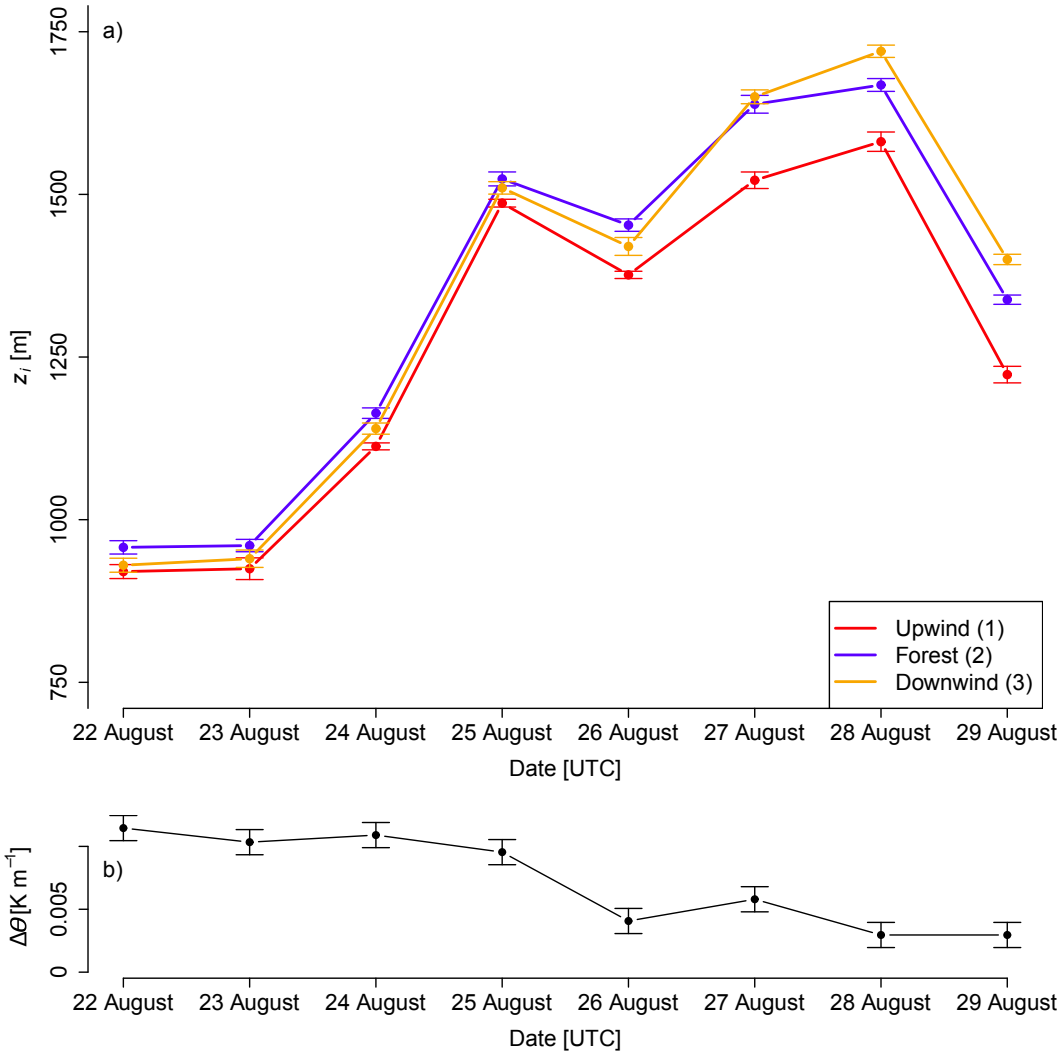

Figure 8: Top (a): the 1000–1300 UTC mean ABL height (z_i) for each day for the upwind (red), forest (blue) and downwind (orange) sites as detected from the backscatter profiles of the lidars (section 2.3.5). The error bars show the standard error of the mean. Bottom (b): time series of the 1200 UTC values of the potential-temperature gradient $\Delta\theta$ of the free atmosphere above the ABL computed from radio soundings at Beit Dagan as described in Sect. 2.2.4. The error bars show the error bounds of $\Delta\theta$ values based on the accuracy of the radiosonde measurements. This figure is taken from Brugger et al. (2018a) in appendix B.

investigated with a model given by

$$\Delta z_i = \frac{u_*}{u_m}\left(\frac{2(\theta_f-\theta_d)(\Delta d - u_m\frac{z_i}{w_*})}{\Delta\theta(\beta^2(2\beta+1))^{-1}}\right)^{1/2}, \tag{12}$$

with $\theta_f - \theta_d$ the difference in potential air temperature between forest and shrubland, Δd the distance to the forest edge in wind direction, u_m the mixed layer wind speed (vertically averaged between 250 and 1000 m), $w_* = (gz_i\overline{w'\theta'}\theta^{-1})^{1/3}$ the convective velocity scale (Deardorff, 1970), and $\beta = 0.2$ the ratio between entrainment flux at the ABL top and sensible heat flux at the surface, which is assumed to be constant (Betts and Ridgway, 1989). The model is conceptually comprised of two parts: first, the forest's effects rise linearly with convective velocity scale to the boundary-layer top and, second, followed by a squared-root growth against the stably stratified free atmosphere adapted from Venkatram (1977) (detailed description in appendix B). Input values of the model were mean values calculated from 1000–1300 UTC from Doppler-Lidar and eddy-covariance measurements (Fig. 7 in appendix B) and the value of $\Delta\theta$ from 1200 UTC shown in Fig. 8b. Figure 9a shows the results for the forest site, which agree within the margin of the standard error of the measurements. For the conditions prevailing during the campaign, the value of Δz_i is mainly controlled by the combination of the stratification of the free atmosphere and the background flow in the mixed layer. In all cases the increase in Δz_i is smaller than what would be expected for an ABL that is fully adapted to the Yatir forest (Brugger et al., 2018a). The results for the downwind site have large deviations from the measurements during the first period with a more stable stratification in the free atmosphere, but show agreement with the measurements for the period with less stable stratification (Fig. 9b). A theory concerning the structure of the convective ABL over complex terrain suggests that a strong capping inversion makes the ABL height less terrain-following (De Wekker and Kossmann, 2015), which may explain the overestimation for the downwind site during the first period, because the site is located on a ridge at a higher elevation than the other two sites, and the heterogeneous model assumes a terrain-following ABL. It is referred to Brugger et al. (2018a) for a further discussion of biases due to the topography and the different instruments used.

3.3.2 Interactions of sea-breeze and diurnal cycle of the ABL

The impact of the sea-breeze on the diurnal cycle of the ABL is investigated with results summarized from the manuscript draft in appendix D. The peak times of the amplitudes (Fig. 5 and Fig. 6) and turbulence statistics (Table 1) are located at different times of the day and allow to identify four groups:

1. $\overline{T}$, σ_T^2, and $\overline{w'T'}$ with an early peak at $1000 - 1200$ UTC.
2. $\overline{u}$, σ_w^2, and $\overline{u'w'}$ with a late peak at $1300 - 1500$ UTC.
3. σ_v^2, $\overline{u'T'}$, and $\overline{v'w'}$ as a group in between.
4. σ_u^2 (Fig. 11a) has an especially interesting behaviour as its peak is in the early group for the shrubland site, but in the late group for the forest site.

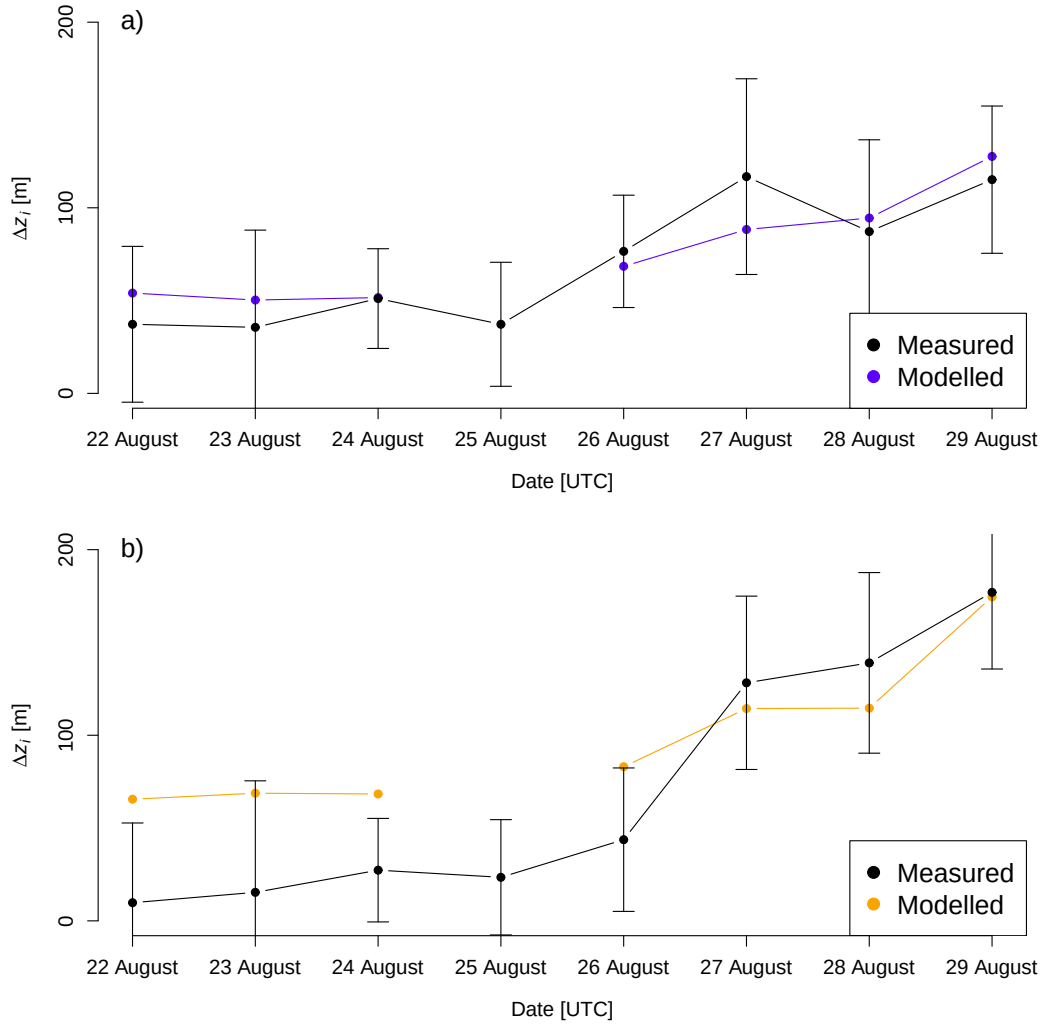

Figure 9: Increase in the ABL height Δz_i from the upwind site to the forest site (a), and from the upwind site to the downwind site (b) according to lidar measurements (black) averaged from 1000–1300 UTC. The error bars show the sum of the standard error of both instruments. The predicted increase by the heterogeneous model given by Eq. 12 is shown for the forest (blue) and the downwind site (orange). This figure is taken from Brugger et al. (2018a) in appendix B.

The differences can be explained with a temporal off-set between buoyant and mechanical turbulence production. The net radiation, which is the driver for surface heating and associated buoyant turbulence production, has its maximum values close to the local noon time at 1000 UTC in accordance with maximum zenith angle of the sun (Fig. 10a). The wind speed measured from the ultrasonic anemometer has an asymmetric diurnal cycle with the maximum in the afternoon (Fig. 10b), which can be explained by a super-position of downward mixing of the north-western geostrophic wind and the delayed arrival of a sea-breeze due to the distance from the Mediterranean sea (Fig. 10c). The contribution from the geostrophic wind is assumed to follow the diurnal cycle of the surface temperature (Zhang and Zheng, 2004) and the sea-breeze as a narrower bell-shaped curve delayed by 4.5 hours due to the Yatir forest's distance from the Mediterranean sea (more detailed description in section 3.3 of appendix D). Those driving mechanisms affect the four groups differently:

1. Quantities closely linked to the surface heating and buoyant production of turbulence have an early peak driven by the net radiation.

2. Quantities connected to the wind speed and resulting mechanical production of turbulence have a late peak due to the delayed arrival of the sea breeze.

3. Quantities which are driven by both (wind speed and surface heating) or the redistribution of turbulent kinetic energy have their peak in the middle group.

4. The special case of σ_u^2 can be explained by the different turbulence production regimes of shrubland and forest. At the shrubland the production is buoyancy driven and redistribution of turbulent kinetic energy from the vertical is larger than the mechanical production and leads to an early peak. At the forest the mechanical production is the main source of turbulent kinetic energy and the peak is therefore in the afternoon with the sea breeze.

Quantity	Forest	Shrubland
u	1330	1400
T	1130	1100
σ_u^2	1300	1100
σ_v^2	1130	1200
σ_w^2	1300	1430
σ_T^2	1030	0900
$\overline{u'v'}^*$	1200	1200
$\overline{v'w'}^*$	1130	1130
$\overline{u'w'}$	1300	1330
$\overline{u'T'}$	1300	1200
$\overline{v'T'}^*$	1000	0800
$\overline{w'T'}$	1100	1200

Table 1: Peak times of the (absolute) mean diurnal cycle of turbulence statistics (left) for forest (middle) and shrubland site (right). The asterisks indicate quantities were day-to-day variations (standard deviation of mean diurnal cycle) were of similar magnitude as the diurnal cycle and, therefore, the maximum could be erroneous. This table is taken from the manuscript draft in appendix D.

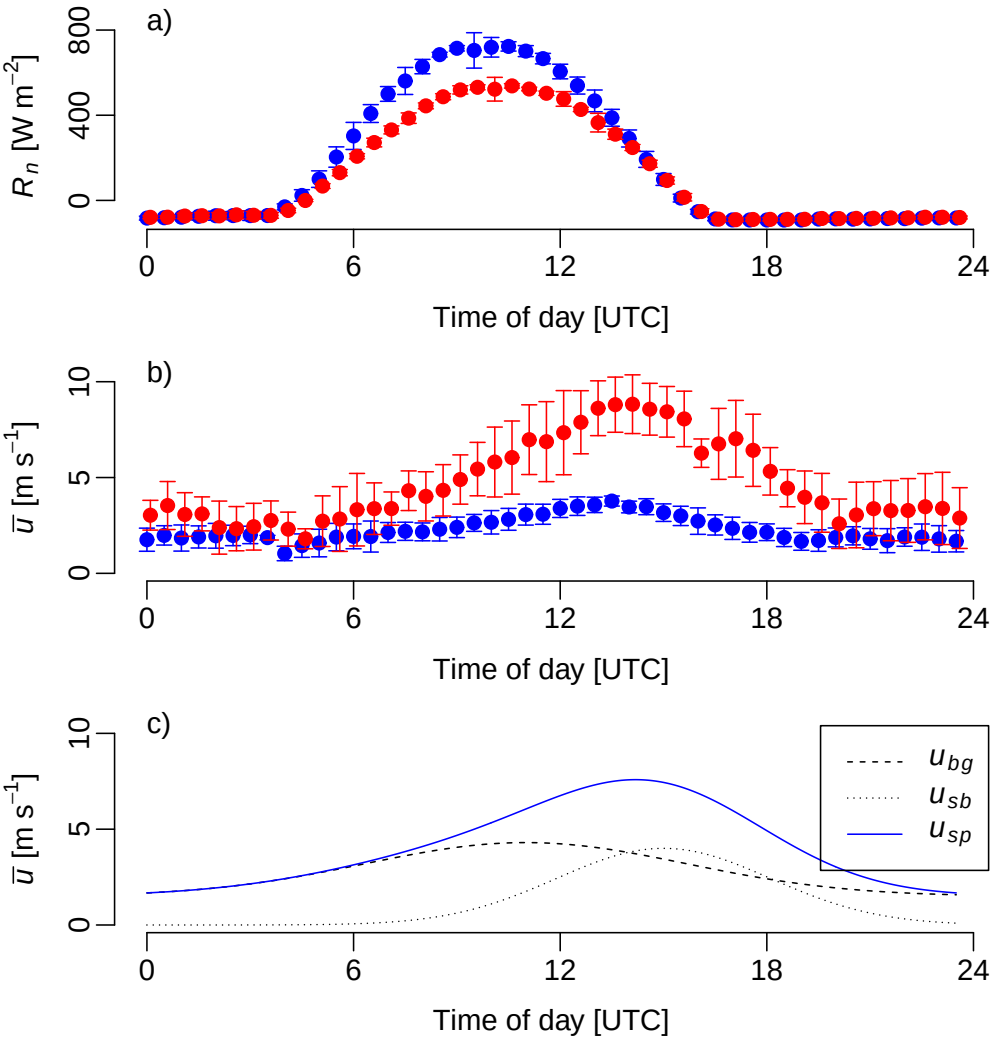

Figure 10: Top (a): Mean diurnal cycle of net radiation with the standard deviation as error-bars. The forest site is shown in blue and the shrubland site in red. Middle (b): Mean diurnal cycle of the wind speed with the standard deviation as error-bars from the eddy-covariance stations of the forest site (blue) and the shrubland site (red). Bottom (c): Simple model to explain the diurnal cycle of the wind speed (solid blue) as superposition of the downward mixing of the synoptic-background wind (black dashed) and the sea-breeze (black dotted). This figure is taken from the manuscript draft in appendix D.

3.3.3 Evening transition at Yatir forest

Indicators for the formation of a residual layer at the Yatir forest have been observed and are summarized from the manuscript draft in appendix D below:

1. In the afternoon (1300 – 1700 UTC) the shrubland has stronger turbulence in the mixed layer (Fig. 11b), while near the surface the ultrasonic anemometers still measure higher velocity variances at the forest (σ_u^2 is shown in Fig. 11a, σ_v^2 is similar throughout the day for forest and shrubland (not shown), and σ_w^2 is always larger at the forest (not shown)).

2. The triple moment $\overline{w'w'T'}$ becomes negative at the forest in the afternoon (Fig. 11c), which can be linked to the vertical gradient of the sensible heat flux, if a gradient diffusion approximation is assumed:

$$\overline{w'w'T'} = -C\tau\sigma_w \frac{\partial \overline{w'T'}}{\partial z}, \tag{13}$$

   where C is a similarity constant and τ is a relaxation time scale defined by the ratio of turbulent kinetic energy and its mean dissipation rate (Katul et al., 2013). Then, a negative $\overline{w'w'T'}$ is connected to a positive $\partial\overline{w'T'}/\partial z$.

This findings are interpreted as a very rapid cooling of the forest in the afternoon due to the late wind speed maximum in combination with the importance of mechanical turbulence production for the sensible heat flux at the Yatir forest. Once the residual heat is removed from the forest and the air is cooling, the advected ABL from the shrubland upwind is warmer and an inversion can form at the interface with the residual layer above. This explanation is also in line with the cooler nighttime temperatures at the forest compared to its surroundings reported by Yosef et al. (2017).

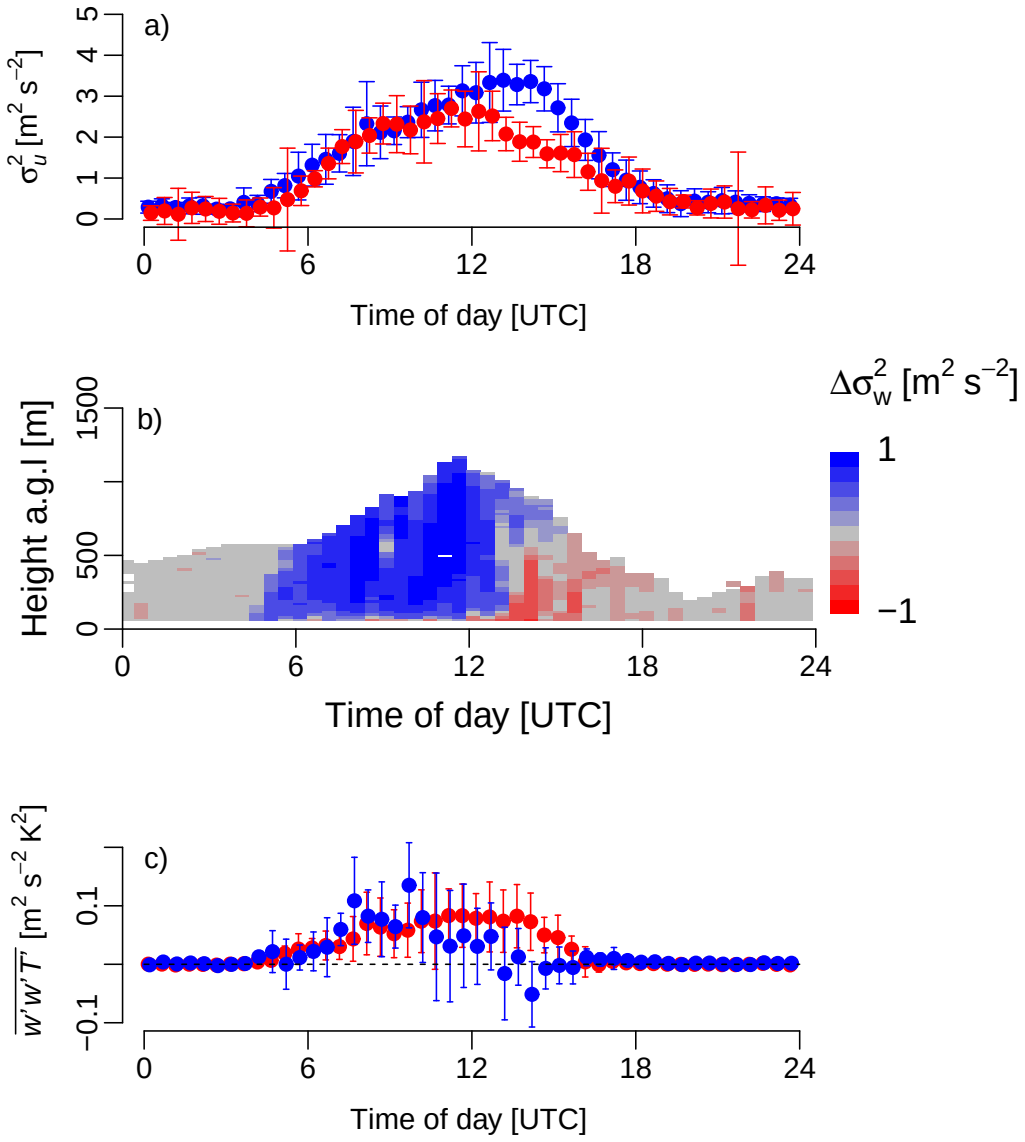

Figure 11: Top (a): Mean diurnal cycle of stream-wise velocity variance (σ_u^2) with the standard deviation as error-bars. The forest site is shown in blue and the shrubland site in red. Middle (b): Time-height plot of the difference in vertical velocity variance between forest and shrubland ($\Delta\sigma_w^2 = \sigma_{w,f}^2 - \sigma_{w,d}^2$) from the Doppler-lidar measurements. Red colors indicate larger σ_w^2 at the shrubland site and blue colors at the forest site (logarithmic spacing of the color bar to emphasis the differences). Bottom (c): Mean diurnal cycle of the triple moment $\overline{w'w'T'}$ with standard deviations as error-bars. The forest site is shown in blue and the shrubland site in red. This figure is taken from the manuscript draft in appendix D.

4 Conclusions

This PhD thesis studied the surface-atmosphere interactions of the solitary, semi-arid Yatir forest surrounded by a sparse shrubland based on measurement data gathered from Doppler-lidar, ceilometer and ultrasonic anemometer measurements.

The properties of the forest canopy lead to a more isotropic turbulence and a higher shear vorticity compared to the shrubland. The reduced momentum transport abilities of more isotropic turbulence are overcompensated by the higher vorticity leading to a more efficient and more energetic momentum transport of the forest canopy compared to the shrubland. Scale wise analysis showed that important processes are located at the large, turbulence-producing scales, while the small scales did not contribute to those differences between the shrubland and the forest. The sensible heat flux had the same efficiency at the forest and the shrubland, but was more energetic at forest site due to the stronger turbulence. Those findings help to understand the reduced aerodynamic resistance to heat transfer of the Yatir forest as a consequence of stronger turbulence, but not a more efficient transport process of heat. This finding should be a general feature of a canopy and apply to other forests as well.

In case of the Yatir forest, the higher momentum and heat fluxes compared to the shrubland affected the whole depth of the ABL and interact with a daily occurring sea-breeze during the summer dry season. It was observed that the Yatir forest increases the vertical velocity variances throughout the ABL during most of the day. An increase of the ABL height compared to upwind site is possible and was observed, but can be suppressed by a strongly stable stratification of the free atmosphere. This finding indicates that the forest size is at the lower limit to have an detectable effect on the ABL height, because the sensible heat fluxes of the forest, which are twice as high as those of the shrubland during the day, could enable a larger increase.

The different turbulence production regimes of the forest and the shrubland in combination with a temporal off-set between surface heating and maximum wind speed due to a delayed arrival of a sea-breeze have an effect on the diurnal cycle. Turbulence statistics closely connected to the buoyant production have their peak values earlier than those connected to mechanical production (in case of the streamwise velocity variance this leads to differences between the sites, because at the forest it was driven by mechanical production, whereas at the shrubland by redistribution from buoyant production).

The importance of the mechanical production for the sensible heat fluxes of the forest in combination with the sea-breeze led to a faster evening transition of the ABL. During the afternoon existed a time window, when the ABL over the shrubland was still well mixed, while at the Yatir forest a decoupled residual layer had already developed.

References

M. Aubinet, T. Vesala, and D. Papale. *Eddy covariance: a practical guide to measurement and data analysis*. Springer Science & Business Media, 2012. 438 pp.

S. Banerjee, R. Krahl, F. Durst, and C. Zenger. Presentation of anisotropy properties of turbulence,

invariants versus eigenvalue approaches. *Journal of Turbulence*, (8):N32, 2007. doi: 10.1080/14685240701506896.

T. Banerjee, P. Brugger, F. De Roo, K. Kröniger, D. Yakir, E. Rotenberg, and M. Mauder. Turbulent transport of energy across a forest and a semi-arid shrubland. *Atmospheric Chemistry and Physics Discussion*, 2017:1–21, 2017. doi: 10.5194/acp-2017-159.

R. G. Barry and R. J. Chorley. *Atmosphere, weather and climate*. Routledge, 29 West 35th Street, New York, NY 10001, 8th edition, 2003. 421 pp.

A. K. Betts and W. Ridgway. Climatic equilibrium of the atmospheric convective boundary layer over a tropical ocean. *Journal of the Atmospheric Sciences*, 46(17):2621–2641, 1989. doi: 10.1175/1520-0469(1989)046⟨2621:CEOTAC⟩2.0.CO;2.

R. A. Betts. Offset of the potential carbon sink from boreal forestation by decreases in surface albedo. *Nature*, 408(6809):187–190, 2000. doi: doi:10.1038/35041545.

K. A. Browning and R. Wexler. The determination of kinematic properties of a wind field using doppler radar. *Journal of Applied Meteorology*, 7(1):105–113, 1968. doi: 10.1175/1520-0450(1968)007⟨0105:TDOKPO⟩2.0.CO;2.

P. Brugger, T. Banerjee, F. De Roo, K. Kröniger, R. Qubaja, S. Rohatyn, E. Rotenberg, F. Tatarinov, D. Yakir, F. Yang, and M. Mauder. Effect of surface heterogeneity on the boundary-layer height: a case study at a semi-arid forest. *Boundary-Layer Meteorology*, ?(?):Accepted, 2018a. doi: 10.1007/s10546-018-0371-5.

P. Brugger, G. G. Katul, F. De Roo, K. Kröniger, E. Rotenberg, S. Rohatyn, and M. Mauder. Scale-wise invariant analysis of the anisotropic reynolds stress tensor for atmospheric surface layer and canopy sublayer turbulent flows. *Physical Review Fluids*, 3:054608, May 2018b. doi: 10.1103/PhysRevFluids.3.054608.

E. J. Burke, S. J. Brown, and N. Christidis. Modeling the recent evolution of global drought and projections for the twenty-first century with the hadley centre climate model. *Journal of Hydrometeorology*, 7(5):1113–1125, 2006. doi: 10.1175/JHM544.1.

U. Dayan and J. Rodnizki. The temporal behavior of the atmospheric boundary layer in israel. *Journal of Applied Meteorology*, 38(6):830–836, 1999. doi: 10.1175/1520-0450(1999)038⟨0830:TTBOTA⟩2.0.CO;2.

S. F. J. De Wekker and M. Kossmann. Convective boundary layer heights over mountainous terrain - a review of concepts. *Frontiers in Earth Science*, 3:77, 2015. doi: 10.3389/feart.2015.00077.

J. W. Deardorff. Preliminary results from numerical integrations of the unstable planetary boundary layer. *Journal of the Atmospheric Sciences*, 27(8):1209–1211, 1970.

F. Eder, F. D. Roo, E. Rotenberg, D. Yakir, H. P. Schmid, and M. Mauder. Secondary circulations at a solitary forest surrounded by semi-arid shrubland and their impact on eddy-covariance

measurements. *Agricultural and Forest Meteorology*, 211-212:115 – 127, 2015. doi: https://doi.org/10.1016/j.agrformet.2015.06.001.

J. J. Finnigan, R. H. Shaw, and E. G. Patton. Turbulence structure above a vegetation canopy. *Journal of Fluid Mechanics*, 637:387–424, 2009. doi: 10.1017/S0022112009990589.

T. Foken and B. Wichura. Tools for quality assessment of surface-based flux measurements. *Agricultural and Forest Meteorology*, 78(1):83 – 105, 1996. ISSN 0168-1923. doi: https://doi.org/10.1016/0168-1923(95)02248-1.

C. Francone, G. G. Katul, C. Cassardo, and R. Richiardone. Turbulent transport efficiency and the ejection-sweep motion for momentum and heat on sloping terrain covered with vineyards. *Agricultural and Forest Meteorology*, 162-163:98 – 107, 2012. doi: 10.1016/j.agrformet.2012.04.012.

Z. Gao, H. Liu, G. G. Katul, and T. Foken. Non-closure of the surface energy balance explained by phase difference between vertical velocity and scalars of large atmospheric eddies. *Environmental Research Letters*, 12(3):034025, 2017.

U. Högström and A.-S. Smedman. Accuracy of sonic anemometers: Laminar wind-tunnel calibrations compared to atmospheric in situ calibrations against a reference instrument. *Boundary-Layer Meteorology*, 111(1):33–54, 2004. doi: 10.1023/B:BOUN.0000011000.05248.47.

J. C. Isaza and L. R. Collins. On the asymptotic behaviour of large-scale turbulence in homogeneous shear flow. *Journal of Fluid Mechanics*, 637:213–239, 2009. doi: 10.1017/S002211200999053X.

J. C. Kaimal and J. J. Finnigan. *Atmospheric boundary layer flows: their structure and measurement*. Oxford university press, 1994.

G. G. Katul, D. Cava, M. Siqueira, and D. Poggi. *Scalar turbulence within the canopy sublayer*, pages 73–95. John Wiley & Sons, Ltd, 2013. ISBN 9781118527191.

A. N. Kolmogorov. The local structure of turbulence in incompressible viscous fluid for very large reynolds numbers. In *Dokl. Akad. Nauk SSSR*, volume 30, pages 299–303, 1941.

S. Liu, L. Lu, D. Mao, and L. Jia. Evaluating parameterizations of aerodynamic resistance to heat transfer using field measurements. *Hydrology and Earth System Sciences*, 11(2):769–783, 2007. doi: 10.5194/hess-11-769-2007.

C. Lotteraner and M. Piringer. Mixing-height time series from operational ceilometer aerosol-layer heights. *Boundary-Layer Meteorology*, 161(2):265–287, 2016. doi: 10.1007/s10546-016-0169-2.

J. L. Lumley and G. R. Newman. The return to isotropy of homogeneous turbulence. *Journal of Fluid Mechanics*, 82(1):161–178, 1977. doi: 10.1017/S0022112077000585.

M. Mauder and T. Foken. *Documentation and Instruction Manual of the Eddy-Covariance Software Package TK3 (update)*. Universität Bayreuth/Abteilung Mikrometeorologie, Bayreuth, 2015.

M. Mauder, M. Cuntz, C. Drüe, A. Graf, C. Rebmann, H. P. Schmid, M. Schmidt, and R. Steinbrecher. A strategy for quality and uncertainty assessment of long-term eddy-covariance measurements. *Agricultural and Forest Meteorology*, 169:122 – 135, 2013. doi: 10.1016/j.agrformet.2012.09.006.

C. Münkel, N. Eresmaa, J. Räsänen, and A. Karppinen. Retrieval of mixing height and dust concentration with lidar ceilometer. *Boundary-Layer Meteorology*, 124(1):117–128, 2007. doi: 10.1007/s10546-006-9103-3.

S. B. Pope. *Turbulent Flows*. Cambridge University Press, 2000. doi: 10.1017/CBO9780511840531.

M. R. Raupach. Anomalies in flux-gradient relationships over forest. *Boundary-Layer Meteorology*, 16(3):467–486, 1979. doi: 10.1007/BF03335385.

M. R. Raupach, J. J. Finnigan, and Y. Brunet. *Coherent Eddies and Turbulence in Vegetation Canopies: The Mixing-Layer Analogy*, pages 351–382. Springer Netherlands, Dordrecht, 1996. doi: 10.1007/978-94-017-0944-6_15.

O. Reynolds. On the dynamical theory of incompressible viscous fluids and the determination of the criterion. *Philosophical Transactions of the Royal Society of London. A*, 186:123–164, 1895. ISSN 02643820.

E. Rotenberg and D. Yakir. Contribution of semi-arid forests to the climate system. *Science*, 327 (5964):451–454, 2010. doi: 10.1126/science.1179998.

E. Rotenberg and D. Yakir. Distinct patterns of changes in surface energy budget associated with forestation in the semiarid region. *Global Change Biology*, 17(4):1536–1548, 2011. doi: 10.1111/j.1365-2486.2010.02320.x.

S. G. Saddoughi. Local isotropy in complex turbulent boundary layers at high reynolds number. *Journal of Fluid Mechanics*, 348:201–245, 1997.

P. Schotanus, F. T. M. Nieuwstadt, and H. A. R. De Bruin. Temperature measurement with a sonic anemometer and its application to heat and moisture fluxes. *Boundary-Layer Meteorology*, 26(1): 81–93, 1983. doi: 10.1007/BF00164332.

P. Seibert, F. Beyrich, S.-E. Gryning, S. Joffre, A. Rasmussen, and P. Tercier. Review and intercomparison of operational methods for the determination of the mixing height. *Atmospheric Environment*, 34(7):1001–1027, 2000. doi: 10.1016/S1352-2310(99)00349-0.

M. Sprintsin, A. Karnieli, P. Berliner, E. Rotenberg, D. Yakir, and S. Cohen. Evaluating the performance of the modis leaf area index (lai) product over a mediterranean dryland planted forest. *International Journal of Remote Sensing*, 30(19):5061–5069, 2009. doi: 10.1080/01431160903032885.

R. B. Stull. *An introduction to boundary layer meteorology*. Kluwer Academic Publishers, Dordrecht, 1988. doi: 10.1007/978-94-009-3027-8. 670 pp.

G. I. Taylor. The spectrum of turbulence. In *Proceedings of the Royal Society of London A: Mathematical, Physical and Engineering Sciences*, volume 164, pages 476–490. The Royal Society, 1938.

I. Van der Hoven. Power spectrum of horizontal wind speed in the frequency range from 0.0007 to 900 cycles per hour. *Journal of Meteorology*, 14(2):160–164, 1957. doi: 10.1175/1520-0469(1957)014⟨0160:PSOHWS⟩2.0.CO;2.

A. Venkatram. A model of internal boundary-layer development. *Boundary-Layer Meteorology*, 11 (4):419–437, 1977. doi: 10.1007/BF02185869.

C. Werner. Dopper Wind Lidar. In C. Weitkamp, editor, *Lidar: Range-Resolved Optical Remote Sensing of the Atmosphere*, pages 325–354. Springer, 2005. ISBN 0-387-40075-3.

J. M. Wilczak, S. P. Oncley, and S. A. Stage. Sonic anemometer tilt correction algorithms. *Boundary-Layer Meteorology*, 99(1):127–150, 2001. doi: 10.1023/A:1018966204465.

G. Yosef, P. Alpert, C. Price, E. Rotenberg, and D. Yakir. Using eof analysis over a large area for assessing the climate impact of small-scale afforestation in a semiarid region. *Journal of Applied Meteorology and Climatology*, 56(9):2545–2559, 2017. doi: 10.1175/JAMC-D-16-0253.1.

D.-L. Zhang and W.-Z. Zheng. Diurnal cycles of surface winds and temperatures as simulated by five boundary layer parameterizations. *Journal of Applied Meteorology*, 43(1):157–169, 2004. doi: 10.1175/1520-0450(2004)043⟨0157:DCOSWA⟩2.0.CO;2.

A Contributions to collaborative publications

The following appendices show the individual publications that contribute to this cumulative dissertation. Here, my contributions to those publication are listed:

Appendix B: Peter Brugger, Tirtha Banerjee, Frederik De Roo, Konstantin Kröniger, Rafat Qubaja, Shani Rohatyn, Eyal Rotenberg, Feodor Tatarinov, Dan Yakir, and Matthias Mauder: Effect of surface heterogeneity on the boundary-layer height: a case study at a semi-arid forest. Boundary-Layer Meteorology (issue not assigned yet), 2018. doi: 10.1007/s10546-018-0371-5
I was responsible for the realisation of the measurements with the Doppler Lidars and Ceilometer at the Yatir forest, data processing (excluding computation of 30-minutes statistics of the eddy-covariance data), data analysis, and writing the manuscript.

Appendix C: Peter Brugger, Gabriel G. Katul, Frederik De Roo, Konstantin Kröniger, Eyal Rotenberg, Shani Rohatyn, and Matthias Mauder: Scalewise invariant analysis of the anisotropic Reynolds stress tensor for atmospheric surface layer and canopy sublayer turbulent flows. Phys. Rev. Fluids, 3(5), 054608, 2018. doi: 10.1103/PhysRevFluids.3.054608
I was responsible for the data processing, data analysis, and writing the following sections of the manuscript: second part of the methods, results and discussion, borader impacts and conclusions.

Appendix D: Peter Brugger, Frederik De Roo, Konstantin Kröniger, Eyal Rotenberg, Feodor Tatarinov, Dan Yakir, Matthias Zeeman and Matthias Mauder: Diurnal variability of the turbulent transport properties above a semi-arid forest canopy in contrast to a nearby shrubland. In preparation for submission to Agricultural and Forest Meteorology

I was responsible for the Doppler lidar measurements, data processing (excluding computation of 30-minutes statistical moments of the ultrasonic anemometer data and surface radiation budget components), data analysis, and writing the manuscript.

Boundary-Layer Meteorology manuscript No.
(will be inserted by the editor)

Effect of surface heterogeneity on the boundary-layer height: a case study at a semi-arid forest

Peter Brugger · Tirtha Banerjee · Frederik De Roo · Konstantin Kröniger · Rafat Qubaja · Shani Rohatyn · Eyal Rotenberg · Feodor Tatarinov · Dan Yakir · Fulin Yang · Matthias Mauder

Received: DD Month YEAR / Accepted: DD Month YEAR

Abstract We investigate the effects of an isolated meso-γ-scale surface heterogeneity for roughness and albedo on the atmospheric boundary-layer (ABL) height, with a case study at a semi-arid forest surrounded by sparse shrubland (forest area: 28 km^2, forest length in the main wind direction: 7 km). Doppler lidar and ceilometer measurements at this semi-arid forest show an increase in the ABL height over the forest compared with the shrubland on four out of eight days. The differences in the ABL height between shrubland and forest are explained for all days with a model that assumes a linear growth of the internal boundary layer of the forest through the convective ABL upwind of the forest followed by a square-root growth into the stable free atmosphere. For the environmental conditions that existed during our measurements, the increase in ABL height due to large sensible heat fluxes from the forest (600 W m^{-2} in

P. Brugger
Karlsruhe Institute of Technology, Institute of Meteorology and Climate Research, Atmospheric Environmental Research, Kreuzeckbahnstraße 19, 82467 Garmisch-Partenkirchen, Germany
Tel.: +49 8821 183 137
Fax: +49 8821 735 73
E-mail: peter.brugger@kit.edu

T. Banerjee
Karlsruhe Institute of Technology, Institute of Meteorology and Climate Research, Atmospheric Environmental Research, Kreuzeckbahnstraße 19, 82467 Garmisch-Partenkirchen, Germany
Present address: Earth and Environmental Sciences Division, Los Alamos National Laboratory, Los Alamos, New Mexico 87545, USA.

F. De Roo · K. Kröniger · M. Mauder
Karlsruhe Institute of Technology, Institute of Meteorology and Climate Research, Atmospheric Environmental Research, Kreuzeckbahnstraße 19, 82467 Garmisch-Partenkirchen, Germany

E. Rotenberg · F. Tatarinov · S. Rohatyn · F. Yang · R. Qubaja · D. Yakir
Weizmann Institute of Science, Faculty of Chemistry, Department of Earth and Planetary Sciences, 234 Herzl Street, Rehovot 7610001, Israel

summer) is subdued by stable stratification in the free atmosphere above the ABL, or reduced by high wind speeds in the mixed layer.

Keywords Boundary-layer height · Forests · Surface heterogeneity · Internal boundary layer · Lidar

1 Introduction

As the lowest part of the atmosphere, the atmospheric boundary layer (ABL) is directly influenced by the underlying surface (Stull 1988), and controls the exchanges of heat, momentum and pollutants between the free atmosphere and Earth's surface. Concepts relating to the ABL, such as scaling laws, usually assume a horizontally homogeneous surface (Lenschow et al. 1980; Sun et al. 2013). However, the Earth's surface is mostly inhomogeneous due to variations in topography and land cover, which has implications for a range of atmospheric transport processes (Rotach et al. 2014). The effects of heterogeneity on the ABL depend on the horizontal scale and amplitude of the surface heterogeneities (Mahrt 2000). The horizontal scales of atmospheric processes are often grouped by their size into three classes: macroscale, mesoscale and microscale, with further subdivision of each class into α, β and γ scales (Orlanski 1975). The importance of macroscale surface heterogeneity (e.g. the land–sea distribution and mountain ranges) in numerical weather prediction is known and recognized, but the importance of the smaller mesoscale (e.g. forests, lakes and cities) and microscale (e.g. forest edges, buildings) surface heterogeneities for the ABL is still uncertain (Maronga and Raasch 2013).

Mesoscale surface heterogeneity studies have shown a range of effects. For example, analytical investigations of thermal heterogeneities by Dalu et al. (1996) showed that these can enhance vertical heat fluxes and that the synoptic background flow weakens the effects. Mauder et al. (2007) found from airborne flux measurements over lakes that the meso-γ-scale contributions to turbulent fluxes may be related to the energy-balance residual, which is a systematic difference between the available energy and turbulent energy observed at micrometeorological sites. Studies of flows over forest edges and clearings show enhanced turbulence levels, modified integral length scales and increased spectral slopes for the velocity fluctuations (Träumner et al. 2012; Eder et al. 2013; Kanani et al. 2014). Studies using large-eddy simulations have investigated the effect of surface heterogeneity on the entrainment flux (Sühring et al. 2014), dispersion (Gopalakrishnan and Avissar 2000; Wu et al. 2009), horizontal wind speed (Kang et al. 2012) and the development of secondary circulations (Maronga and Raasch 2013) and coherent structures (Baidya Roy and Avissar 2000).

The ABL height describes the vertical extent of the region in which the atmosphere is directly influenced by the Earth's surface, and is used in surface-layer parametrizations as an outer-layer scaling parameter (Banerjee and Katul 2013) for the influence of the exchange between the land surface and the atmosphere (Zilitinkevich et al. 2012). The ABL height is highly variable in time

and space depending on topography, the underlying surface, synoptic conditions, and the time of day. Encroachment models neglecting dynamic effects and only accounting for thermodynamical influences predict a deeper ABL for stronger surface heating and for a given mixed-layer temperature (Batchvarova and Gryning 1991). Surface roughness in the presence of a background flow increases the turbulence levels and deepens the ABL as well, but heating and cooling effects are more important for convective conditions (Stull 1988). While studies on the influence of surface heterogeneity on the ABL height are scarce, Zhong and Doran (1995) found from numerical simulations of farm and steppe surfaces that the height of the convective ABL is controlled by the local surface heat flux and roughness, together with horizontal advection and vertical motions arising from convergence or divergence. Using ground-based remote-sensing instruments, De Tomasi et al. (2011) observed a decrease in the ABL height due to a replacement of continental air with maritime air related to the onset of a sea breeze at a coastal site. Huang et al. (2017) investigated the diurnal cycle of the ABL height over a city, and reported a deeper nocturnal boundary layer, which they explained as being due to heat absorbed during the day by man-made structures followed by the night-time release in the form of thermal updrafts.

We investigate the effect of meso-γ-scale surface heterogeneities on the ABL height by focusing on the Yatir forest in Israel, which is an isolated, semi-arid forest surrounded by shrubland (Fig. 1), with pronounced differences in albedo and roughness compared with the surrounding shrubland, making it useful for the study of the effects of surface heterogeneity. Rotenberg and Yakir (2011) analyzed the impact of the Yatir forest on the surface-energy budget, showing an increased surface radiation budget and higher sensible heat fluxes compared with the shrubland. Using the blending-height concept, Eder et al. (2015) estimated that the areal extent of the Yatir forest is of a sufficient magnitude to be able to influence the whole depth of the ABL, and found evidence for the existence of a secondary circulation between the forest and surrounding shrubland.

Our aim here is to investigate whether albedo and roughness heterogeneities with horizontal extent within the meso-γ-scale can modify the whole depth of the ABL. To achieve this aim, we use a case study at the Yatir forest, and (i) investigate the forest's effect on the ABL height, and (ii) develop a model describing the effects.

2 Measurements

We describe our study site at the Yatir forest and the measurement set-up here, followed by the instruments used and the data-processing procedures followed for eddy-covariance stations, Doppler lidars, as well as for the ceilometer and radiosondes.

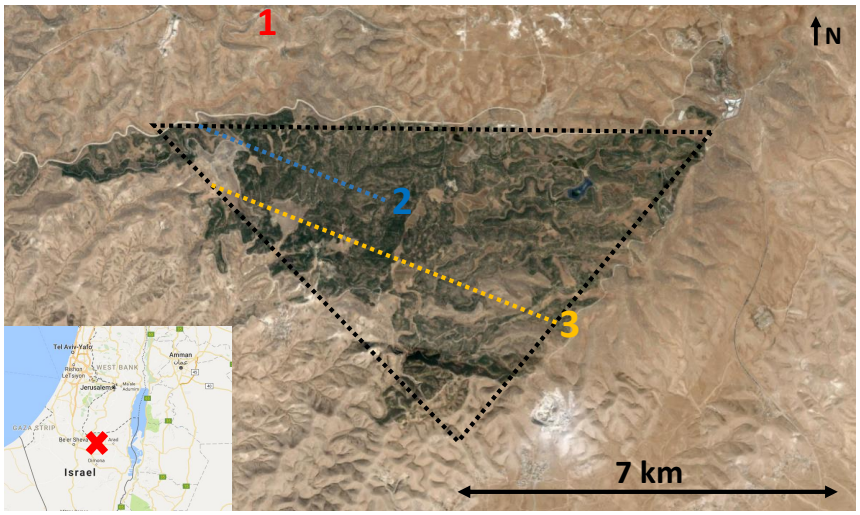

Fig. 1 Satellite image of the Yatir forest with the three measurement sites shown as coloured numbers (see Sect. 2.2). Map of Israel with the location of forest (bottom left, location marked with red cross; the distance from the Mediterranean Sea is approximately 60 km). The dashed lines show the geometry of the heterogeneous model introduced in Sect. 3.2 with the black line showing the approximated shape of the forest and the blue (orange) line showing the distance Δd to the forest edge in the main wind direction for the forest site (downwind site) for 29 August 2015 with a wind direction of 292° as an example. Source of map and satellite image: Google Maps.

2.1 Research site

The evergreen Yatir pine forest, which is located in southern Israel to the west of the Dead Sea and north of the Negev desert (Fig. 1), is a planted forest covering an area of approximately 28 km^2, with a length of 7 km in the main wind direction, and *Pinus halepensis* as the predominant tree species (Rotenberg and Yakir 2011). The climate is semi-arid with an annual mean precipitation of 285 mm and an annual positive surface radiation budget of 238 W m^{-2} (Rotenberg and Yakir 2011). The Yatir forest has a mean height of 662 m above sea level, with its lowest areas at 500 m and highest at 850 m. The older north-western parts of the forest with tree heights of around 11 m were planted from 1964–1969, and planting has continued since. The forest represents isolated heterogeneity for albedo, roughness and surface (skin) temperature compared with the surrounding shrubland. The albedo of the forest is 0.13 compared with 0.34 for the shrubland, and the skin temperature of the forest is 5°C lower on average (Rotenberg and Yakir 2011). The shrubland consists of scattered herbaceous annuals and perennials (mainly *Sarcopoterium spinosum*) with heights ranging from 0.3–0.5 m. During the summer dry season, this leads to sensible heat fluxes of up to 600 W m^{-2} during midday, and friction velocities of 0.8 m s^{-1} over the forest canopy, which are twice as high as those of the surrounding shrubland (Eder et al. 2015).

2.2 Measurement set-up and synoptic conditions

To observe the effects of the forest on the ABL, three measurement sites were established along the main wind direction (Fig. 1):

1. Upwind of the forest (latitude 31.3757°, longitude 35.0242°, 620 m above sea level) to probe the ABL with a Doppler lidar and eddy-covariance station without disturbance from the forest.
2. In the forest (latitude 31.3453°, longitude 35.0522°, 660 m above sea level) to investigate the effect of the forest on the ABL with a Doppler lidar and eddy-covariance station.
3. Downwind of the forest (latitude 31.3258°, longitude 35.0838°, 780 m above sea level) to capture the advection of these effects with a ceilometer.

The measurements were conducted from 16–29 August 2015 during the dry season when the albedo difference between the desert and forest is more pronounced compared with the wet season. During the time of the measurements, the area was located within the subtropical ridge, which is an area of general subsidence in the troposphere connected to the sinking branch of the Hadley cell (Barry and Chorley 2003). The synoptic horizontal pressure gradients are controlled by a heat-induced surface low to the east, the Persian trough (Dayan and Rodnizki 1999), giving a main wind direction from the north-west and cloud free conditions, with a radiation-driven diurnal cycle of the ABL during the campaign.

2.3 Eddy-Covariance Method

We measured the turbulent fluxes at the upwind and forest sites with two eddy-covariance stations. Measurements at the upwind site consisted of a mobile eddy-covariance station from the Weizmann Institute of Science, with an expandable mast equipped with an R3-100 ultrasonic anemometer (Gill Instruments, Lymington, Hampshire, UK) and a LI-7200 gas analyzer (LI-COR Biosciences, Lincoln, Nebraska, USA). The sampling frequency was 20 Hz, and the measurement height was 9 m above the ground until 23 August 2015, before being raised to 15 m to blend local terrain irregularities because of problems with the stationarity assumption due to a small footprint. Both measurement heights are within the surface layer, where fluxes are assumed in theory to be constant with height, which is also approximately the case in these measurements (Aubinet et al. 2012).

The eddy-covariance station at the forest site is the permanent FLUXNET Yatir forest station (Baldocchi et al. 2001), which is equipped with an R3-50 ultrasonic anemometer from Gill Instruments and a LI-7000 gas analyzer from LI-COR Biosciences, with both instruments sampling at a frequency of 20 Hz. The ultrasonic anemometer is mounted 19 m above the ground on a tower surround by trees of an average height of 10 m, placing the ultrasonic anemometer 9 m above the roughness elements. The eddy-covariance data at

the forest is missing on 20 August 2015 from 0308–1750 UTC and on 25 August 2015 from 0910–1500 UTC due to data-acquisition problems.

Computation of the turbulence statistics at 30-min intervals, and the quality control of the eddy-covariance data from both stations was performed with the TK3 software (Mauder and Foken 2015), which includes despiking (Mauder et al. 2013), unit conversions (Schotanus et al. 1983), a transformation of the coordinate system according to the planar-fit method (Wilczak et al. 2001), block averaging, and the determination of time lags by cross-correlation and frequency-response corrections (Moore 1986). The quality control includes steady-state and integral-turbulence tests (Foken and Wichura 1996), with low-quality data discarded based on the flagging system of Mauder et al. (2013).

2.4 Doppler Lidar

Together with the eddy-covariance stations, two Doppler lidars (the Stream Line model, Halo Photonics Ltd., Worcester, UK) were deployed at the upwind and forest sites, and levelled using the internal pitch and roll sensors (instrument specifications in Table 1). Both systems were operated in vertical stare mode with an 18-point velocity-azimuth-display scan at an elevation angle of 70° every 30 min, and every full hour the instrument performed some housekeeping for 30 sec. Wind-speed and direction profiles were computed from the velocity-azimuth-display scans with the method described in Browning and Wexler (1968). Data quality was ensured by averaging 15,000 pulses per estimate for an effective measurement frequency of 1 Hz, while discarding range gates from the lowest 60 m or with a signal-to-noise ratio < -17 dB (Päschke et al. 2015). The Doppler lidar at the upwind site was inoperable due to power cuts from 1500 UTC on 19 August 2015 until 1030 UTC on 21 August 2015, and for a short time on 23 August 2015 around 1000 UTC.

Several methods exist for the determination of the ABL height from ground-based lidars (Lammert and Bösenberg 2006; Hennemuth and Lammert 2006; Träumner et al. 2011), for which we used the gradient method outlined in Münkel et al. (2007), which detects the ABL height by a decrease in the backscatter coefficient between the aerosol-laden ABL and the clean, free atmosphere. The backscatter coefficient profiles were first range corrected, vertically smoothed, while removing noise at large distances. The heights of the largest of three negative gradients above a threshold were then computed for each backscatter profile, and the most frequent heights within each 10-min interval were detected as aerosol-layer heights. To compute the time series of the ABL height from the aerosol layers, and to remove outliers, we followed the algorithm of Lotteraner and Piringer (2016), but without their wind-speed threshold. First, we selected the lowest detected aerosol layer for each timestep, and then outliers were filtered by removing values lower than 100 m, higher than 2500 m, or differing by more than 200 m from the moving average of 1 h.

Table 1 Technical specification of the two Halo-Photonics Stream Line Doppler lidars used at the upwind site and the forest site (left column) and the Vaisala C51 ceilometer (right column) at the downwind site.

serial number (upwind/forest)	0114-75/0114-74	F4460004
range gate length [m]	18	10
pulse length [m]	60	33
pulse repetition frequency [Hz]	15000	6500
laser wavelength [μm]	1.5	0.91

2.5 Ceilometer

A ceilometer model CL51 from Vaisala (Vantaa, Finnland) was deployed at the downwind edge of the forest pointing vertically upwards to measure profiles of the backscatter coefficient. The ceilometer was levelled with a spirit level, and sampled at a temporal resolution of 16 s; the technical specifications are given in Table 1.

Data processing and detection of the largest negative gradients in the backscatter coefficient profiles were performed with the BLMatlab software version 1.9 (Münkel et al. 2007). The algorithm of Lotteraner and Piringer (2016) was also used to compute the time series of the ABL height from Doppler lidar data. Estimates of the ABL height can differ depending on the definition, instrument or algorithm used (Seibert et al. 2000). Side-by-side measurements of the ABL height showed good agreement for convective, cloud-free conditions between the Doppler lidar and ceilometer (see Appendix 1).

2.6 Radiosonde

Information about the stratification of the free atmosphere was obtained from temperature profiles derived from radiosondes launched at Beit Dagan (station number 40179, which is located approximately 75 km from the Yatir forest), which uses RS92/DigiCORA II radiosondes from Vaisala (Vantaa, Finnland). Based on the results of a World Meteorological Organization inter-comparison of radiosondes in Yangjiang, China, the radiosonde has an accuracy of 0.5 K for the temperature, 1 hPa for the pressure, and 20 m for the height in the lower atmosphere. A radiosonde ascending at 5 m s^{-1} corresponds to a 50-m layer averaged over 10 s (Dayan et al. 2002). The Israel Meteorological Service conducted the launches, whose resulting data were distributed via the World Meteorological Organization network, which we accessed at a web portal provided by the University of Wyoming (www.weather.uwyo.edu).

To determine the stratification of the free atmosphere, we first determined the ABL height from the radiosonde profiles using the parcel method as reviewed by Seibert et al. (2000), but without adding an excess temperature. With this method, the ABL height is determined from a temperature inversion at the top of the mixed layer by following the dry adiabat from the lowest

sounding level until it intersects with the temperature profile. The results were found to be in agreement with a subjective method by visually locating an inversion base with a simultaneous dew-point decrease. The 1200 UTC soundings coincide with the local temperature maximum when the ABL has already incorporated the residual layer. The stratification of the free atmosphere was then computed from the potential-temperature gradient $\Delta\theta$ of a 500-m layer starting at the detected ABL height. An alternative approach of computing $\Delta\theta$ from a fixed height interval above the ABL (1500–2000 m) leads to similar results, with the exception on 29 August 2015 when a second elevated inversion was present, so that the parcel method is preferable (not shown). The measurement accuracy leads to an upper error bound of 0.002 K m^{-1} for the potential-temperature gradient. We can assume that the temperature gradient at Beit Dagan is representative for the Yatir forest, because the horizontal variation of the free atmosphere in the subtropical ridge is small (Barry and Chorley 2003).

3 Models of the Boundary-Layer Height

To identify mechanisms affecting the ABL height, we considered two models that take into account the stress at the surface and the stratification of the free atmosphere, with the first assuming horizontal homogeneity, and the second accounting for a change in surface properties.

3.1 Homogeneous Model

The ABL height z_i was computed with a thermodynamic encroachment model, with entrainment at the boundary-layer top given by

$$\frac{dz_i}{dt} = \frac{\overline{w'\theta'} - \overline{w'\theta'}_{z_i}}{\Delta\theta z_i}, \tag{1}$$

where $\overline{w'\theta'}$ is the kinematic heat flux at the surface, $\overline{w'\theta'}_{z_i}$ is the entrainment flux at the boundary-layer top, and $\Delta\theta$ is the potential-temperature gradient of the free atmosphere above the ABL (Carson 1973; Zilitinkevich et al. 2012). For encroachment models, the entrainment flux is usually assumed to be proportional to the sensible heat flux at the surface by $\overline{w'\theta'}_{z_i} = -\beta\overline{w'\theta'}$ (Tennekes 1973), where the value of β (= 0.2) is frequently assumed constant (Betts and Ridgway 1989; Juang et al. 2007). The model assumes both horizontal homogeneity and the boundary layer as a single slab without any internal source or sink terms (Juang et al. 2007). The ABL height was computed by integrating Eq. 1 from 0600–1300 UTC. As an initial condition, the ABL height measured by the Doppler lidars at 0600 UTC is used, which is the earliest time when reliable measurements of the ABL height are available at all sites and for all days. We used $\overline{w'\theta'}$ derived from the eddy-covariance measurements at the respective sites for each timestep, and set the value of $\Delta\theta$ as constant for the

whole day based on the 1200 UTC radiosonde profile at Beit Dagan. For comparison with measurements, the computed ABL heights were averaged from 1000–1300 UTC.

3.2 Heterogeneous Model

The heterogeneous model for describing the ABL height over the forest accounts for the both heterogeneity and the presence of a convective boundary layer upwind of the forest, where a schematic overview of the growth process is shown in Fig. 2. We assume an air parcel travels close to the surface from the shrubland to the forest at a mean horizontal wind speed u_m, and rises convectively at the convective velocity scale $w_* = (g z_i \overline{w'\theta'} \theta^{-1})^{1/3}$ (Deardorff 1970), continuing to rise until reaching the top of the ABL, whose height is not yet influenced by the forest. The distance the air parcel travels horizontally until it reaches the ABL height is given by

$$\Delta x_1 = u_m \frac{z_i}{w_*}, \tag{2}$$

where u_m is the mixed-layer wind speed computed from the Doppler-lidar measurements and averaged between 250 m and 1000 m above ground, z_i is the ABL height from the upwind site measured by the Doppler lidar, and w_* is computed with values from the eddy-covariance station at the forest site. Once at the top of the ABL, an air parcel penetrates the free atmosphere, which deepens the ABL over the forest, similar to the offshore growth of a convective internal boundary layer encountering a stably-stratified atmosphere, assuming air parcels travel along straight trajectories. To compute the increase in the ABL height, we adapted the model of Venkatram (1977) given by

$$\Delta z_i = \frac{u_*}{u_m} \left(\frac{2(\theta_f - \theta_d)\Delta x_2}{\Delta\theta(\beta^2(2\beta+1))^{-1}} \right)^{1/2}, \tag{3}$$

where u_* is the friction velocity of the forest, $\Delta x_2 = \Delta d - \Delta x_1$ is the distance the air parcel travels while working against the free atmosphere after reaching the top of the upwind ABL, Δd is the distance to the forest edge in the wind direction (Fig. 1), and θ_f and θ_d are the potential air temperatures over the forest canopy and at the desert, which are assumed to be constant for both surface types. This assumption can be made because both the shrubland and the forest are horizontally homogeneous within their domain, and, close to the surface, the effects of advection should only matter close to the forest edge (Dupont and Brunet 2008; Kröniger et al. 2017). Furthermore, the model also assumes steady-state conditions for the time scale of the model (≈ 3 h), which may be unsatisfactory during the hours around sunset and sunrise (Venkatram 1977). The distance Δd was computed by approximating the forest shape with a triangle as shown in Fig. 1. The increase in the ABL height was computed for each day based on mean values from 1000–1300 UTC around the time of maximum ABL height, which implicitly assumes that these conditions are

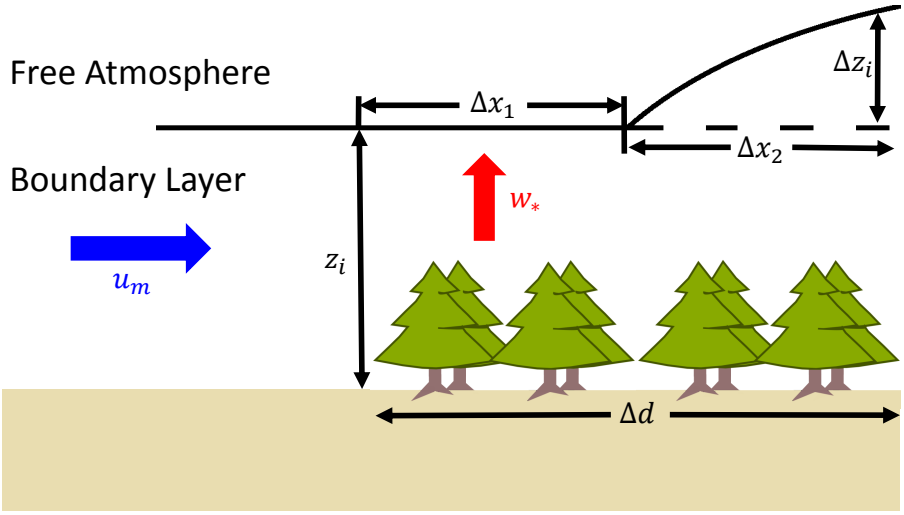

Fig. 2 Schematic image of the increase in the ABL height over the forest as explained in Sect. 3.2.

stationary for a sufficient time such that the effects are transported to the top of the ABL.

4 Results

We first investigate whether the Yatir forest acts to increase the ABL height z_i compared with that over the upwind site. If the forest has an effect on the magnitude of z_i, it is expected that the largest differences between sites occur at the time of the maximum value of z_i, corresponding to between 1000 UTC and 1250 UTC at each site (Table 2). The mean z_i value from 1000–1300 UTC for each day at each site is shown in Fig. 3a (the period is extended to 1300 UTC for consistency with the 30-min eddy-covariance data presented below). Features of note are a general increase in the value of z_i from 22–28 August 2015 at all three sites, a period from 22–25 August 2015 when the value of z_i is similar at the three sites, and a period from 26–29 August 2015 with an increase in z_i values from the upwind to downwind of the forest. The mean difference between the upwind and downwind sites during the period with similar z_i values at all sites is 19 m, but 122 m during the period with an increase in z_i values over the forest. The root-mean-square error between the instruments is 48 m (see Appendix 1 for side-by-side comparisons of the Doppler lidar and ceilometer measurements). By investigating the periods around the time of maximum ABL height, we also avoid detection problems associated with multiple layers of weak aerosol-density changes during the night, and periods without a fully convective boundary layer.

The potential-temperature gradient of the free atmosphere above the ABL is shown in Fig. 3b, illustrating larger values during more stable stratification

Table 2 Time of maximum ABL height according to Doppler lidar and Ceilometer data for each site and day.

Date	Upwind	Forest	Downwind
22 August 2015	1200	1140	1200
23 August 2015	1210	1140	1200
24 August 2015	1120	1140	1200
25 August 2015	1050	1250	1140
26 August 2015	1150	1150	1240
27 August 2015	1100	1100	1110
28 August 2015	1040	1030	1200
29 August 2015	1000	1020	1040

from 22–25 August 2015 compared with smaller values from 26–29 August 2015 corresponding to less stable stratification. The accuracy of the potential-temperature gradient is 0.002 K m^{-1}, which is sufficient to separate the two periods. The period with more stable stratification coincides with similar z_i values at all three sites, while the period with a less stable stratification coincides with an increase in z_i values over the forest. The change in stratification may explain the site differences, because the ABL requires energy to penetrate the free atmosphere against stable stratification, and the required energy increases with stability. Moreover, the energy input for the ABL growth from the sensible heat fluxes did not vary much from day to day during the campaign (the mean values from 1000–1300 UTC varied to within 16% of the campaign mean as shown in Fig. 6b). The change in the potential-temperature gradient is presumably caused by the southern extension of a Rossby-wave passage in the westerlies, which changed the curvature of the isohypses from anticyclonic to cyclonic, and cooled the free atmosphere (Global Forecast System reanalysis). Both indicate that the large-scale subsidence was reduced in the eastern Mediterranean, which weakened the stable stratification in the lower free atmosphere.

The effect of stratification on the general increase in z_i values at all three sites from 22–28 August 2015 are investigated using the homogeneous-slab model (Eq. 1) without consideration of the free-atmosphere stratification, which predicts constant z_i values throughout the campaign, and overestimates z_i over the forest on all days compared with the measurements (Fig. 4a). The model including the stratification from the radiosonde data predicts a value of z_i roughly similar to the measurements for the upwind site with the exception of measurements on 25 August 2015 (the absolute mean difference excluding 25 August 2015 is 109 m), but always shows an overestimated value of z_i at the forest (Fig. 4b). Since the background flow speed was higher on 25 August 2015 than on any other day during the campaign (see Fig. 6a), the failure of the model on this day may be explained by the model only accounting for buoyancy-driven growth of the boundary layer. A second exception is 29 August 2015, which has lower z_i values despite a low potential-temperature gradient (Fig. 3b), but this decline is reproduced by the model for the upwind site. This result suggests that the general increase in z_i values at all three sites is connected to a decrease of the stable stratification of the free atmosphere

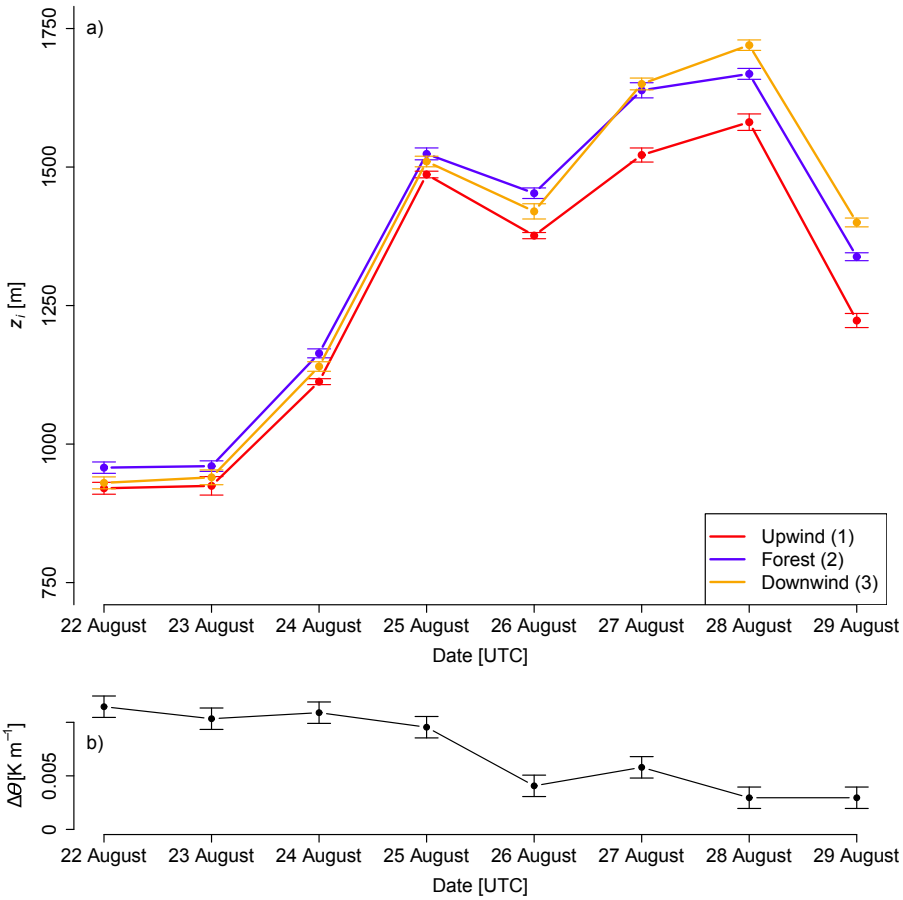

Fig. 3 Top (a): the 1000–1300 UTC mean ABL height z_i for each day for the upwind (red), forest (blue) and downwind (orange) sites as detected by a drop in the aerosol density from the backscatter profiles of the lidars using the methods described in Sects. 2.4 and 2.5. The error bars show the standard error of the mean. Bottom (b): time series of the 1200 UTC values of the potential-temperature gradient $\Delta\theta$ of the free atmosphere above the ABL computed from radio soundings at Beit Dagan as described in Sect. 2.6. The error bars show the error bounds of $\Delta\theta$ values based on the accuracy of the radiosonde measurements.

above the ABL from 0.010 K m^{-1} to 0.004 K m^{-1}, but cannot explain all the variation of z_i alone. However, these results show that the boundary layer over the forest site is not yet fully adapted to the new surface.

The increase in ABL height from the upwind site to the forest or downwind site Δz_i is investigated with the heterogeneous model (Eq. 3). Figure 5a shows a comparison of the predicted and measured Δz_i values by the model and Doppler lidars, respectively, for the forest site, which agree within the margin of the standard error of the measurements. For the conditions prevailing during the campaign, the value of Δz_i is mainly controlled by the combination of the stratification of the free atmosphere (see Fig. 3b) and the background flow

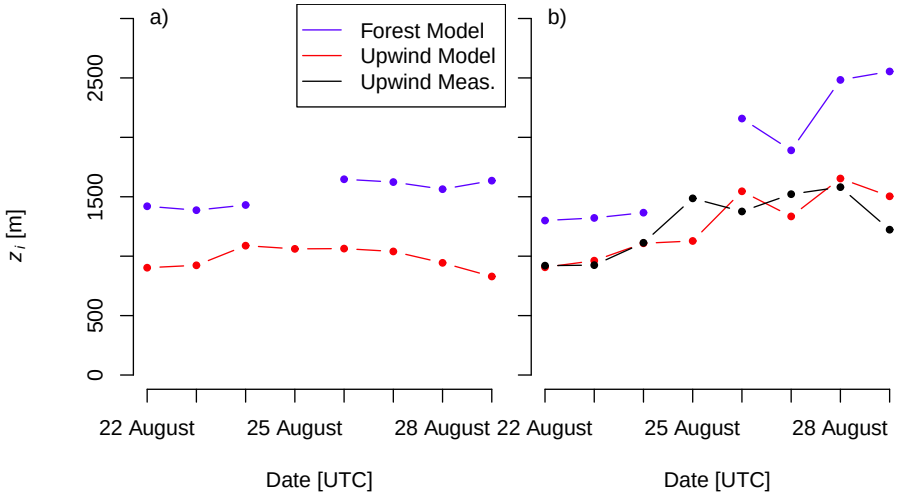

Fig. 4 Mean values of z_i from 1000–1300 UTC for each day for the upwind (red) and forest (blue) sites computed with the homogeneous model (Eq. 1). The left panel (a) shows the predicted z_i values based on the measured sensible heat flux at the eddy-covariance stations and a constant potential-temperature gradient of $\Delta\theta = 0.01$ K m^{-1}. The right panel (b) shows the results usingthe value of $\Delta\theta$ obtained from the radiosonde launches at Beit Dagan shown in Fig. 3b. For comparison, the measured z_i values for the upwind site as shown in Fig. 3a are plotted in the right panel (black).

in the mixed layer (see Fig. 6a), which enters Eq. 3 twice by also influencing the magnitude of Δx_2. The variations of the sensible heat flux, the friction velocity, and temperature differences (see Fig. 6b–d) do not have a strong impact on the results, either because their variations during the campaign were too small, or because the magnitude of Δz_i is not sensitive to any variations. The results for the downwind site have large deviations from the measurements during the first period with a more stable stratification in the free atmosphere, but show agreement with the measurements for the period with less stable stratification (Fig. 5b). Theories concerning the structure of the convective ABL over complex terrain suggests that a strong capping inversion makes the ABL height less terrain-following (De Wekker and Kossmann 2015; Stull 1992), which may explain the overestimation for the downwind site during the first period, because the site is located on a ridge at a higher elevation than the other two sites, and the heterogeneous model assumes a terrain-following ABL.

In summary, the results of this campaign suggest that, while the ABL is not in complete equilibrium with the forest, its effects have propagated through the whole depth of the ABL, which increases the ABL height if the stratification in the free atmosphere above the ABL is weak. However, high wind speeds increased the distance air parcels travel before reaching the ABL top, and reduced the forest's effect on the ABL height.

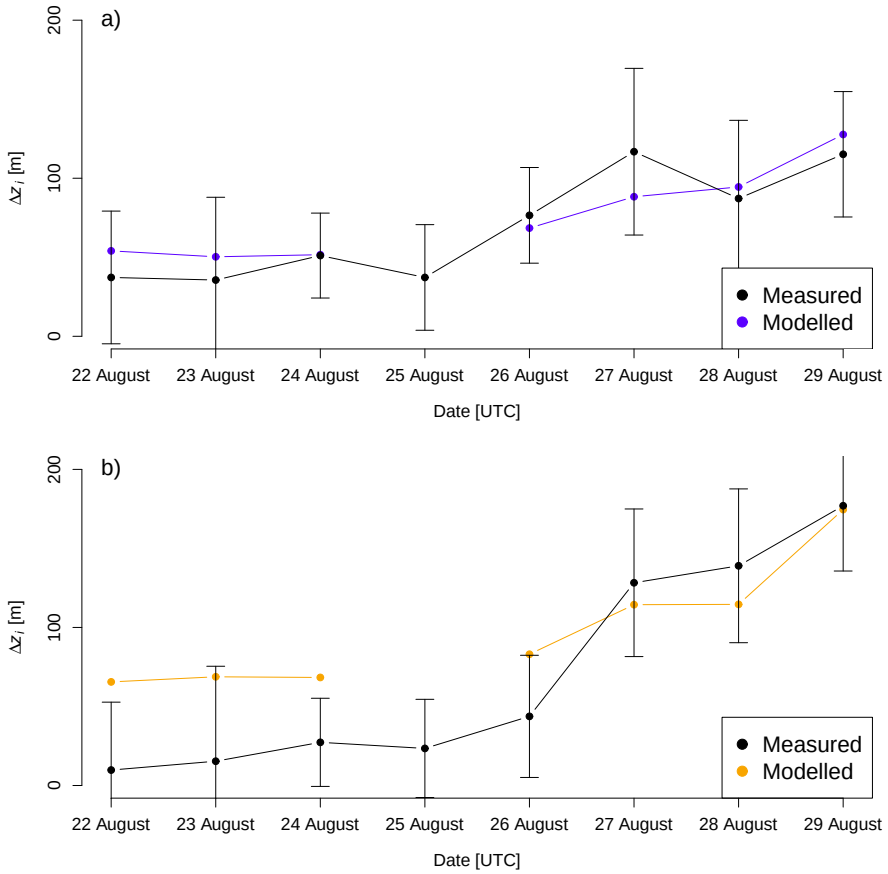

Fig. 5 Increase in the ABL height Δz_i from the upwind site to the forest site (a), and from the upwind site to the downwind site (b) according to lidar measurements (black) averaged from 1000–1300 UTC. The error bars show the sum of the standard error of both instruments. The predicted increase by the heterogeneous model given by Eq. 3 is shown for the forest (blue) and the downwind site (orange). The model was computed with the mean values calculated from 1000–1300 UTC shown in Fig. 6a–f and the value of $\Delta\theta$ from 1200 UTC shown in Fig. 3b.

5 Discussion

The dependency of the general ABL height in Israel on the upper-air inversion by the subtropical anticyclone (Dayan and Rodnizki 1999), as well as the dependency on the sensible heat flux and friction velocity of the underlying surface for homogeneous conditions have been established (e.g. Batchvarova and Gryning 1991; Zilitinkevich et al. 2012). Studies of the ABL height in the presence of surface heterogeneity at shorelines with a stable boundary layer offshore have detected a developing convective internal boundary layer being stabilized in the upper layer by the stable stratification (Garratt 1990;

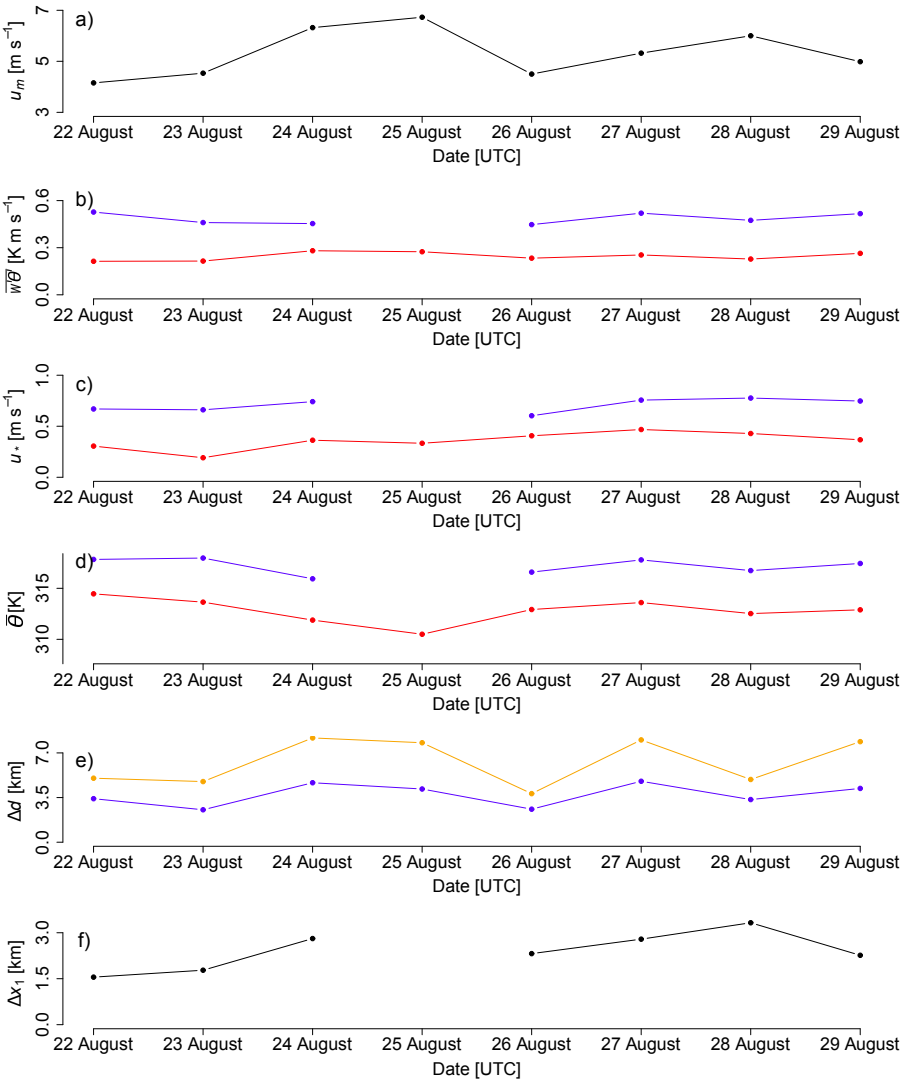

Fig. 6 Time series of the mean values from 1000–1300 UTC of the horizontal wind speed averaged between 250 m and 1000 m above ground level from the Doppler lidars (a), the kinematic sensible heat flux (b), the friction velocity (c), and the potential temperature for 1000 hPa (d) over the forest canopy (blue) and the desert surface (red) derived from the eddy-covariance stations. Panel (e) shows the distance Δd in the wind direction from the forest site (blue) and downwind site (orange) to the forest edge for the geometry explained in Sect. 3.2 and shown in Fig. 1. Panel (f) shows the distance Δx_1 (Eq. 2) air parcels travel before reaching the top of the upwind ABL.

De Tomasi et al. 2011). Similar processes are also applicable at our study site, but are elevated to the ABL top and shifted horizontally downwind, because a well-mixed convective ABL from the desert is advected over the forest where the internal boundary layer deepens rapidly initially. After the forest's effects reach the top of the upwind ABL, the growth of the ABL slows as it penetrates deeper into the free atmosphere. The main driver for the increase in the magnitude of z_i over the forest is the large sensible heat flux from the forest during the day, which often exceeds 600 W m^{-2}, which is twice as high as that of the surrounding shrubland, and results from the lower albedo of the forest compared with the surrounding shrubland (Rotenberg and Yakir 2010). Furthermore, the enhanced roughness of the canopy enhances the magnitude of the heat flux at a lower surface temperature than would be required for a smoother surface (Banerjee et al. 2017). While the large sensible heat fluxes of the forest were present on all days of the campaign, their effect on the value of z_i was suppressed by a more stable stratification in the free atmosphere on some days. High wind speeds also opposed the increase in z_i values by increasing the required distance of the first growth phase through the advected upwind ABL, so that the size of the forest became too small to have any effect. As the two opposing mechanisms affecting the ABL height were independent, the change of the inversion at the boundary-layer top cannot be linked to surface data.

As our results may be influenced by topographical effects and a bias in the detection of the ABL height by the ceilometer and Doppler lidar instruments, both effects are discussed below. The convective boundary layer over complex terrain is expected to be shallower over mountains and deeper over valleys from noon to the evening (De Wekker and Kossmann 2015). The topography of the Yatir forest has a higher elevation at the downwind site compared with the upwind site. As the effects of advection due to the north-western background flow would reduce the magnitude of z_i for the forest and downwind site (De Wekker and Kossmann 2015), the influence of the topography opposes the increase in the magnitude of z_i by the forest, and the height difference between the measurement sites would cause an underestimation of Δz_i values in the measurements for our assumption of a terrain-following ABL.
As we used a different instrument at the downwind site to detect the ABL height than at the forest and upwind sites, a bias between the instruments may distort the results. A comparison of the site-by-site measurements based on Doppler lidar and ceilometer data is presented in Appendix 1, showing that the bias between the instruments is smaller than the increase in the magnitude of z_i due to the effect of the forest. Here, we assume that the bias between the two identical Doppler lidars is smaller than the bias between the Doppler lidar and the ceilometer.

Further limitations of the results arise from the lack of validation data for those periods except at the time of the maximum ABL height, as well as the inability of the heterogeneous model to reproduce fluctuations in Δz_i values on short time scales. The former limitation was partly a precision problem, because the measured Δz_i values before the time of the maximum ABL height

were not significant, and later in the afternoon when residual layers were encountered. Also, the model assumption of a steady state may be violated due to the diurnal cycle of z_i values for those times. The latter limitation results from fluctuations in ABL height due to entrainment, as well as the penetration of thermals into the free atmosphere on short time scales (tens of minutes). This process is not included in the model and, if it were to be included, our measurement set-up would be insufficient for verification because we cannot track individual thermals. Furthermore, the presence of topography with a non-terrain-following ABL impedes correct model estimates.

The results presented herein have shown that the Yatir forest may influence the entire ABL, which does not fully adapt to the forest, whose area is limited. As the planting of the Yatir forest (and other forests in the area) continues, a larger forest will presumably have a stronger impact on the ABL height. Based on the magnitude of the forest's sensible heat flux, an increase in the boundary-layer height by roughly 500 m is predicted by the homogeneous model (Fig. 4). Using the heterogeneous model, we increased the forest size Δd until it yielded the expected 500-m increase of the homogeneous case, which requires a forest on the scale of 72 km, or approximately ten times the size of the current forest.

6 Conclusion

Measurements of the ABL height z_i show that a semi-arid forest with a horizontal extent within the meso-γ-scale surrounded by shrubland can lead to increases in the magnitude of z_i, with the effect advected downwind. The increase in z_i values over the forest is driven by the large sensible heat flux generated in this dry ecosystem, but is constrained by the stratification of the free atmosphere above the ABL height, as well as the wind speed in the mixed layer. Days with a potential-temperature gradient of $\Delta\theta > 9 \times 10^{-3}$ K m^{-1} prevented a significant increase in z_i values over the forest, while an increase of $70 - 260$ m was observed for days with $\Delta\theta < 5 \times 10^{-3}$ K m^{-1}. High wind speeds reduced the increase in the magnitude of z_i due to the shorter adjustment period of the boundary layer to the forest. However, the increase is still detectable for wind speeds up to 6 m s^{-1} during our measurement period. As these findings are based on only eight days of measurements, an extended campaign to yield more robust results over a wider range of meteorological conditions is desirable for future research.

The measured increase in z_i values resulting from the presence of the forest is able to be reproduced with a modified internal boundary-layer model (Eq. 3), which is a new model assuming a vertical transport of the forest's effects at the convective velocity scale w_* to the ABL top while being advected horizontally by the background flow. This implies a linear growth of the forest's internal boundary layer through the advected convective boundary layer. The growth of the ABL due to the change in surface properties follows the square-root law of a conventional slab model for an internal boundary layer, which should be applicable to other forests and to urban heat islands during convective

conditions. In principle, our model can be used for the estimation of the growth of the ABL height for an increase of the surface roughness and heat flux over multiple step changes (e.g. the surrounding rural areas to the suburbs to the city centre), but this needs validation by measurements.

Acknowledgements This research was supported by the German Research Foundation (DFG) as part of the German–Israel collaborative project "Climate feedbacks and benefits of semi-arid forests" (CliFF; grant no. YA 274/1-1 and SCHM 2736/2-1) and the project "Capturing all relevant scales of biosphere–atmosphere exchange — the enigmatic energy balance closure problem" (VH-NG-834), which is funded by the Helmholtz-Association through the President's Initiative and Networking Fund, and by KIT. The permanent and mobile flux facilities at the Yatir forest were supported by the Israel Science Foundation (ISF), JNF-KKL, and the C. Wills and R. Lewis program in Environmental Science. We thank the students Omri Garini (undergraduate assistant) and Avraham Pelner (IT) from the Weizmann Institute for their help during the measurement campaign.

Appendix 1

Adjacent measurements for comparison of the ceilometer and Doppler lidar instruments were conducted during a preliminary campaign on 9 September 2013 at the forest site introduced in Sect. 2.2. The environmental conditions during these measurements were within the range of environmental conditions observed during the campaign in 2015 (Table 3). The ceilometer and Doppler lidar were of the same types used here, but a different instrument. We compare the ABL height retrieval from the Doppler lidar and the ceilometer for the time period from 0800–1500 UTC for the comparison of the ABL height, because of the presence of clouds in the morning. The time series of the ABL height for both instruments are shown in Fig. 7; the time series of z_i values have a Pearson correlation coefficient of 0.96, a mean bias of 30.5 m, and a root-mean-square error of 48.3 m. The reasons for the bias may be different range-gate lengths, different laser wavelengths (which are sensitive to different aerosol sizes), or different window lengths for the vertical smoothing of the backscatter profiles (234 m for the Doppler lidar, and 240 m for the ceilometer).

Table 3 Comparison of environmental conditions during the side-by-side measurement campaign on 9 September 2013 taken from Eder et al. (2015) (left column), and the campaign at the end of August 2015 (right column) at the forest site. The rows show, from top to bottom, the mean values from 0500–1500 UTC of the friction velocity, stability parameter z/L, sensible heat flux and horizontal mean wind speed at 200–500 m above ground level. The value range for the 2015 campaign illustrates the minimum and maximum values.

u_*[m s^{-1}]	0.72	0.57-0.73
$-z/L$	0.20	0.11 - 0.35
H[W m^{-1}]	400.5	368.8 - 434.4
U[m s^{-1}]	6.19	4.60 - 6.52

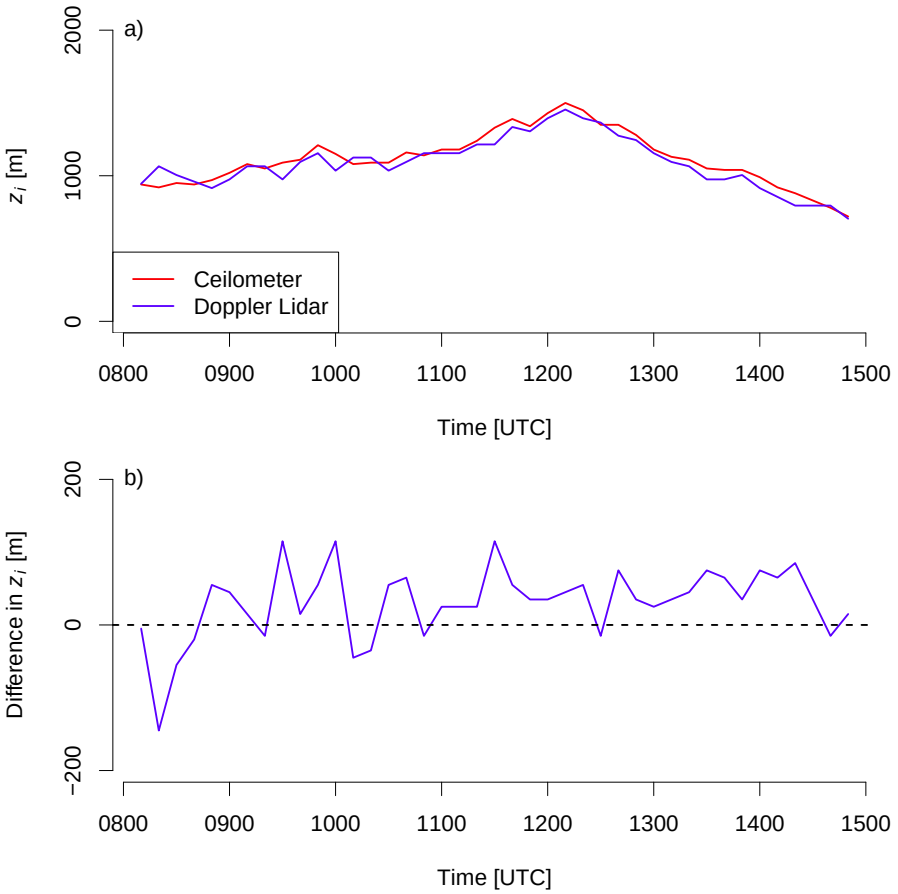

Fig. 7 Time series of ABL heights retrieved from side-by-side measurements of a ceilometer and a Doppler lidar (a) and the difference between the instruments (b).

References

Aubinet M, Vesala T, Papale D (2012) Eddy covariance: a practical guide to measurement and data analysis. Springer Science & Business Media, 438 pp

Baidya Roy S, Avissar R (2000) Scales of response of the convective boundary layer to land-surface heterogeneity. Geophys Res Lett 27(4):533–536

Baldocchi D, Falge E, Gu L, Olson R, Hollinger D, Running S, Anthoni P, Bernhofer C, Davis K, Evans R, Fuentes J, Goldstein A, Katul G, Law B, Lee X, Malhi Y, Meyers T, Munger W, Oechel W, Paw U KT, Pilegaard K, Schmid HP, Valentini R, Verma S, Vesala T, Wilson K, Wofsy S (2001) Fluxnet: A new tool to study the temporal and spatial variability

of ecosystem–scale carbon dioxide, water vapor, and energy flux densities. Bull Am Meteorol Soc 82(11):2415–2434
Banerjee T, Katul G (2013) Logarithmic scaling in the longitudinal velocity variance explained by a spectral budget. Phys Fluids 25(12):125,106
Banerjee T, De Roo F, Mauder M (2017) Explaining the convector effect in canopy turbulence by means of large-eddy simulation. Hydrol Earth Syst Sci 21(6):2987
Barry RG, Chorley RJ (2003) Atmosphere, weather and climate, 8th edn. Routledge, 29 West 35th Street, New York, NY 10001, 421 pp
Batchvarova E, Gryning SE (1991) Applied model for the growth of the daytime mixed layer. Boundary-Layer Meteorol 56(3):261–274
Betts AK, Ridgway W (1989) Climatic equilibrium of the atmospheric convective boundary layer over a tropical ocean. J Atmos Sci 46(17):2621–2641
Browning KA, Wexler R (1968) The determination of kinematic properties of a wind field using doppler radar. J Appl Meteorol 7(1):105–113
Carson D (1973) The development of a dry inversion-capped convectively unstable boundary layer. Q J R Meteorol Soc 99(421):450–467
Dalu GA, Pielke RA, Baldi M, Zeng X (1996) Heat and momentum fluxes induced by thermal inhomogeneities with and without large-scale flow. J Atmos Sci 53(22):3286–3302
Dayan U, Rodnizki J (1999) The temporal behavior of the atmospheric boundary layer in israel. J Appl Meteorol 38(6):830–836
Dayan U, Lifshitz-Goldreich B, Pick K (2002) Spatial and structural variation of the atmospheric boundary layer during summer in Israel - profiler and rawinsonde measurements. J Appl Meteorol 41(4):447–457
De Tomasi F, Miglietta MM, Perrone MR (2011) The growth of the planetary boundary layer at a coastal site: a case study. Boundary-Layer Meteorol 139(3):521–541
De Wekker SFJ, Kossmann M (2015) Convective boundary layer heights over mountainous terrain - a review of concepts. Frontiers in Earth Science 3:77
Deardorff JW (1970) Preliminary results from numerical integrations of the unstable planetary boundary layer. J Atmos Sci 27(8):1209–1211
Dupont S, Brunet Y (2008) Edge flow and canopy structure: a large-eddy simulation study. Boundary-Layer Meteorol 126(1):51–71
Eder F, Serafimovich A, Foken T (2013) Coherent structures at a forest edge: Properties, coupling and impact of secondary circulations. Boundary-Layer Meteorol 148(2):285–308
Eder F, De Roo F, Rotenberg E, Yakir D, Schmid HP, Mauder M (2015) Secondary circulations at a solitary forest surrounded by semi-arid shrubland and their impact on eddy-covariance measurements. Agric For Meteorol 211:115–127
Foken T, Wichura B (1996) Tools for quality assessment of surface-based flux measurements. Agric For Meteorol 78(1):83–105
Garratt J (1990) The internal boundary layer: a review. Boundary-Layer Meteorol 50(1-4):171–203

Gopalakrishnan S, Avissar R (2000) An les study of the impacts of land surface heterogeneity on dispersion in the convective boundary layer. J Atmos Sci 57(2):352–371

Hennemuth B, Lammert A (2006) Determination of the atmospheric boundary layer height from radiosonde and lidar backscatter. Boundary-Layer Meteorol 120(1):181–200

Huang M, Gao Z, Miao S, Chen F, LeMone MA, Li J, Hu F, Wang L (2017) Estimate of boundary-layer depth over Beijing, China, using doppler lidar data during surf-2015. Boundary-Layer Meteorol 162(3):503–522

Juang JY, Porporato A, Stoy PC, Siqueira MS, Oishi AC, Detto M, Kim HS, Katul GG (2007) Hydrologic and atmospheric controls on initiation of convective precipitation events. Water Resour Res 43(3)

Kanani F, Träumner K, Ruck B, Raasch S (2014) What determines the differences found in forest edge flow between physical models and atmospheric measurements? An LES study. Meteorol Z 23(1):33–49

Kang SL, Lenschow D, Sullivan P (2012) Effects of mesoscale surface thermal heterogeneity on low-level horizontal wind speeds. Boundary-Layer Meteorol 143(3):409–432

Kröniger K, Banerjee T, De Roo F, Mauder M (2017) Flow adjustment inside homogeneous canopies after a leading edge - an analytical approach backed by les agricultural and forest meteorology. Agric For Meteorol 255:17–30

Lammert A, Bösenberg J (2006) Determination of the convective boundary-layer height with laser remote sensing. Boundary-Layer Meteorol 119(1):159–170

Lenschow D, Wyngaard JC, Pennell WT (1980) Mean-field and second-moment budgets in a baroclinic, convective boundary layer. J Atmos Sci 37(6):1313–1326

Lotteraner C, Piringer M (2016) Mixing-height time series from operational ceilometer aerosol-layer heights. Boundary-Layer Meteorol 161(2):265–287

Mahrt L (2000) Surface heterogeneity and vertical structure of the boundary layer. Boundary-Layer Meteorol 96(1):33–62

Maronga B, Raasch S (2013) Large-eddy simulations of surface heterogeneity effects on the convective boundary layer during the LITFASS-2003 experiment. Boundary-Layer Meteorol 146(1):17–44

Mauder M, Foken T (2015) Documentation and Instruction Manual of the Eddy-Covariance Software Package TK3 (update). Universität Bayreuth/Abteilung Mikrometeorologie, Bayreuth

Mauder M, Desjardins RL, MacPherson I (2007) Scale analysis of airborne flux measurements over heterogeneous terrain in a boreal ecosystem. J Geophys Res Atmos 112(D13)

Mauder M, Cuntz M, Drüe C, Graf A, Rebmann C, Schmid HP, Schmidt M, Steinbrecher R (2013) A strategy for quality and uncertainty assessment of long-term eddy-covariance measurements. Agric For Meteorol 169:122–135

Moore C (1986) Frequency response corrections for eddy correlation systems. Boundary-Layer Meteorol 37(1-2):17–35

Münkel C, Eresmaa N, Räsänen J, Karppinen A (2007) Retrieval of mixing height and dust concentration with lidar ceilometer. Boundary-Layer Meteorol 124(1):117–128

Orlanski I (1975) A rational subdivision of scales for atmospheric processes. Bull Am Meteorol Soc 56:527–530

Päschke E, Leinweber R, Lehmann V (2015) An assessment of the performance of a 1.5 μm doppler lidar for operational vertical wind profiling based on a 1-year trial. Atmos Meas Tech 8(6):2251

Rotach MW, Wohlfahrt G, Hansel A, Reif M, Wagner J, Gohm A (2014) The world is not flat: Implications for the global carbon balance. Bull Am Meteorol Soc 95(7):1021–1028

Rotenberg E, Yakir D (2010) Contribution of semi-arid forests to the climate system. Science 327(5964):451–454

Rotenberg E, Yakir D (2011) Distinct patterns of changes in surface energy budget associated with forestation in the semiarid region. Glob Change Biol 17(4):1536–1548

Schotanus P, Nieuwstadt F, De Bruin H (1983) Temperature measurement with a sonic anemometer and its application to heat and moisture fluxes. Boundary-Layer Meteorol 26(1):81–93

Seibert P, Beyrich F, Gryning SE, Joffre S, Rasmussen A, Tercier P (2000) Review and intercomparison of operational methods for the determination of the mixing height. Atmos Environ 34(7):1001–1027

Stull RB (1988) An introduction to boundary layer meteorology. Springer, Dordrecht

Stull RB (1992) A theory for mixed-layer-top levelness over irregular topography. In: Proceedings of the 10th AMS Symposium on Turbulence and Diffusion, Portland

Sühring M, Maronga B, Herbort F, Raasch S (2014) On the effect of surface heat-flux heterogeneities on the mixed-layer-top entrainment. Boundary-Layer Meteorol 151(3):531–556

Sun J, Lenschow DH, Mahrt L, Nappo C (2013) The relationships among wind, horizontal pressure gradient, and turbulent momentum transport during CASES-99. J Atmos Sci 70(11):3397–3414

Tennekes H (1973) A model for the dynamics of the inversion above a convective boundary layer. J Atmos Sci 30(4):558–567

Träumner K, Kottmeier C, Corsmeier U, Wieser A (2011) Convective boundary-layer entrainment: Short review and progress using doppler lidar. Boundary-Layer Meteorol 141(3):369–391

Träumner K, Wieser A, Ruck B, Frank C, Röhner L, Kottmeier C (2012) The suitability of doppler lidar for characterizing the wind field above forest edges. Forestry 85(3):399–412

Venkatram A (1977) A model of internal boundary-layer development. Boundary-Layer Meteorol 11(4):419–437

Wilczak JM, Oncley SP, Stage SA (2001) Sonic anemometer tilt correction algorithms. Boundary-Layer Meteorol 99(1):127–150

Wu Y, Nair US, Pielke RA, McNider RT, Christopher SA, Anantharaj VG (2009) Impact of land surface heterogeneity on mesoscale atmospheric dispersion. Boundary-Layer Meteorol 133(3):367–389

Zhong S, Doran JC (1995) A modeling study of the effects of inhomogeneous surface fluxes on boundary-layer properties. J Atmos Sci 52(17):3129–3142

Zilitinkevich SS, Tyuryakov SA, Troitskaya YI, Mareev EA (2012) Theoretical models of the height of the atmospheric boundary layer and turbulent entrainment at its upper boundary. Izv Atmos Ocean Phys 48(1):133–142

Scalewise invariant analysis of the anisotropic Reynolds stress tensor for atmospheric surface layer and canopy sublayer turbulent flows

Peter Brugger,[1,*] Gabriel G. Katul,[2,3,1] Frederik De Roo,[1] Konstantin Kröniger,[1] Eyal Rotenberg,[4] Shani Rohatyn,[4] and Matthias Mauder[1]

[1]*Karlsruhe Institute of Technology (KIT), Institute of Meteorology and Climate Research - Atmospheric Environmental Research (IMK-IFU), Kreuzeckbahnstraße 19, 82467 Garmisch-Partenkirchen, Germany*
[2]*Nicholas School of the Environment, Box 80328, Duke University, Durham, North Carolina 27708, USA*
[3]*Department of Civil and Environmental Engineering, Duke University, Durham, North Carolina 27708, USA*
[4]*Weizmann Institute of Science (WIS), Faculty of Chemistry, Department of Earth and Planetary Sciences, 234 Herzl Street, Rehovot 7610001, Israel*

(Received 21 December 2017; published 24 May 2018)

Anisotropy in the turbulent stress tensor, which forms the basis of invariant analysis, is conducted using velocity time series measurements collected in the canopy sublayer (CSL) and the atmospheric surface layer (ASL). The goal is to assess how thermal stratification and surface roughness conditions simultaneously distort the scalewise relaxation towards isotropic state from large to small scales when referenced to homogeneous turbulence. To achieve this goal, conventional invariant analysis is extended to allow scalewise information about relaxation to isotropy in physical (instead of Fourier) space to be incorporated. The proposed analysis shows that the CSL is more isotropic than its ASL counterpart at large, intermediate, and small (or inertial) scales irrespective of the thermal stratification. Moreover, the small (or inertial) scale anisotropy is more prevalent in the ASL when compared to the CSL, a finding that cannot be fully explained by the intensity of the mean velocity gradient acting on all scales. Implications to the validity of scalewise Rotta and Lumley models for return to isotropy as well as advantages to using barycentric instead of anisotropy invariant maps for such scalewise analysis are discussed.

DOI: 10.1103/PhysRevFluids.3.054608

I. INTRODUCTION

The classical treatment of turbulence in the atmospheric surface layer (ASL) and the roughness sublayer (CSL) above canopies has primarily focused on distortions to the mean velocity profile caused by the presence of roughness elements and thermal stratification [1–9]. Surface roughness effects and thermal stratification modify the components of the Reynolds stress tensor, as evidenced by a large number of experiments and simulations [5,10–19]. These modifications are expected to lead to differences in kinetic energy distribution among velocity components comprising the stress tensor. Such differences in energy anisotropy has been previously used to explore the sensitivity of turbulent structures to surface boundary conditions such as roughness changes [20–25] or thermal stratification [26]. However, the route of how the anisotropy at large scales relaxes to quasi-isotropic state at small scales remains a subject of research [27–31]. The juxtaposition of these questions and studies to ASL and CSL turbulence using field measurements is the main motivation for the work here.

Exchanges of turbulent kinetic energy among the three spatial components occur through interactions between fluctuating velocities and pressure. Starting from an anisotropic stress tensor

*peter.brugger@kit.edu

$\overline{u_i u_j}$, these exchanges have been labeled as return to isotropy; when mean flow gradients are removed or suppressed, they describe the expected state that turbulence relaxes to. Here, u_i are the turbulent or fluctuating velocity components along x_i, where x_1 (or x), x_2 (or y), and x_3 (or z) represent the longitudinal, lateral, and vertical directions, respectively, the overbar denotes time averaging, and $\overline{u_i} = 0$. Much progress has been made by exploring connections between $\overline{u_i u_j}$ and the so-called invariant analysis [22,30,32–36]. Such connections resulted in nonlinear models for the slow part of the pressure-strain correlation and highlighted distinct routes along which turbulence relaxes to isotropic conditions [27,33,34]. These routes have been succinctly summarized in what are labeled as anisotropy invariant maps (AIM), proposed by Lumley [33,34]. Invariant analysis is based on the anisotropic second-order normalized stress tensor related to $\overline{u_i u_j}$ by

$$a_{ij} = \frac{\overline{u_i u_j}}{2k} - \frac{1}{3}\delta_{ij}, \quad k = \frac{\overline{u_m u_m}}{2}, \tag{1}$$

where k is the mean turbulent kinetic energy and δ_{ij} is the Kronecker delta. This tensor has three invariants: $I_1 = a_{ii} = 0$, here and $I_2 = a_{ij}a_{ji}$ and $I_3 = a_{ij}a_{jn}a_{ni}$, which are independent of the coordinate rotation of the reference system and can be linked to the eigenvalues of a_{ij}. Invariant maps feature I_3 (abscissa) versus $-I_2$ (ordinate) along with bounds imposed by realizability constraints on $\overline{u_i u_j}$ (e.g., $\det[a_{ij}] \geqslant 0$, where $\det[\cdot]$ is the determinant). The I_2 represents the degree of anisotropy whereas I_3 represents the nature (or topology) of the anisotropy. The AIM approach suggests that anisotropy in $\overline{u_i u_j}$ may be 1-component (rodlike energy distribution), 2-component (disklike energy distribution), or 3-component, of which the isotropic state (spherical energy distribution) is a limiting case. Depending on the sign of I_3, progression from 1-component or 2-component to 3-component follows an axisymmetric expansion or contraction on the AIM when the source of inhomogeneity (e.g., mean flow gradients) is removed until isotropy is achieved [34]. As noted earlier, the AIM domain bounds all realizable Reynolds stress invariants [22,34,37,38], thereby making AIM an effective visual tool to track anisotropy at different heights in boundary layer turbulence. In fact, the AIM proved to be effective at demonstrating that rough-wall turbulence appears more isotropic than its smooth-wall counterpart for the same Reynolds numbers [21]. Experiments and simulations [25] also reported that the AIM signature for smooth wall turbulence appears well defined and robust to variations in Reynolds number. The same experiments further showed that turbulent flows over three-dimensional (3D) k-type roughness appear more isotropic than flows over their 2D k-type roughness counterparts throughout the boundary layer [25].

An alternative to the AIM representation is the barycentric map (BAM), which offers a number of advantages over AIM, such as nondistored visualization of anisotropy and weighting of the limiting states, as discussed elsewhere [32]. However, AIM and BAM representations are connected by transformations derived from the three eigenvalues of a_{ij}. Invariant analysis in a_{ij} assumes that anisotropy is inherently a large-scale feature, and finer scales become isotropic and decoupled from their anisotropic large scales counterpart. How anisotropy in a_{ij} is destroyed as eddy sizes or scales become smaller remains a subject of inquiry, especially in vertically inhomogeneous flows characterizing the ASL and CSL of the atmosphere. The ASL and CSL experience mechanical production of k through interactions between the turbulent shear stress and the mean velocity profile. However, additional sources (or sinks) of k occur through surface heating (or cooling) and their associated thermal stratification. Above and beyond these two processes, canopy roughness effects introduce additional length scales (e.g., adjustment length and shear length scales) when describing flow statistics in the CSL [5,39].

Two early pioneering attempts to extend invariant analysis across scales were conducted in the Fourier domain. One utilized numerical simulations of isotropic turbulence [28]. The other considered 3-component velocity time series collected in a pipe at multiple distances from the pipe wall and at two bulk Reynolds numbers [23]. The simulation study showed that small-scale anisotropy in Reynolds stresses persisted and was traced back to nonlocal triad interactions that appear not efficient at destroying an initial spanwise energy injection. The pipe flow experiments showed that, at large scales, near-wall structures exhibit "rod-like" (or prolate) energy distribution whereas "disk-like"

(or oblate) energy distribution characteristics were reported as the buffer region is approached. Approximate isotropic states were reported as the pipe center is approached, where the mean velocity gradients approach zero (by virtue of symmetry). Another recent study [26] also extended aspects of invariant analysis across scales in the Fourier domain to explore how thermal stratification modifies isotropic and anisotropic states above an urban canopy. This work showed that the relaxation rate towards local isotropy varies with thermal stratification. Specifically, unstable atmospheric stability appears to be closer to the isotropic state than its near-neutral or stable counterpart at a given scale or wave number. A relation was suggested between the scale over which maximum isotropy is attained and an outer length scale derived from temperature statistics [26].

The work here uses invariant analysis across scales in the ASL and CSL to explore the simultaneous role of roughness contrast and thermal stratification on anisotropy relaxation towards quasi-isotropic conditions. How anisotropy in a_{ij} produced at large scales varies with thermal stratification in the ASL and CSL and how such a large-scale anisotropic state relaxes to quasi-isotropic conditions at progressively smaller scales frame the scope of the work. The novelties of the analysis proposed here over prior work [23,26] are that (1) velocity differences in physical space are used instead of spectral and cospectral analysis, and (2) both AIM and BAM measures of anisotropy are employed and their outcome compared to conventional local isotropy analysis. Advantages to conducting the analysis in physical space instead of spectral space are discussed.

With regards to the experimental design, the 3-component velocity time series were simultaneously collected in the CSL above a tall forest and in the ASL above an adjacent desert-like shrubland. The runs spanned a wide range of atmospheric stability conditions as characterized by the atmospheric stability parameter. Distances to the surface or zero-plane displacement (in the case of the forest) were similar for both setups and were chosen to be commensurate with the aforementioned experiment on the urban surface layer [26]. It is envisaged that the analysis reported here offers a new perspective on the relative sensitivity of turbulent structures to roughness modifications and thermal stratification, especially at the crossover from large (or integral) scales to inertial scales.

II. METHOD OF ANALYSIS

A. Definitions and nomenclature

Any three-dimensional second-rank tensor σ_{ij} has three independent invariant quantities associated with it, which can be determined from the eigenvalues of σ_{ij}. The eigenvalues (λ) are computed from the determinant $\det[\sigma_{ij} - \lambda\delta_{ij}] = 0$. Expanding the determinant of the matrix

$$\begin{bmatrix} \sigma_{11} - \lambda & \sigma_{12} & \sigma_{13} \\ \sigma_{21} & \sigma_{22} - \lambda & \sigma_{23} \\ \sigma_{31} & \sigma_{32} & \sigma_{33} - \lambda \end{bmatrix}$$

and setting it to zero yields the characteristic equation that defines the invariants and is given by [40]

$$\det[\sigma_{ij} - \lambda\delta_{ij}] = -\lambda^3 + I_1\lambda^2 - I_2\lambda + I_3 = 0, \tag{2}$$

where

$$I_1 = \sigma_{kk} = \mathrm{tr}[\sigma], \tag{3}$$

$$I_2 = \tfrac{1}{2}(\sigma_{ii}\sigma_{jj} - \sigma_{ij}\sigma_{ji}), \tag{4}$$

$$I_3 = \det[\sigma_{ij}], \tag{5}$$

with $\mathrm{tr}[\cdot]$ being the trace of σ_{ij}. When $\sigma_{ij} = a_{ij}$, symmetry insures that Eq. (2) has three real roots (the eigenvalues) labeled as λ_1, λ_2, and λ_3. The principal stresses are defined as components of σ_{ij} when the basis is changed so that the shear stress components become zero and σ_{ij} becomes a 3×3 diagonal matrix whose elements are σ_1, σ_2, and σ_3. These principal stresses are the three eigenvalues

ordered by magnitude using $\sigma_1 = \max(\lambda_1,\lambda_2,\lambda_3)$, $\sigma_3 = \min(\lambda_1,\lambda_2,\lambda_3)$, and $\sigma_2 = I_1 - \sigma_1 - \sigma_3$. The σ_1, σ_2, and σ_3 are independent of the coordinate basis in which the components of σ_{ij} are originally derived, which is advantageous in ASL and CSL field studies where large variations in wind directions are unavoidable. Applying the diagonal form of σ_{ij} to the definitions of the three invariants given by Eq. (2) yields the following simplified expressions:

$$I_1 = \sigma_1 + \sigma_2 + \sigma_3, \tag{6}$$

$$I_2 = \sigma_1\sigma_2 + \sigma_2\sigma_3 + \sigma_3\sigma_1, \tag{7}$$

$$I_3 = \sigma_1\sigma_2\sigma_3. \tag{8}$$

These definitions directly apply to a_{ij} or any other second-rank tensor such as the strain rate [40,41] and others relevant to vorticity and dissipation [20]. One advantage to using a_{ij} here instead of $\overline{u_i u_j}$ for invariant analysis is that $I_1 = \mathrm{tr}[\mathrm{a_{ij}}] = \mathrm{a_{11}} + \mathrm{a_{22}} + \mathrm{a_{33}} = 0$ and only the second and third invariants are required.

The BAM framework makes use of the fact that a_{ij} can be expressed as a linear combination of three limiting states (1-component, 2-component, or 3-component). That is, a_{ij} can be decomposed into $C_{1c}a_{1c} + C_{2c}a_{2c} + C_{3c}a_{3c}$, where C_{1c}, C_{2c}, and C_{3c} are determined from the eigenvalues using [32]

$$C_{1c} = \lambda_1 - \lambda_2, \tag{9}$$

$$C_{2c} = 2(\lambda_2 - \lambda_3), \tag{10}$$

$$C_{3c} = 3\lambda_3 + 1, \tag{11}$$

and a_{1c}, a_{2c}, and a_{3c} are 3×3 diagonal matrices with diagonal elements $[2/3,-1/3,-1/3]$ (1-component limiting state), $[1/6,1/6,-1/3]$ (2-component limiting state), and $[0,0,0]$ (3-component limiting state). In the BAM representation, C_{1c}, C_{2c}, and C_{3c} determined from λ_1, λ_2, and λ_3 indicate how much each turbulent state is contributing to a point situated in the map. The map itself can be constructed within an equilateral triangle with vertices being the three limiting states defined by coordinates $(x_{1c},y_{1c}) = (1,0)$, $(x_{2c},y_{2c}) = (-1,0)$, and $(x_{3c},y_{3c}) = (0,\sqrt{3})$. Once these limiting states are set, a normalization is applied so that $C_{1c} + C_{2c} + C_{3c} = 1$ and the coordinates of any point on the map $(x_{\mathrm{BAM}},y_{\mathrm{BAM}})$ can be determined from

$$x_{\mathrm{BAM}} = C_{1c}x_{1c} + C_{2c}x_{2c} + C_{3c}x_{3c}, \tag{12}$$

$$y_{\mathrm{BAM}} = C_{1c}y_{1c} + C_{2c}y_{2c} + C_{3c}y_{3c}. \tag{13}$$

As discussed elsewhere [32], an equilateral triangle shaped BAM does not introduce any visual bias of the limiting states as is the case for the AIM. Randomly distributed points within BAM, when converted to AIM, result in visual clustering near the isotropic or 3-component state primarily because of the nonlinearity in the transformation from BAM to AIM.

B. Measures of anisotropy

A scalar measure of anisotropy in the AIM is the shortest or linear distance to the isotropic state. This distance was determined from I_2 and I_3 via [22,33]

$$F = 1 + 27I_3 + 9I_2. \tag{14}$$

Isotropic turbulence is strictly attained when both $I_2 = I_3 = 0$ and $F = 1$, whereas $F = 0$ occurs along the linear boundary describing the 2-component state. The distance F was reported to be a function of distance from a solid boundary for various turbulent boundary layer flows [22–25]. At all

distances from the boundary, F was smaller for turbulent flows over smooth walls when compared to all types of rough-wall cases [24,25].

In the BAM, the distance to the isotropic state is [32]

$$C_{\text{ani}} = -3\lambda_3. \tag{15}$$

This measure has not been extensively used before, and is employed along with F for the data collected in the ASL and CSL.

C. Scalewise analysis

The scalewise analysis of AIM and BAM uses the structure function approach (in physical or r space) instead of Fourier space. The overall premise is similar to what was proposed earlier [28] except that structure functions ensure integrability and minimize other limitations discussed elsewhere for spectral and co-spectral versions [23]. The premise of the scalewise AIM or BAM analysis is to replace $\overline{u_i u_j}$ by

$$D_{ij}(r) = \tfrac{1}{2}\overline{\Delta u_i(r)\Delta u_j(r)}, \tag{16}$$

where $\Delta u_k(r) = u_k(x+r) - u_k(x)$, and r is the separation distance along the longitudinal (or x_1) direction determined from time increments and Taylor's frozen turbulence hypothesis [42,43], which is conventional when interpreting time series in field experiments. Equation (16) has a number of desirable limits. To illustrate, consider its expansion given as

$$D_{ij}(r) = \tfrac{1}{2}(\overline{u_i(x+r)u_j(x+r)} + \overline{u_i(x)u_j(x)}) - \tfrac{1}{2}(\overline{u_i(x+r)u_j(x)} + \overline{u_i(x)u_j(x+r)}). \tag{17}$$

For planar homogeneous flows and at $r/L_I \gg 1$, $D_{ij}(r) \approx \overline{u_i(x)u_j(x)}$ [or $D_{ij}(r) \approx \overline{u_i(x+r)u_j(x+r)}$], where L_I is the integral length scale of the flow (to be defined later). Hence, $D_{ij}(r)$ recovers all the properties of the stress tensor at large scales. For $r \to 0$, $D_{ij}(r) \to 0$ and ensures no energy and stress contributions at very small scales. The use of $D_{ij}(r)$ is rather convenient because expected scaling laws for inertial subrange eddies are known. For example, when $i = 1$ and $j = 1$, $D_{11}(r)$ becomes the longitudinal velocity structure function, which measures the integrated energy content at scale r. It is noted here that $rdD_{11}(r)/dr \propto k_1 E_{11}(k_1)$, where k_1 is the one-dimensional wave number along direction x_1 and $E_{11}(k_1)$ is the longitudinal velocity energy spectrum. Likewise, for $r/L_I \gg 1$, $D_{11}(r) \to \overline{u_1 u_1}$. Because structure functions measure integrated energy content at a given scale r, the singularity issues in Fourier domain noted elsewhere [23] are bypassed. For locally isotropic turbulence and for $\eta/L_I \ll r/L_I \ll 1$, Kolmogorov (or K41) scaling is expected to hold in the ASL and yields the following for the componentwise structure functions:

$$D_{11}(r) = C_{o,1}\overline{\epsilon}^{2/3} r^{2/3}, \tag{18}$$

$$D_{22}(r) = C_{o,2}\overline{\epsilon}^{2/3} r^{2/3}, \tag{19}$$

$$D_{33}(r) = C_{o,3}\overline{\epsilon}^{2/3} r^{2/3}, \tag{20}$$

where $\eta = (\nu^3/\overline{\epsilon})^{1/4}$ is the Kolmogorov microscale, ν is the fluid kinematic viscosity, $C_{o,2} = C_{o,3} = (4/3)C_{o,1}$, $C_{o,1} = 2$, and $\overline{\epsilon}$ is the mean dissipation rate of k. One undesirable outcome to using $D_{ij}(r)$ is its nonzero trace at any r. As was the case with a_{ij} and $\overline{u_i(x)u_j(x)}$, this outcome may be circumvented by evaluating

$$A_{ij}(r) = \frac{D_{ij}(r)}{D_{kk}(r)} - \frac{1}{3}\delta_{ij}. \tag{21}$$

The AIM and BAM as well as $F(r)$ and $C_{\text{ani}}(r)$ can now be computed for the ASL and CSL velocity time series once the eigenvalues of $D_{ij}(r)$ or $A_{ij}(r)$ are determined for each $r > 0$.

D. Comparison with a reference model

To compare the computed scalewise variations of I_2 and I_3 in the CSL and ASL with a well-studied turbulent state, homogeneous turbulence (i.e., lacking any mean flow gradients) is selected as a reference. Once the mean flow gradients are removed for this reference state, the decay rates of I_2 and I_3 are shown to reasonably follow a quadratic model given by [27]

$$\frac{dI_2}{d\tau} = -2(B_1 - 2)I_2 + 2B_2 I_3, \tag{22}$$

$$\frac{dI_3}{d\tau} = -3(B_1 - 2)I_3 + \frac{1}{2}B_2 I_2^2, \tag{23}$$

where τ is a relaxation time scale, and $B_1 = 3.4$ and $B_2 = 3(B_1 - 2)$ are constants determined by fitting this model to a wide range of experiments. For $B_2 = 0$, this system recovers the Lumley model [33] (i.e., uncoupled equations), and for $B_2 = 0$ and $I_3 = 0$, the classical Rotta model is recovered. Hence, finite B_2 and I_3 offer a clear indication that the linear Rotta model may not be adequate to describe the trajectory towards isotropy. The two ordinary differential equations can now be combined to yield

$$\frac{dI_2}{dI_3} = \frac{-2(B_1 - 2)I_2 + 2B_2 I_3}{-3(B_1 - 2)I_3 + \frac{1}{2}B_2 I_2^2}, \tag{24}$$

which can be solved to yield $-I_2$ as a function of I_3 (i.e., the trajectory on the AIM) without requiring the determination of time τ provided τ is sufficiently large to attain the isotropic state. The trajectories of this model (in AIM or BAM) are simply computed here to illustrate how homogeneous turbulence relaxes to the isotropic state once the mean flow gradients (that are prevalent in ASL and CSL) are suppressed. The initial conditions to equation (24) are the measured I_2 and I_3 in the CSL or ASL as determined for $r/L_I \gg 1$.

III. EXPERIMENTS

A. Research site

The experiments were conducted at the Yatir Forest in southern Israel, which is a planted evergreen pine forest surrounded by a sparse desert-like shrubland [44]. The trees were planted in the late 1960s and now cover an approximate area of 28 km^2 [44]. The primary tree species of the forest is *Pinus halepensis* and the shrubland has scattered herbaceous annuals and perennials (mainly *Sarcopoterium spinosum*). The albedo of the forest is low (=12.5%) when compared to the shrubland (=33.7%). In the absence of latent heat fluxes (as is the case in the extensive dry season), this albedo contrast leads to sensible heat fluxes up to 800 W m^{-2} during the day over the forest, which can be twice as high as those of the surrounding shrubland [45]. The higher roughness length of the forest also creates friction velocities (u_*) of up to 0.8 m s^{-1}, which are twice as high as those above the shrubland [45]. These sensible heat flux and friction velocity differences between the forest and shrubland do impact the generation of k. To illustrate, a stationary and planar-homogeneous flow at high Reynolds number in the absence of subsidence is considered. The k budget for such an idealized flow is

$$\frac{\partial k}{\partial t} = 0 = -\overline{u_1 u_3}\frac{dU}{dz} + \beta_o g\overline{u_3 T'} + P_D + T_T - \bar{\epsilon}, \tag{25}$$

where t is time, and the five terms on the right-hand side of Eq. (25) are mechanical production, buoyant production (or destruction), pressure transport, turbulent transport of k, and viscous dissipation of k, respectively; β_o is the thermal expansion coefficient for air ($\beta_o = 1/T$, T is mean air temperature and T' is temperature fluctuation), g is the gravitational acceleration, $-\overline{u_1 u_3} = u_*^2$ is the turbulent kinematic shear stress near the surface, $\overline{u_3 T'}$ is the kinematic sensible heat flux from (or to) the surface, and U is the mean longitudinal velocity. The $\rho_a C_p \overline{u_3 T'}$ defines the sensible heat flux in energy units (W m^{-2}), with ρ_a and C_p being the mean air density and the specific heat

capacity of dry air at constant pressure, respectively. When $\overline{u_3T'} > 0$, buoyancy is responsible for the generation of k and the flow is classified as unstable. When $\overline{u_3T'} < 0$, the flow is classified as stable and buoyancy acts to diminish the mechanical production of k. The relative significance of the mechanical production to the buoyancy generation (or destruction) in the TKE budget may be expressed as [10,13,14]

$$-\overline{u_1u_3}\frac{dU}{dz} + \beta_o g\overline{u_3T'} = \frac{u_*^3}{\kappa z}\left[\phi_m(\zeta) + \frac{\kappa z\beta_o g\overline{u_3T'}}{u_*^3}\right] = \frac{u_*^3}{\kappa z}[\phi_m(\zeta) - \zeta], \tag{26}$$

where

$$\frac{\kappa z}{u_*}\frac{dU}{dz} = \phi_m(\zeta), \quad \zeta = \frac{z}{L}, \quad L = -\frac{u_*^3}{\kappa g\beta_o\overline{u_3T'}}, \tag{27}$$

and $\phi_m(\zeta)$ is known as a stability correction function reflecting the effects of thermal stratification on the mean velocity gradient [$\phi_m(0) = 1$ recovers the von Karman–Prandtl logarithmic law], $\kappa \approx 0.4$ is the von Karman constant, and L is known as the Obukhov length [46] as described by the Monin and Obukhov similarity theory [1,2,7,9]. The physical interpretation of L is that it is the height at which mechanical production balances the buoyant production or destruction when $\phi_m(\zeta)$ does not deviate appreciably from unity. For a neutrally stratified atmospheric flow, $|L| \to \infty$ and $|\zeta| \to 0$. The sign of L reflects the direction of the heat flux, with negative values of L corresponding to upward heat fluxes (unstable atmospheric conditions) and positive values L corresponding to downward heat flux (stable atmosphere).

B. Instruments and measurements

High-frequency measurements of the turbulent velocity components were conducted concurrently in the CSL over the forest and the ASL of the surrounding shrubland desert ecosystem. The measurements in the ASL were conducted northwest of the forest above the shrubland with a mobile mast positioned at latitude 31.3757°, longitude 35.0242°, and 620 m above sea level. The mast was equipped with a R3-100 ultrasonic anemometer from Gill Instruments Ltd. (Lymington, Hampshire, UK) sampling three orthogonal velocity components with a frequency of 20 Hz. The ultrasonic anemometer was mounted at a height of 9 m above ground surface. The measurements in the CSL were conducted above the forest canopy with a R3-50 ultrasonic anemometer from Gill Instruments with a measurement frequency of 20 Hz (latitude 31.3453°, longitude 35.0522°, 660 m above sea level). The manufacturer states for both ultrasonic anemometers an accuracy <1% for mean wind speeds below 32 m s^{-1}. Wind tunnel and atmospheric comparison to hot-film anemometers showed an accuracy of 2% for the mean wind speed, 9% for variances, and 23% for covariances [47]. The sonic anemometer was mounted 19 m above the ground surface on a meteorological tower. The mean height of the trees around the tower is 10 m, placing the sonic anemometer some 9 m above the canopy top and commensurate to the setup of the urban roughness study previously discussed [26]. The anemometer sonic path length is 0.15 m; hence, separation distances smaller than 0.3 m are not used as they are influenced by instrument averaging. Data from the period 17–23 August 2015 are used here. During this period, the Yatir forest experienced a subtropical ridge, an area of general subsidence in the troposphere connected to the sinking branch of the Hadley cell [48]. The horizontal air pressure gradients were controlled by a heat-induced surface low, the Persian trough, to the east [49]. This led to stationary weather conditions with a main wind direction from the northwest and cloud-free conditions with a radiation driven diurnal cycle of the boundary layer height during the campaign.

C. Post-processing

The measured u_i time series were first separated into nonoverlapping 30-minute runs, and turbulent flow statistics were computed using the 30-minute averaging period per run. Threshold filters of 50 $\mathrm{m\,s^{-1}}$ for the horizontal wind components and 10 $\mathrm{m\,s^{-1}}$ for the vertical component were applied, and spikes were removed by a five-standard-deviation threshold. Then gaps in the time series were linearly interpolated when the total gap length was less than 5% (otherwise the 30-minute run was discarded). The interpolated data set was rotated into the mean wind direction using a standard double rotation ($\overline{u_3} = \overline{u_2} = 0$ and $U \neq 0$) and the mean value was subtracted to obtain turbulent fluctuations. Further quality control was conducted using stationary tests and integral turbulence characteristic tests described elsewhere [50], and only intervals with the best quality metrics were used [51]. For comparison purposes, only intervals where both sites had simultaneous high quality measurements were used. After such post-processing, 65 runs remained for investigating the anisotropy in the ASL and CSL.

IV. RESULTS AND DISCUSSION

To address the study objective, the results are presented as follows: the a_{ij} components computed from Eq. (1) for the ASL and CSL and their dependence on ζ are first presented. Similarities between anisotropy in componentwise turbulent kinetic energy and integral scales along the x_1,x_2,x_3 are also featured. Next, attainment of local isotropy at finer scales is explored by comparing measured $D_{11}(r)$, $D_{22}(r)$, and $D_{33}(r)$ with predictions from K41 scaling and corollary isotropic measures. The scalewise development of the anisotropic stress tensor $[A_{ij}(r)]$ for the ASL and CSL, as determined from Eq. (21), is then discussed using AIM and BAM. Predictions from Eq. (24) are displayed as references to illustrate expected pathways by which $A_{ij}(r)$ approaches its isotropic state with decreasing r for homogeneous turbulence. Finally, the two scalewise measures $F(r)$ and $C_{\mathrm{ani}}(r)$ are presented as a function of r for CSL and ASL flows across a wide range of ζ values. The focus here is on two types of scales: (i) the largest r for which local isotropy is attained, and (ii) the smallest r over which the return to isotropy begins to be efficient. These two scales are then contrasted for ASL and CSL flows and across ζ values, thereby completing the sought objective.

A. Conventional analysis

Unsurprisingly, the computed a_{ij} components exhibit large anisotropy for both ASL and CSL flows. In particular, the streamwise a_{11} and the cross-streamwise a_{22} attain positive values (i.e., more energy than isotropic predictions) as evidenced by Figs. 1(a) and 1(b) and negative values for the vertical a_{33} [Fig. 1(c)] when compared to the expected $Y = 0$ designating the isotropic state. The streamwise and cross-stream components show that the anisotropy for near-neutral conditions in the CSL is between the vertical and streamwise components. The sum of the two horizontal components ($a_{11} + a_{22} = -a_{33}$), which accounts for much of the k, is expected to provide a robust measure of the anisotropy between the horizontal and vertical components. The mean values for a_{33} differ between CSL and ASL at a 95% confidence level, confirming a significantly larger anisotropy in the ASL when compared to its CSL counterpart. The analysis here also shows that a_{33} and a_{23} are not sensitive to variations in ζ for both ASL and CSL flows. The only component of a_{ij} that exhibits variation with ζ is a_{13} in the CSL, which has a slope significantly different from zero at a 95% confidence level. The a_{13} is small in the ASL by comparison to its CSL values. The scatter of most data points in Fig. 1 can be explained by the measurement accuracy, but in the cases of a_{11} and a_{22} the accuracy alone cannot explain the variation and it is likely that nonstationary wind directions affect those components. Direct numerical simulations of homogeneous turbulent shear flows showed more isotropy for weaker shear [52], which agrees with our experiments, where the CSL appears more isotropic and has weaker shear parameter S^* compared to its ASL counterpart for near-neutral conditions. Moreover, the simulation results [52] showed patterns among the components of a_{ij} that are similar to the atmospheric measurements reported in Fig. 1 for a near-neutral ASL. The S^* here varied from 35 to 83 compared to their highest, $S^* = 27$, where $S^* = Sk^2/\epsilon$ with $S = U/(z - d)$.

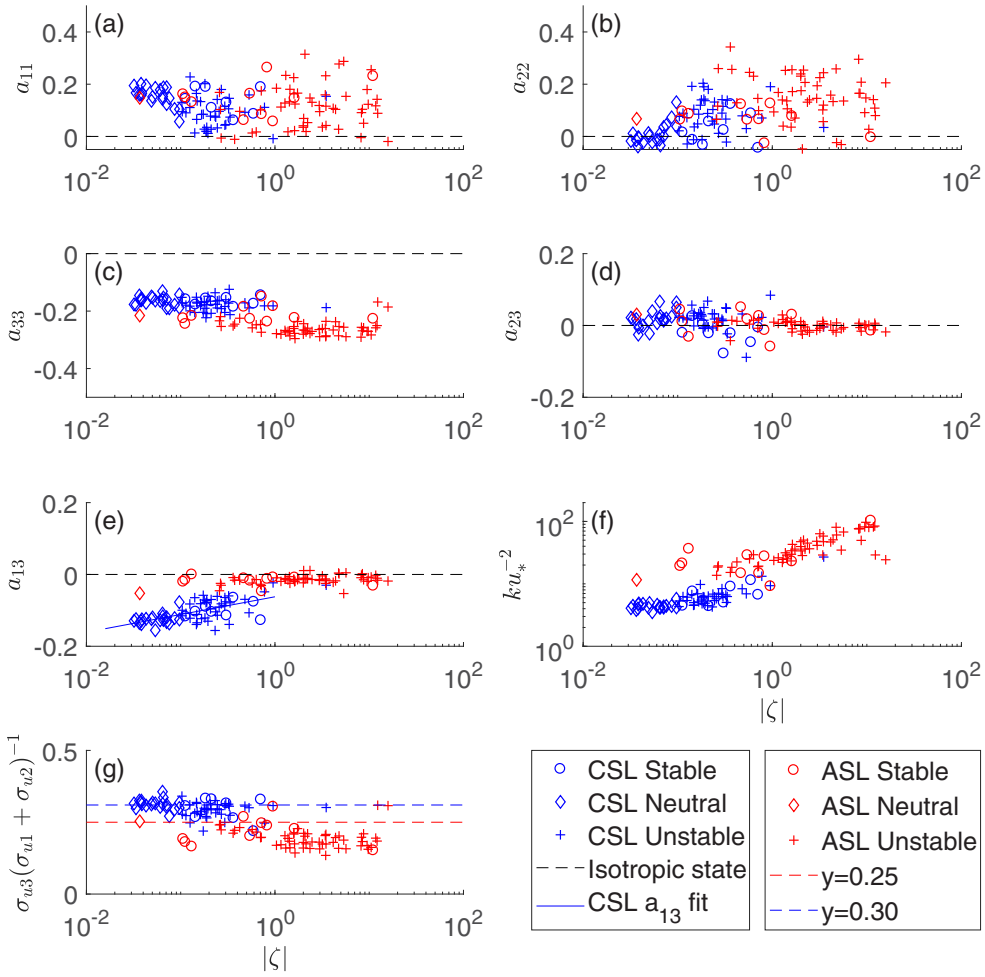

FIG. 1. The measured components of the anisotropy tensor a_{ij} are shown as a function of the absolute value of the stability parameter $|\zeta| = |(z-d)/L|$ [(a), (b), (c), and (e)]. Measurements of the ASL (desert) are red and those of the CSL (forest) are blue. Circles show stable conditions, diamonds are used for near neutral stratification conditions, and crosses denote unstable conditions. The a_{33} shown in panel (c) are significantly larger in the CSL compared to the ASL at a confidence level of 95%. The black dashed line shows the expected value for isotropic turbulence and the solid blue line in panel (e) shows a linear regression of a_{33} for the CSL. The lower right panel (f) shows turbulent kinetic energy k normalized with u_* and the lower left panel (g) shows $\sigma_{u3}(\sigma_{u1}+\sigma_{u2})^{-1}$ together with the expectation for near neutral conditions as dashed lines [5]. Note the larger $\sigma_{u3}(\sigma_{u1}+\sigma_{u2})^{-1}$ for the CSL when compared to the ASL.

Moreover, these simulations do not have a "wall" thereby suppressing any possible wall-blocking likely to be higher in the ASL than the CSL. As earlier noted, the u_*^2 is larger for the CSL when compared to the ASL due to the rougher forest cover. While $\overline{u_3u_3}/u_*^2$ increases with increasing $-\zeta$, $\overline{u_1u_1}/u_*^2$ and $\overline{u_2u_2}/u_*^2$ vary with both $-\zeta$ and $\log_{10}(z/h_{BL})$, where h_{BL} is the boundary layer height as discussed elsewhere [16,17,53–55] with higher values (and fraction of k) in the ASL when compared to the CSL. Separate field experiments suggest that h_{BL} above the forest and the shrubland are comparable [56] (and by design, so are the z values in the CSL and ASL). These findings explain the lower measured k/u_*^2 in the CSL [Fig. 1(f)] when compared to its ASL counterpart given the larger u_* over the forest. While $\overline{u_1u_1}/u_*^2$, $\overline{u_2u_2}/u_*^2$, and $\overline{u_3u_3}/u_*^2$ follow expectations for near-neutral conditions from a mixing layer analogy [5] in the CSL, these flow statistics were higher than expected for the ASL (not shown). A plausible explanation for higher than expected values in the ASL are some topographic variability upwind of the ASL measurement tower. However, the aforementioned topographic variability did not affect the anisotropy appreciably given that canopy sublayer experiments (field and laboratory) collected at $z/h = 1$ yield $\sigma_{u3}(\sigma_{u1}+\sigma_{u2})^{-1} = 0.30$ (with

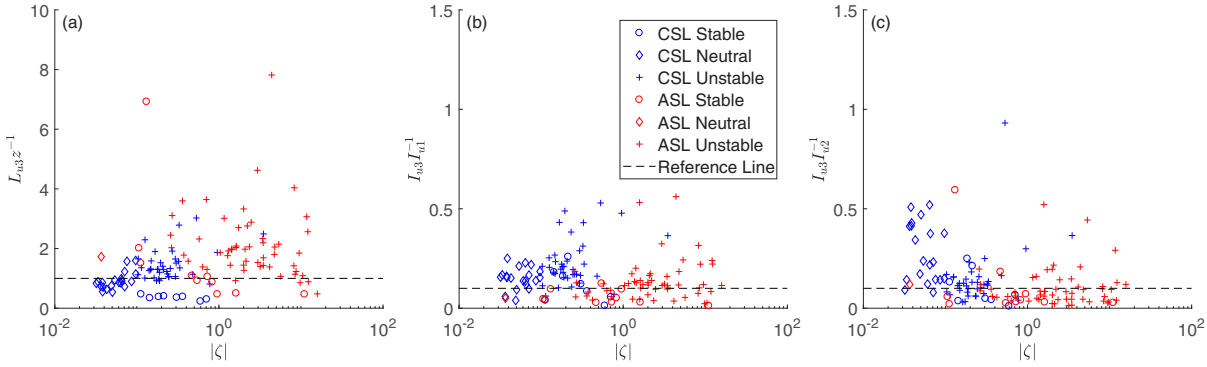

FIG. 2. Normalized length scale $L_{u3}z^{-1}$ (a) and the length scale ratios $L_{u3}L_{u1}^{-1}$ (b) and $L_{u3}L_{u2}^{-1}$ (c) are shown as a function of the absolute value of the stability parameter $|\zeta| = |(z-d)/L|$. Measurements of the ASL (desert) are red and those of the CSL (forest) are blue. Unstable stratification is shown as crosses, near neutral as diamonds, and stable as circles. The dashed line in panels (b) and (c) shows $L_{u3}L_{u1}^{-1} = 0.1$ reported from other experiments [57,58].

$\sigma_{ui} = \sqrt{\overline{u_i u_i}}$) whereas surface layer experiments yield $\sigma_{u3}(\sigma_{u1} + \sigma_{u2})^{-1} = 0.25$, to which ASL and CSL appear to be commensurate for near-neutral conditions [Fig. 1(g)].

To contrast energy anisotropy with eddy size anisotropy along the x_1, x_2, and x_3 directions, the effective eddy sizes for the u_i are determined from the integral time scale I_{ui} and Taylor's frozen turbulence hypothesis [42] using

$$L_{ui} = U I_{ui} = U \int_0^\infty \rho_{ui}(\tau_0) d\tau_0, \tag{28}$$

where $\rho_{ui}(\tau_0)$ is the u_i velocity component autocorrelation function and τ_0 is the time lag. Here, L_{u3} is presumed to be the most restrictive scale given that u_3 is the flow variable most impacted by the presence of a boundary (porous in the CSL and solid in the ASL). The calculations show that L_{u3}/z is on the order of unity for the CSL but higher in the ASL for near-neutral conditions [Fig. 2(a)]. As expected, L_{u3}/L_{u1} [Fig. 2(b)] and L_{u3}/L_{u2} [Fig. 2(c)] are well below unity for both ASL and CSL flows and do not vary appreciably with ζ. Roughly, L_{u1} is about a factor of 10 larger than L_{u3} (shown as a dashed line) in agreement with prior CSL [57] and ASL [58] experiments. Interestingly, the shape of the normalized energy distribution ellipsoid observed in Fig. 1 is qualitatively similar to the effective eddy sizes but they are not identical. Because L_{u3} is the most restrictive eddy size and partly captures some effects of ζ on elongation or compression of eddy sizes [Fig. 2(a)], the scalewise analysis is to be reported as r/L_{u3} (instead of r/z) for each run. It is also worth noting that r/L_{u3} may be interpreted as normalized time-scale separation given that Taylor's hypothesis equally impacts the numerator and denominator. While Taylor's hypothesis is not expected to be suitable near roughness elements [59] in the CSL, its distortions become less severe beyond $z/h > 2$, the case for the CSL here.

The ensemble-averaged (over ζ) normalized $D_{11}/\overline{2u_1u_1}$, $D_{22}/\overline{2u_2u_2}$, and $D_{33}/\overline{2u_3u_3}$ approaches unity at large rL_{u3}^{-1}, consistent with expectations from stationarity arguments (Fig. 3). However, stationarity appears to be attained at smaller rL_{u3}^{-1} for the CSL when compared to its ASL counterpart. The fact that $D_{11}/\overline{2u_1u_1}$ exhibits an approximate logarithmic region at scales larger than inertial but smaller than scales where $dD_{11}(r)/dr \approx 0$ is not surprising for the ASL, and is consistent with prior theoretical analysis explaining the -1 power law in the longitudinal velocity spectrum at large scales as well as in laboratory studies, field experiments, and large eddy simulations [55,60–68]. Such a logarithmic transition between inertial and $dD_{11}(r)/dr \approx 0$ is much more restricted in scale separation within the CSL.

At about $r/L_{u3} = 1/2$, all velocity component structure functions follow the $r^{2/3}$ K41 scaling, consistent with other ASL experiments [69,70]. However, second-order structure function scaling

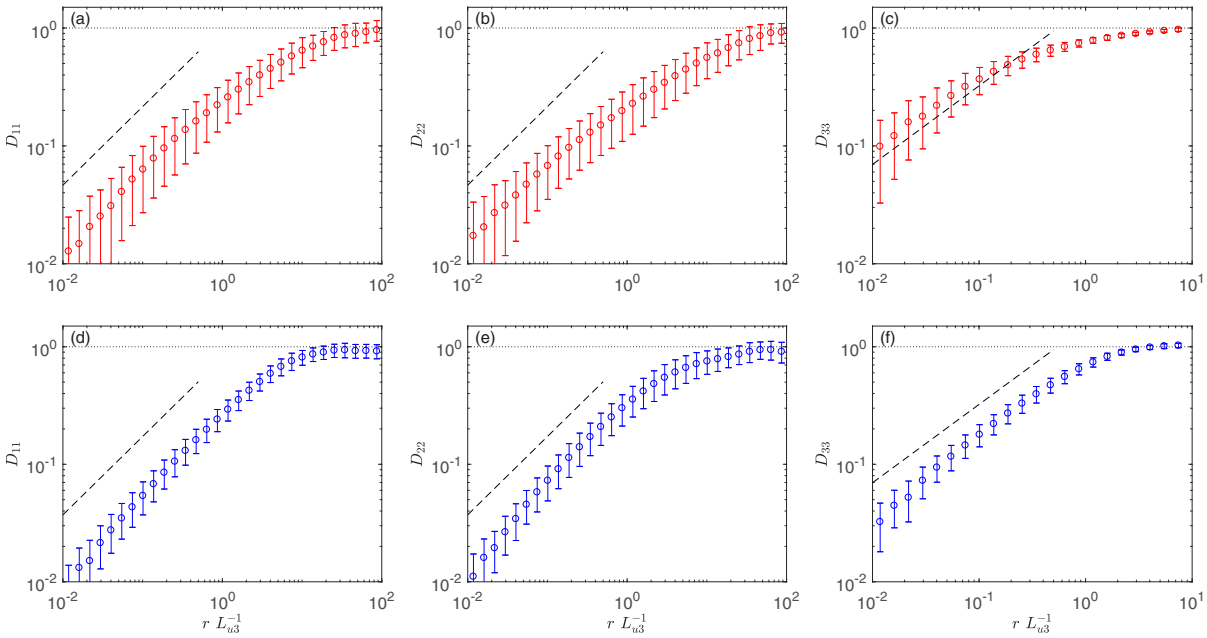

FIG. 3. Ensemble averaged of normalized structure function $\frac{1}{2}D_{11}\overline{u_1u_1}^{-1}$ (left column), $\frac{1}{2}D_{22}\overline{u_2u_2}^{-1}$ (middle column), and $\frac{1}{2}D_{33}\overline{u_3u_3}^{-1}$ (right column) are shown for the ASL (top, red) and CSL (bottom, blue). The black dotted line is $y = 1$ and the black dashed line shows the slope $r^{2/3}$ for Kolmogorov scaling [Eq. (18)]. The error bars show the standard deviation of the ensemble.

laws are only a necessary but not sufficient condition to the attainment of local isotropy. The componentwise velocity structure function ratios against r/L_{u3} demonstrate that anisotropy exists at fine scales even for $r/L_{u3} = 1/2$ and for both ASL and CSL flows (Fig. 4). However, for $r/L_{u3} < 0.1$, predictions from local isotropy agree with measurements. The calculations were repeated for D_{11}/D_{33} and D_{22}/D_{33} to correct for finite squared turbulent intensity effects using the linear model of Wyngaard and Clifford [43,71]. The results do not deviate appreciably from direct application of Taylor's frozen turbulence hypothesis, assuming small turbulent intensity (figure not shown). It is precisely the nature of this anisotropy that we seek to address using the invariance measures across scales.

B. Invariant analysis

The return-to-isotropy trajectories are shown in BAM for all ensemble members [Figs. 5(a) and 5(b)]. The starting and ending points of the scalewise trajectories are consistent with the conventional analysis previously discussed: large scales are further away from the isotropic (or 3D) limit for the ASL when compared to the CSL. The ζ variations also show no significant influence on the starting position of the points within the BAM [Figs. 5(a) and 5(b)].

The relaxation trajectories towards the isotropic (or 3D) state with decreasing scale r appear to be shorter for the CSL when compared to the ASL. Trajectories, by and large, show a return to isotropy by a contraction in the proximity of the 2D-3D limit for near-neutral and unstable ζ. However, the trajectory for stable conditions is closer to the center of the BAM [Figs. 5(c) and 5(d)]. In all cases, meandering of trajectories in the BAM with decreasing scale deviates from predictions based on zero-mean shear or homogeneous turbulence. These deviations partly reflect contributions from dU/dz that is active on all scales. In the AIM, the trajectories show rough similarities in curvature to the model for homogeneous turbulence [Eq. (24)] at the same starting position. This agreement is mainly due to the compressed trajectory representation of AIM near the isotropic limit corner, as discussed elsewhere [32]. The deviation between modeled and measured trajectories is quantified as the shortest distance in the BAM for a given r by $d(dI_2/dI_3, \vec{n}_{\mathrm{BAM}})$, with $\vec{n}_{\mathrm{BAM}} = (x_{\mathrm{BAM}}, y_{\mathrm{BAM}})$ given by Eq. (12) and dI_2/dI_3 by Eq. (24). The ensemble average of the deviation is decreasing

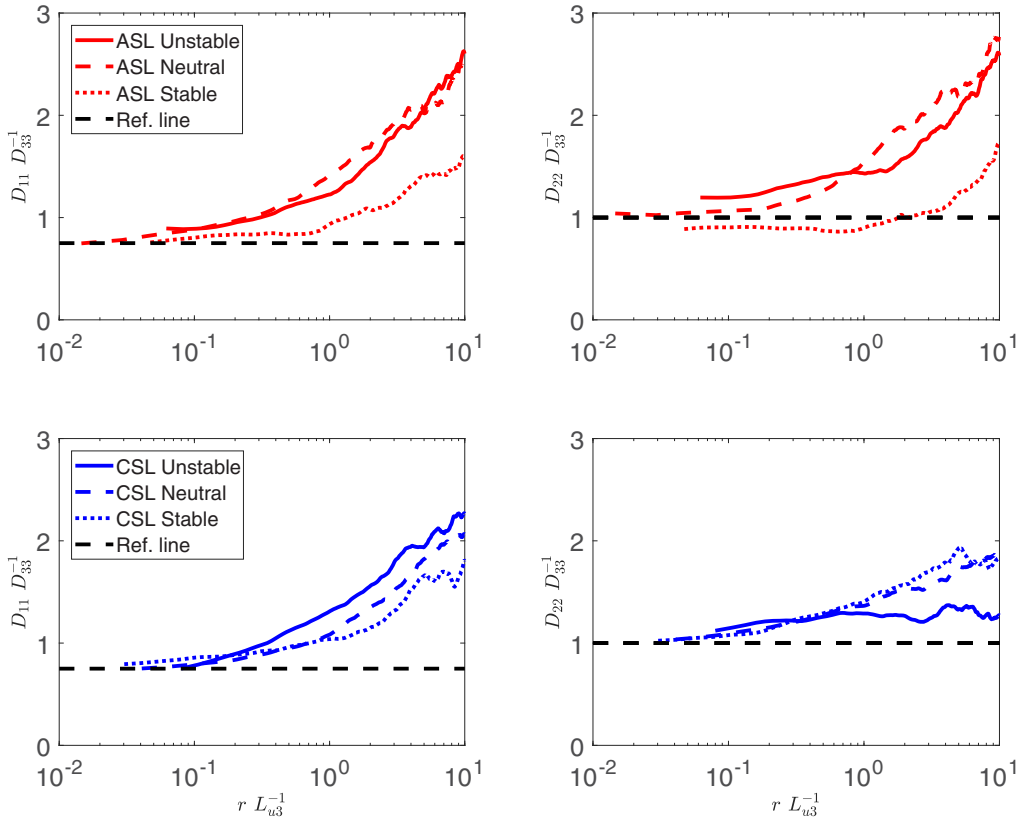

FIG. 4. Local isotropy attained by the ratios $D_{11}D_{33}^{-1}$ (left column) and $D_{22}D_{33}^{-1}$ (right column) for the ASL (top row, red) and CSL (bottom row, blue). The three lines show one example interval for stable (solid), neutral (dashed), and unstable (dotted) conditions. The black dashed line shows the expected ratio for locally isotropic turbulence based on K41.

towards the large scales, because we initialized the model with the measurements at the starting point of the trajectory, and at small scales where both converge to the isotropic state [Figs. 5(e) and 5(f)]. In between, the return to isotropy of the Rotta model shows significant deviations from the measurements, which cannot be explained by the measurement errors. The measurement errors were computed empirically by generating 2500 realizations of the anisotropy tensor a_{ij} from the accuracy of the covariance, assuming a normal distribution. Each a_{ij} was then diagonalized to gain a distribution of the eigenvalues and subsequently a distribution of $\vec{n}_{\mathrm{BAM}}$. From this the measurement error is estimated as the standard deviation of the distance between the mean of $\vec{n}_{\mathrm{BAM}}$ (which is equal to measurements) and each ensemble member.

An ensemble average of all runs shows at which rL_{u3}^{-1} the return to isotropy commences and terminates using both F and C_{iso} (Fig. 6). While the F (or AIM) measure suggests near-isotropic conditions at small scales, the C_{iso} (or BAM) measure suggests small but sustained anisotropy at those same small scales. As noted earlier, the AIM compresses the trajectories (and distance) near isotropic states, whereas BAM does not. Consistent with the previous structure function analysis, a near local isotropy at small scales $rL_{u3}^{-1} < 0.5$ is attained where as anisotropy exists at larger scales. The ASL is shown to be more anisotropic at large scales ($rL_{u3}^{-1} > 100$) when compared to the CSL. Both anisotropy measures reveal three separated regimes: scale independent anisotropy at large scales where F and C_{iso} are constantly low but approximately independent of scale (anisotropy is large), a return-to-isotropy regime in which the flow begins to relax towards isotropy as smaller scales are approached, and a third regime where scale-independent near-isotropy at small scales is attained (anisotropy is weak). The upper and lower scales bounding this intermediate regime are hereafter designated as r_{ani} and r_{iso}, respectively. They were determined from the scale r where C_{ani} has reached 90% of maximum isotropy (approaching from large r) in the case of r_{iso} and from the

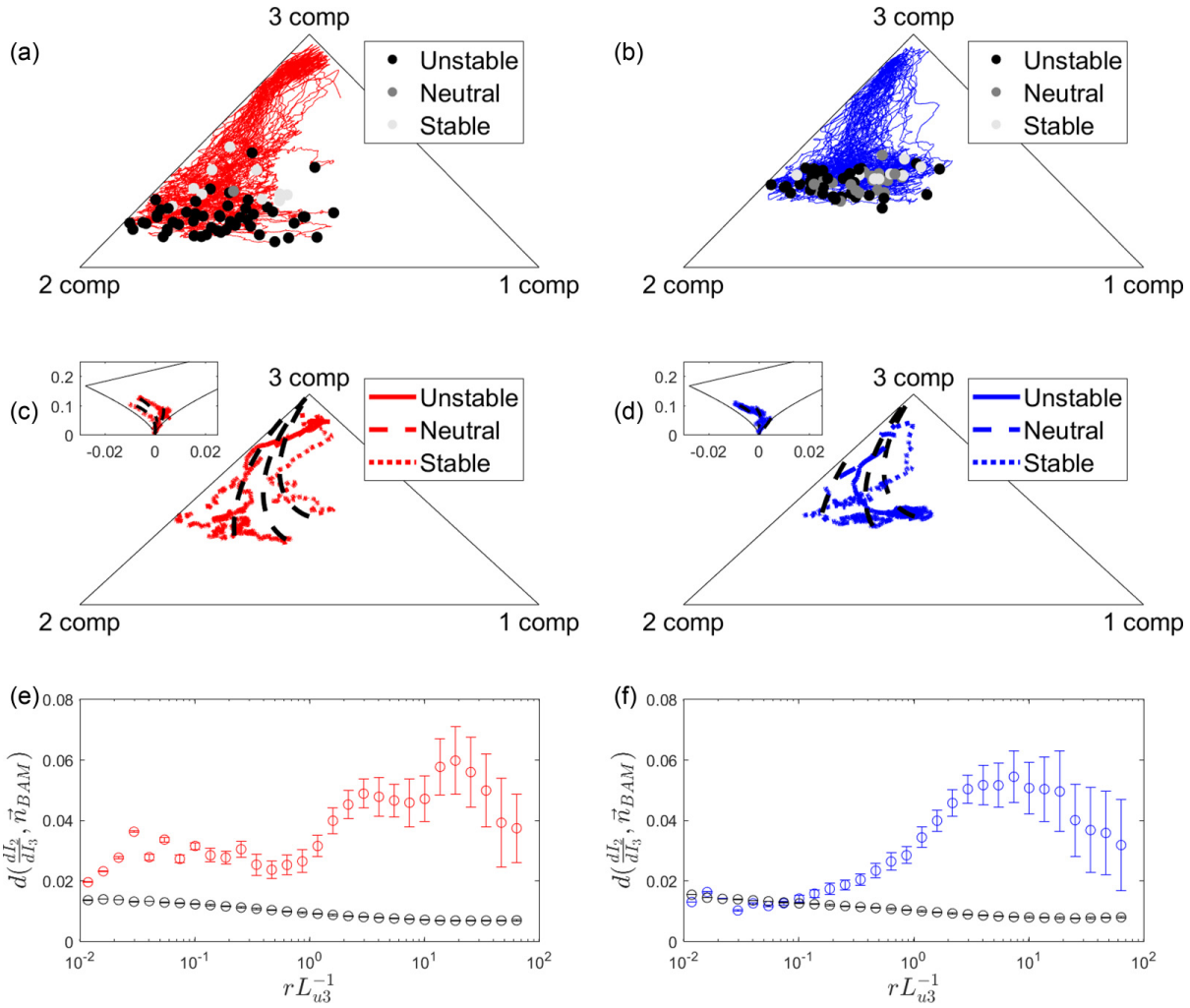

FIG. 5. The top row shows the trajectories of all 30 minute runs for the ASL (a) and the CSL (b) together with starting points color coded according to their stability class (black is unstable, dark grey is near neutral, and light grey is stable). The middle row shows return-to-isotropy trajectories in the BAM for three sample cases with unstable, neutral, and stable stratification of the ASL (c) and CSL (d) together with model trajectories [Eq. (24)]. The insets show the same three trajectories in the AIM representation. The bottom row shows the mean distance between modeled and measured trajectories in BAM, with the standard deviation as error bars, for the ASL (e) and CSL (f) together with the part of each deviation which can be explained by the measurement errors (black).

scale r where C_{ani} was within 10% of its lowest value (approaching from small r) in the case of r_{ani}. In the ASL, the return to isotropy is initiated at larger scales ($r_{\text{ani}} L_{u3}^{-1} > 70$) when compared to the CSL ($r_{\text{ani}} L_{u3}^{-1} > 25$) and covers a wider scale range. The scales at which local isotropy is roughly attained ($r_{\text{iso}} L_{u3}^{-1} = 0.5$) are comparable for the ASL and CSL.

The experiments above urban canopies suggested that r_{ani} varies with an outer length scale associated with the peak in the air temperature spectrum [26]. A similar analysis was conducted using the integral length scale of the air temperature time series L_{uT}, and the outcome is featured in Fig. 7. When analyzing all the individual runs, r_{ani} is smaller for stable than for unstable conditions for the CSL but not the ASL [Fig. 7(a)]. Also, r_{ani} has a weak dependency on L_{uT} for the ASL but not for the CSL [Fig. 7(a)]. In contrast, r_{iso} is less sensitive to variations in L_{uT} [Fig. 7(b)], especially in the ASL ($r_{\text{iso}} \approx z/2$). Normalizing r_{ani} and r_{iso} with L_{u3} removes any L_{uT} dependency in the ASL [Figs. 7(c) and 7(d)] and the correlation coefficient of L_{uT} and r_{ani} decreases from 0.43 to 0.02, and in case of r_{iso} it decreases from 0.40 to -0.12 (in the CSL all correlation coefficients are

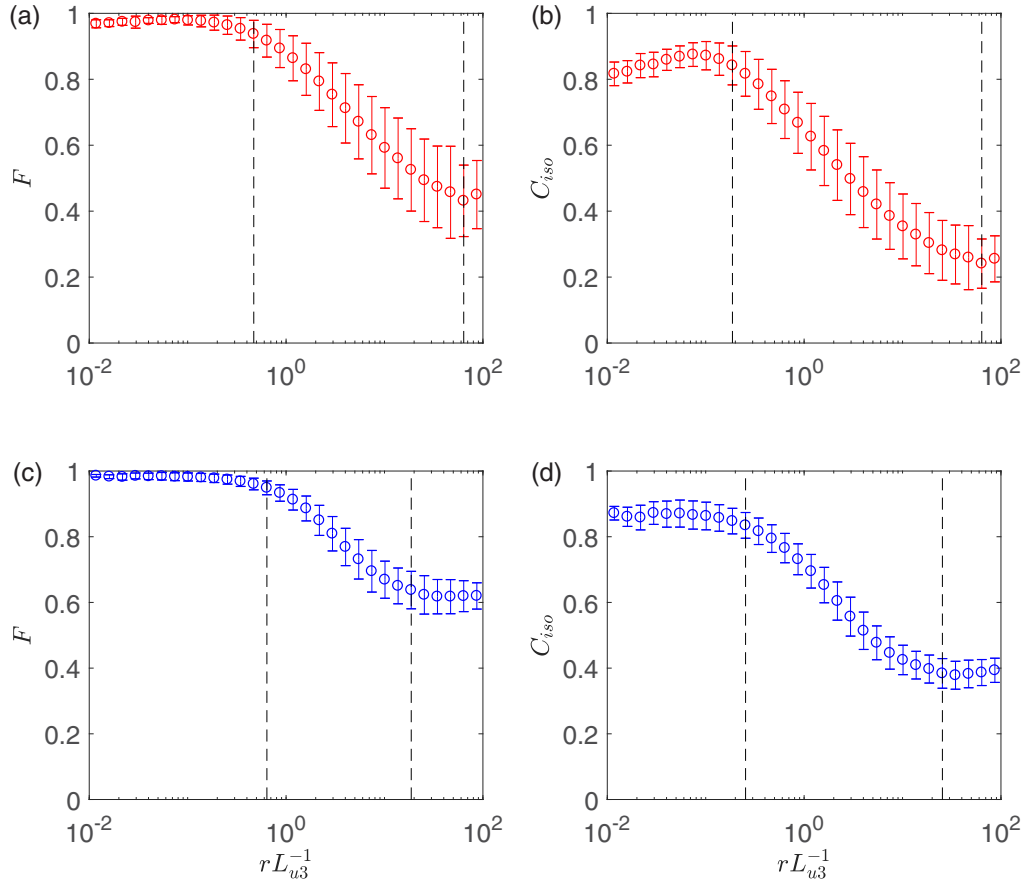

FIG. 6. Anisotropy measures F [left column, Eq. (14)] and C_{ani} [right column, Eq. (15)] are shown for ASL (top row, red) and CSL (bottom rom, blue) as an ensemble average with standard deviation across all ζ to highlight the role of surface roughness. The black dashed lines show three regimes defined by reaching 90% of maximum isotropy or 10% of anisotropy.

smaller than 0.14). That is, much of the dependency of r_{ani} on L_{uT} in the ASL can be attributed to variations in L_{u3} with $-\zeta$. Furthermore, ensemble averages of r_{ani} are significantly different for CSL and ASL and remain significantly different if normalized with L_{u3}. The ensemble average of r_{iso} is also significantly different when comparing CSL and ASL flows, but this difference is collapsed if r_{iso} is normalized L_{u3}. These results are robust even when other methods for determining r_{ani} and r_{iso} (e.g., fitting a tangent hyperbolic function) are employed (not shown). In comparison to experiments above urban canopies [26], values of L_{uT} cover similar ranges in the ASL and CSL. The range r_{ani} covers more than a decade if ASL and CSL results are treated separately (and when excluding the data point with $r_{\text{ani}} = 5$ for the CSL), which is a larger range than observed above urban canopies. It may be surmised that the return to isotropy depends more on roughness properties and less on surface heating or cooling for the same L.

The persistence of anisotropy at small scales has been extensively studied and linked to the finite mean velocity gradient [72,73]. The so-called integral structure function of order n, defined as

$$\overline{\left[\Delta u_k(r)^3 + \alpha_c r \frac{dU}{dz} \Delta u_k(r)^2\right]^{n/3}}, \tag{29}$$

has been shown to recover measured structure functions in laboratory settings and simulations [72,73] at small scales, where α_c is a similarity constant. The prevalence of dU/dz acting on all scales suggests that anisotropy produced by the mean velocity gradient can persist throughout the inertial subrange via finite cospectra [74,75]. This argument was recently suggested to explain persistent anisotropy in the urban surface layer [26]. In terms of a lower boundary condition on the flow, this mean velocity

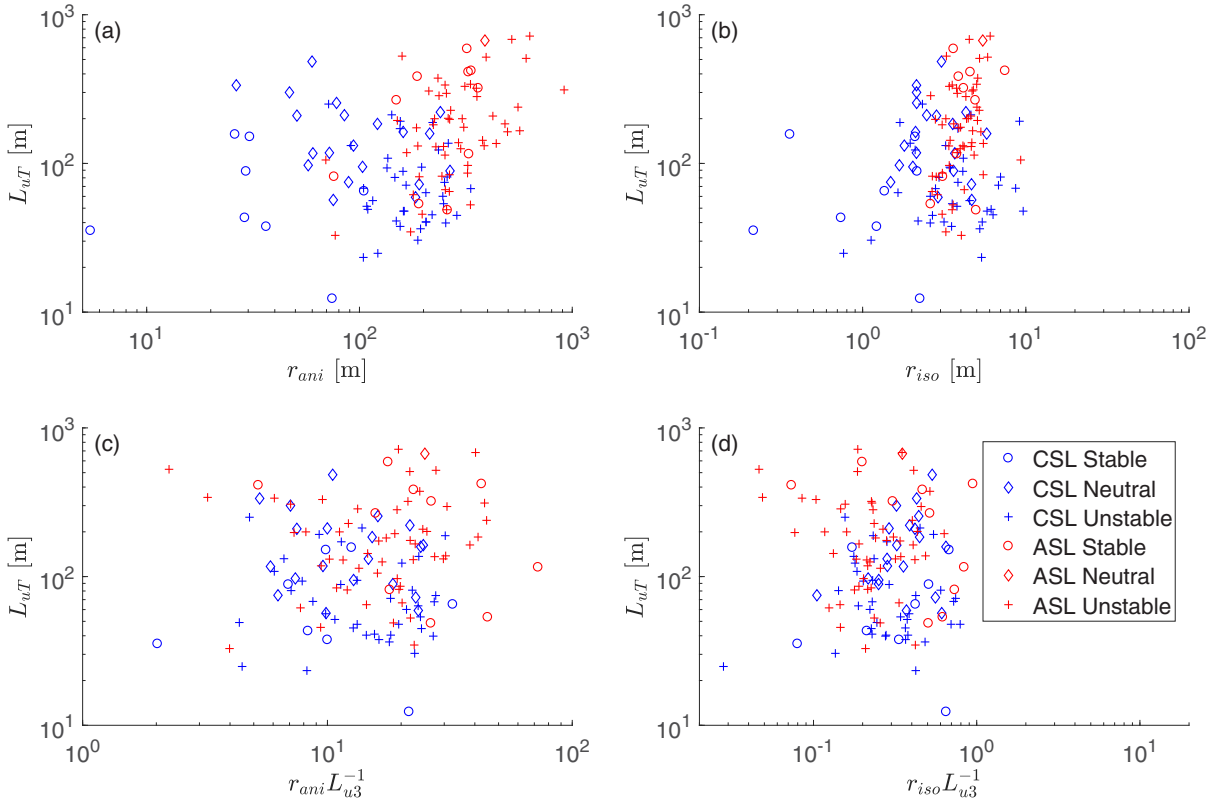

FIG. 7. The starting scales of the return to isotropy r_{ani} (a) and $r_{\text{ani}}L_{u3}^{-1}$ (c) and scales r_{iso} (b) and $r_{\text{iso}}L_{u3}^{-1}$ (d) at which isotropy is reached are plotted against the temperature length scale L_{uT}. Circles indicate stable, diamonds near-neutral, and crosses unstable stratification. Blue symbols show the CSL over the forest canopy and red symbols the ASL over the desert surface.

gradient is linked to the shear stress and thermal stratification by

$$\frac{dU}{dz} = \phi_m(\zeta)\frac{u_*}{\kappa z}. \tag{30}$$

For near-neutral conditions (i.e., $\phi_m(0) = 1$) and at a fixed z, increasing u_* increases dU/dz.

In the case of the CSL, u_* and dU/dz are expected to be higher than their ASL counterpart if κz is similar. However, the invariant analysis here suggests that ASL is more anisotropic at fine scales, $r < r_{\text{iso}}$. Hence, shear intensity (or dU/dz) alone cannot be the main cause. The alternative explanation stems from the fact that $\sigma_{u3}/(\sigma_{u1} + \sigma_{u2})$ is larger for the CSL when compared to its ASL counterpart for similar ζ values. While both ASL and CSL turbulence appear to be isotropic in the plane paralleling the ground surface, the CSL energy ellipsoid appears to be closer to 3D when compared to its ASL counterpart. This initial energy configuration state at large scales in the ASL requires that the return to isotropy transfer more energy to the vertical direction when compared to the CSL.

V. BROADER IMPACTS

The results presented here are pertinent to subgrid-scale turbulence closure schemes in large eddy simulations. Most models use subgrid-scale stress parametrization based on isotropic eddy-diffusivity schemes (e.g., PALM [76–78]). Turbulence closure methods accounting for subgrid-scale anisotropy based on explicit algebraic Reynolds stress models, which utilize the mean strain and rotation rate, have been developed and successfully tested [79,80]. Our results show that near isotropy can be attained for fine scales (<5 m) in CSL and ASL flows, but coarser grid resolutions require anisotropic subgrid modeling. Further, the results here can be utilized to improve or formulate new wall-blocking models, for example in the description of the mean velocity profile [81], as the data set spans

atmospheric flows from weak blockage (CSL) to strong blockage (ASL) and covers a wide range of velocity variances. The aforementioned examples above implicitly or explicitly assume Rotta's energy redistribution hypothesis, which is popular in higher-order closure schemes [82] used in climate and weather forecasting models (e.g., weather research and forecasting model). The analysis here hints of a need for exploring approaches beyond a linear Rotta scheme. Another path for improvement is to find a normalization collapsing r_{ani} between CSL and ASL, which then could be utilized in modeling the efficiency of the return to isotropy.

VI. CONCLUSIONS

Scalewise invariant analysis showed that the return to isotropy is initiated at larger scales and covers a wider range of scales in the ASL when compared to the CSL. This statement holds when scales (or separation distances) are normalized by the integral length of the vertical velocity. The two normalized scales at which the return to isotropy becomes active and near isotropy is attained are insensitive to atmospheric thermal stratification (again when the scales are normalized by the integral length scale of the vertical velocity). However, the precise trajectory in the BAM towards isotropy at finer scales is modified by thermal stratification and mean velocity gradient, and does not follow expectation from homogeneous turbulence. The analysis also reveals that larger scales appear less anisotropic in the CSL when compared to its ASL counterpart. Both CSL and ASL appear to be near-planar isotropic at large scales. However, the reduced overall anisotropy in the CSL mainly originates from $\sigma_{u3}/(\sigma_{u1} + \sigma_{u2})$ being larger for CSL when compared to its ASL counterpart. Hence, CSL turbulence commences its relaxation to isotropy in BAM with reduced scales from a point closer to the 3D state and along the 2D-3D interface. Because of the significance of the third invariant (in both ASL and CSL), the classical Rotta return-to-isotropy approach must be amended. The work here also shows that the return to isotropy depends more on surface roughness properties and less on surface heating. From a broader perspective, the work here extends prior laboratory (pipe and wind-tunnel) studies by demonstrating that rougher surfaces (i.e., a forest) tend to make turbulence more isotropic than their smooth wall or small roughness (i.e., shrubland) counterparts.

ACKNOWLEDGMENTS

G.K. acknowledges support from the National Science Foundation (NSF-EAR-1344703, NSF-AGS-1644382, and NSF-DGE-1068871) and from the Department of Energy (DE-SC0011461). K.K. and P.B. acknowledge support from the German Research Foundation (DFG) as part of the project "Climate feedbacks and benefits of semi-arid forests" (CliFF) (SCHM 2736/2-1). M.M. and F.D.R. acknowledge support from the Helmholtz-Association through the President's Initiative and Networking Fund as part of the Young Investigator Group "Capturing all relevant scales of biosphere-atmosphere exchange—the enigmatic energy balance closure problem" (VH-NG-843). This work was supported by a Helmholtz Research School MICMoR Visiting Scientist Fellowship through KIT/IMK-IFU to G.K. (HGF VH-KO-505).

[1] A. S. Monin and A. M. F. Obukhov, Basic laws of turbulent mixing in the surface layer of the atmosphere, Contrib. Geophys. Inst. Acad. Sci. USSR **24**, 163 (1954) [**151**, e187 (1954)].

[2] A. J. Dyer, A review of flux-profile relationships, Bound.-Lay. Meteorol. **7**, 363 (1974).

[3] J. R. Garratt, Surface influence upon vertical profiles in the atmospheric near-surface layer, Q. J. R. Meteorol. Soc. **106**, 803 (1980).

[4] M. R. Raupach and A. S. Thom, Turbulence in and above plant canopies, Annu. Rev. Fluid Mech. **13**, 97 (1981).

[5] M. R. Raupach, J. J. Finnigan, and Y. Brunet, Coherent eddies and turbulence in vegetation canopies: The mixing-layer analogy, Bound.-Lay. Meteorol. **25**, 351 (1996).

[6] J. J. Finnigan, Turbulence in plant canopies, Annu. Rev. Fluid Mech. **32**, 519 (2000).
[7] T. Foken, 50 years of the Monin–Obukhov similarity theory, Bound.-Lay. Meteorol. **119**, 431 (2006).
[8] I. N. Harman and J. J. Finnigan, A simple unified theory for flow in the canopy and roughness sublayer, Bound.-Lay. Meteorol. **123**, 339 (2007).
[9] G. G. Katul, A. G. Konings, and A. Porporato, Mean Velocity Profile in a Sheared and Thermally Stratified Atmospheric Boundary Layer, Phys. Rev. Lett. **107**, 268502 (2011).
[10] J. C. Wyngaard and O. R. Coté, The budgets of turbulent kinetic energy and temperature variance in the atmospheric surface layer, J. Atmos. Sci. **28**, 190 (1971).
[11] H. A. Panofsky and J. A. Dutton, *Atmospheric Turbulence: Models and Methods for Engineering Applications* (Wiley, New York, 1984).
[12] B. A. Kader and A. M. Yaglom, Mean fields and fluctuation moments in unstably stratified turbulent boundary layers, J. Fluid Mech. **212**, 637 (1990).
[13] J. R. Garratt *et al.*, *The Atmospheric Boundary Layer*, Cambridge Atmospheric and Space Science Series, Vol. 416 (Cambridge University Press, Cambridge, 1994).
[14] J. C. Kaimal and J. J. Finnigan, *Atmospheric Boundary Layer Flows: Their Structure and Measurement* (Oxford University Press, Oxford, 1994).
[15] J. J. Finnigan, R. H. Shaw, and E. G. Patton, Turbulence structure above a vegetation canopy, J. Fluid Mech. **637**, 387 (2009).
[16] T. Banerjee and G. G. Katul, Logarithmic scaling in the longitudinal velocity variance explained by a spectral budget, Phys. Fluids **25**, 125106 (2013).
[17] T. Banerjee, G. G. Katul, S. T. Salesky, and M. Chamecki, Revisiting the formulations for the longitudinal velocity variance in the unstable atmospheric surface layer, Q. J. R. Meteorol. Soc. **141**, 1699 (2015).
[18] T. Banerjee, D. Li, J.-Y. Juang, and G. G. Katul, A spectral budget model for the longitudinal turbulent velocity in the stable atmospheric surface layer, J. Atmos. Sci. **73**, 145 (2016).
[19] E. G. Patton, P. P. Sullivan, R. H. Shaw, J. J. Finnigan, and J. C. Weil, Atmospheric stability influences on coupled boundary layer and canopy turbulence, J. Atmos. Sci. **73**, 1621 (2016).
[20] R. A. Antonia, J. Kim, and L. W. B. Browne, Some characteristics of small-scale turbulence in a turbulent duct flow, J. Fluid Mech. **233**, 369 (1991).
[21] H. S. Shafi and R. A. Antonia, Anisotropy of the Reynolds stresses in a turbulent boundary layer on a rough wall, Exp. Fluids **18**, 213 (1995).
[22] K. S. Choi and J. L. Lumley, The return to isotropy of homogeneous turbulence, J. Fluid Mech. **436**, 59 (2001).
[23] P.-Å. Krogstad and L. E. Torbergsen, Invariant analysis of turbulent pipe flow, Flow, Turbul. Combust. **64**, 161 (2000).
[24] R. A. Antonia and P.-Å. Krogstad, Turbulence structure in boundary layers over different types of surface roughness, Fluid Dyn. Res. **28**, 139 (2001).
[25] R. Smalley, S. Leonardi, R. Antonia, L. Djenidi, and P. Orlandi, Reynolds stress anisotropy of turbulent rough wall layers, Exp. Fluids **33**, 31 (2002).
[26] H. Liu, R. Yuan, J. Mei, J. Sun, Q. Liu, and Y. Wang, Scale properties of anisotropic and isotropic turbulence in the urban surface layer, Bound.-Lay. Meteorol. **165**, 277 (2017).
[27] S. Sarkar and C. G. Speziale, A simple nonlinear model for the return to isotropy in turbulence, Phys. Fluids A **2**, 84 (1990).
[28] P. K. Yeung and James G. Brasseur, The response of isotropic turbulence to isotropic and anisotropic forcing at the large scales, Phys. Fluids A **3**, 884 (1991).
[29] T. Jongen and T. B. Gatski, General explicit algebraic stress relations and best approximation for three-dimensional flows, Int. J. Eng. Sci. **36**, 739 (1998).
[30] F. G. Schmitt, Direct test of a nonlinear constitutive equation for simple turbulent shear flows using DNS data, Commun. Nonlinear Sci. Numer. Simul. **12**, 1251 (2007).
[31] J. P. Panda, H. V. Warrior, S. Maity, A. Mitra, and K. Sasmal, An improved model including length scale anisotropy for the pressure strain correlation of turbulence, J. Fluids Eng. **139**, 044503 (2017).
[32] S. Banerjee, R. Krahl, F. Durst, and C. Zenger, Presentation of anisotropy properties of turbulence, invariants versus eigenvalue approaches, J. Turbul., doi: 10.1080/14685240701506896.

[33] J. L. Lumley and G. R. Newman, The return to isotropy of homogeneous turbulence, J. Fluid Mech. **82**, 161 (1977).
[34] J. L. Lumley, Computational modeling of turbulent flows, Adv. Appl. Mech. **18**, 213 (1979).
[35] T.-H. Shih, J. Zhu, and J. L. Lumley, A new Reynolds stress algebraic equation model, Comput. Methods Appl. Mech. Eng. **125**, 287 (1995).
[36] D. B. Taulbee, An improved algebraic Reynolds stress model and corresponding nonlinear stress model, Phys. Fluids A **4**, 2555 (1992).
[37] T. Rung, F. Thiele, and S. Fu, On the realizability of nonlinear stress–strain relationships for Reynolds stress closures, Flow Turbul. Combust. **60**, 333 (1998).
[38] U. Schumann, Realizability of Reynolds-stress turbulence models, Phys. Fluids **20**, 721 (1977).
[39] D. Poggi, A. Porporato, L. Ridolfi, J. D. Albertson, and G. G. Katul, The effect of vegetation density on canopy sub-layer turbulence, Bound.-Lay. Meteorol. **111**, 565 (2004).
[40] J. M. Chacin and B. J. Cantwell, Dynamics of a low Reynolds number turbulent boundary layer, J. Fluid Mech. **404**, 87 (2000).
[41] S. B. Pope, A more general effective-viscosity hypothesis, J. Fluid Mech. **72**, 331 (1975).
[42] G. I. Taylor, The spectrum of turbulence, Proc. R. Soc. London A **164**, 476 (1938).
[43] C.-I. Hsieh and G. G. Katul, Dissipation methods, taylor's hypothesis, and stability correction functions in the atmospheric surface layer, J. Geophys. Res. **102**, 16391 (1997).
[44] E. Rotenberg and D. Yakir, Distinct patterns of changes in surface energy budget associated with forestation in the semiarid region, Glob. Change Biol. **17**, 1536 (2011).
[45] F. Eder, F. De Roo, E. Rotenberg, D. Yakir, H. P. Schmid, and M. Mauder, Secondary circulations at a solitary forest surrounded by semi-arid shrubland and their impact on eddy-covariance measurements, Agric. For. Meteorol. **211**, 115 (2015).
[46] A. M. Obukhov, The local structure of atmospheric turbulence, Dokl. Akad. Nauk. SSSR **67**, 643 (1949).
[47] U. Högström and A.-S. Smedman, Accuracy of sonic anemometers: laminar wind-tunnel calibrations compared to atmospheric in situ calibrations against a reference instrument, Bound.-Lay. Meteorol. **111**, 33 (2004).
[48] R. G. Barry and R. J. Chorley, *Atmosphere, Weather and Climate*, 8th ed. (Routledge, New York, 2003).
[49] U. Dayan and J. Rodnizki, The temporal behavior of the atmospheric boundary layer in Israel, J. Appl. Meteorol. **38**, 830 (1999).
[50] T. Foken and B. Wichura, Tools for quality assessment of surface-based flux measurements, Agric. For. Meteorol. **78**, 83 (1996).
[51] M. Mauder, M. Cuntz, C. Drüe, A. Graf, C. Rebmann, H. P. Schmid, M. Schmidt, and R. Steinbrecher, A strategy for quality and uncertainty assessment of long-term eddy-covariance measurements, Agric. For. Meteorol. **169**, 122 (2013).
[52] J. C. Isaza and L. R. Collins, On the asymptotic behaviour of large-scale turbulence in homogeneous shear flow, J. Fluid Mech. **637**, 213 (2009).
[53] I. Marusic, J. P. Monty, M. Hultmark, and A. J. Smits, On the logarithmic region in wall turbulence, J. Fluid Mech. **716**, R3 (2013).
[54] C. Meneveau and I. Marusic, Generalized logarithmic law for high-order moments in turbulent boundary layers, J. Fluid Mech. **719**, R1-1 (2013).
[55] R. J. A. M. Stevens, M. Wilczek, and C. Meneveau, Large-eddy simulation study of the logarithmic law for second-and higher-order moments in turbulent wall-bounded flow, J. Fluid Mech. **757**, 888 (2014).
[56] T. Banerjee, P. Brugger, F. De Roo, K. Kröniger, D. Yakir, E. Rotenberg, and M. Mauder, Turbulent transport of energy across a forest and a semi-arid shrubland, Atmos. Chem. Phys. Discuss., doi: 10.5194/acp-2017-159.
[57] G. G. Katul and W.-H. Chang, Principal length scales in second-order closure models for canopy turbulence, J. Appl. Meteorol. **38**, 1631 (1999).
[58] B. A. Kader, A. M. Yaglom, and S. L. Zubkovskii, Spatial correlation functions of surface-layer atmospheric turbulence in neutral stratification, Bound.-Lay. Meteorol. **47**, 233 (1989).

[59] Y. Pan and M. Chamecki, A scaling law for the shear-production range of second-order structure functions, J. Fluid Mech. **801**, 459 (2016).
[60] P. Drobinski, P. Carlotti, R. K. Newsom, R. M. Banta, R. C. Foster, and J.-L. Redelsperger, The structure of the near-neutral atmospheric surface layer, J. Atmos. Sci. **61**, 699 (2004).
[61] P. A. Davidson, T. B. Nickels, and P.-Å. Krogstad, The logarithmic structure function law in wall-layer turbulence, J. Fluid Mech. **550**, 51 (2006).
[62] P. A. Davidson and P.-Å. Krogstad, A simple model for the streamwise fluctuations in the log-law region of a boundary layer, Phys. Fluids **21**, 055105 (2009).
[63] G. G. Katul, A. Porporato, and V. Nikora, Existence of k^{-1} power-law scaling in the equilibrium regions of wall-bounded turbulence explained by Heisenberg's eddy viscosity, Phys. Rev. E **86**, 066311 (2012).
[64] G. G. Katul, T. Banerjee, D. Cava, M. Germano, and A. Porporato, Generalized logarithmic scaling for high-order moments of the longitudinal velocity component explained by the random sweeping decorrelation hypothesis, Phys. Fluids **28**, 095104 (2016).
[65] P. A. Davidson and P.-Å. Krogstad, A universal scaling for low-order structure functions in the log-law region of smooth-and rough-wall boundary layers, J. Fluid Mech. **752**, 140 (2014).
[66] C. M. de Silva, I. Marusic, J. D. Woodcock, and C. Meneveau, Scaling of second-and higher-order structure functions in turbulent boundary layers, J. Fluid Mech. **769**, 654 (2015).
[67] R. A. Antonia and M. R. Raupach, Spectral scaling in a high Reynolds number laboratory boundary layer, Bound.-Lay. Meteorol. **65**, 289 (1993).
[68] Marcelo Chamecki, Nelson L. Dias, Scott T. Salesky, and Ying Pan, Scaling laws for the longitudinal structure function in the atmospheric surface layer, J. Atmos. Sci. **74**, 1127 (2017).
[69] J. C. Kaimal, J. C. Wyngaard, Y. Izumi, and O. R. Coté, Spectral characteristics of surface-layer turbulence, Q. J. R. Meteorol. Soc. **98**, 563 (1972).
[70] G. G. Katul, C.-I. Hsieh, and J. Sigmon, Energy-inertial scale interactions for velocity and temperature in the unstable atmospheric surface layer, Bound.-Lay. Meteorol. **82**, 49 (1997).
[71] J. C. Wyngaard and S. F. Clifford, Taylor's hypothesis and high-frequency turbulence spectra, J. Atmos. Sci. **34**, 922 (1977).
[72] F. Toschi, E. Leveque, and G. Ruiz-Chavarria, Shear Effects in Nonhomogeneous Turbulence, Phys. Rev. Lett. **85**, 1436 (2000).
[73] D. Poggi, A. Porporato, and L. Ridolfi, Analysis of the small-scale structure of turbulence on smooth and rough walls, Phys. Fluids **15**, 35 (2003).
[74] G. G. Katul, A. Porporato, C. Manes, and C. Meneveau, Co-spectrum and mean velocity in turbulent boundary layers, Phys. Fluids **25**, 091702 (2013).
[75] T. Ishihara, K. Yoshida, and Y. Kaneda, Anisotropic Velocity Correlation Spectrum at Small Scales in a Homogeneous Turbulent Shear Flow, Phys. Rev. Lett. **88**, 154501 (2002).
[76] J. W. Deardorff, Stratocumulus-capped mixed layers derived from a three-dimensional model, Bound.-Lay. Meteorol. **18**, 495 (1980).
[77] C.-H. Moeng and J. C. Wyngaard, Spectral analysis of large-eddy simulations of the convective boundary layer, J. Atmos. Sci. **45**, 3573 (1988).
[78] B. Maronga, M. Gryschka, R. Heinze, F. Hoffmann, F. Kanani-Sühring, M. Keck, K. Ketelsen, M. O. Letzel, M. Sühring, and S. Raasch, The parallelized large-eddy simulation model (PALM) version 4.0 for atmospheric and oceanic flows: Model formulation, recent developments, and future perspectives, Geosci. Model Dev. **8**, 2515 (2015).
[79] T. B. Gatski and C. G. Speziale, On explicit algebraic stress models for complex turbulent flows, J. Fluid Mech. **254**, 59 (1993).
[80] L. Marstorp, G. Brethouwer, O. Grundestam, and A. V. Johansson, Explicit algebraic subgrid stress models with application to rotating channel flow, J. Fluid Mech. **639**, 403 (2009).
[81] K. A. McColl, G. G. Katul, P. Gentine, and D. Entekhabi, Mean-velocity profile of smooth channel flow explained by a cospectral budget model with wall-blockage, Phys. Fluids **28**, 035107 (2016).
[82] G. L. Mellor and T. Yamada, Development of a turbulence closure model for geophysical fluid problems, Rev. Geophys. **20**, 851 (1982).

Diurnal variability of the turbulent transport properties above a semi-arid forest canopy in contrast to a nearby shrubland

Peter Brugger[a,*], Frederik De Roo[a], Konstantin Kröniger[a], Eyal Rotenberg[b], Dan Yakir[b], Matthias Zeeman[a], Matthias Mauder[a]

[a] *Institute of Meteorology and Climate Research - Atmospheric Environmental Research, Kreuzeckbahnstraße 19, 82467 Garmisch-Partenkirchen, Germany*
[b] *Weizmann Institute of Science, Faculty of Chemistry, Department of Earth and Planetary Sciences, 234 Herzl Street, Rehovot 7610001, Israel*

Abstract

Efficiency and energetics of the turbulent transport in the canopy sublayer of a semi-arid pine forest and the atmospheric surface layer of a sparse desert-like shrubland are investigated from ultrasonic anemometer measurements during the summer dry season. The results show that an increased sensible heat flux over the forest canopy is generated by more energetic turbulence across all scales, but the transport process itself is equally efficient compared to the neighbouring shrubland. In contrast, the turbulent momentum flux over the forest canopy is caused by more efficient and energetic momentum transport at large scales. The more energetic turbulence appears to reduce the aerodynamic resistance to heat transfer of the semi-arid forest, which enables the increased sensible heat flux at a lower surface temperature. The results help explain the observed differences in diurnal variation of statistical moments of turbulent quantities that are caused by the interaction between radiative forcing, the background wind and the different turbulence production regimes of the forest and the shrubland. Lastly, the results also explain the observed cooler nighttime temperatures and quicker formation of a residual layer at the forest site.

Keywords: Surface-atmosphere exchange, Semi-arid forest, Sea-breeze,

*Corresponding author
Email address: peter.brugger@kit.edu (Peter Brugger)

Turbulent transport, Phase difference, Diurnal cycle

1. Introduction

Forests in semi-arid regions influence the Earth's climate through modifying CO_2 and net radiation (Rotenberg and Yakir, 2010). Cooling effects by carbon sequestration and increased cloud cover are contrasted by warming effects due to higher net radiation and humidity (Betts, 2000; Rotenberg and Yakir, 2011), resulting in a loss of of efficiency for the forest productivity that corresponds to decades of carbon uptake (Rotenberg and Yakir, 2010). The significance of these semi-arid ecosystems could increase in the future due to predicted warming and drying trends for parts of the global land area (Burke et al., 2006) and due to afforestation efforts in the eastern Mediterranean (Sprintsin et al., 2009). However, these semi-arid forests are confronted with a large net radiation, due to high amounts of incoming radiation and a low albedo, while evaporative cooling is limited by low water availability during the summer dry season. Their survival relies on a canopy convector effect, which generates a turbulent transport of heat to the overlying atmosphere, while maintaining a low surface (skin) temperature (Rotenberg and Yakir, 2011). Therefore, a detailed investigation of the underlying physical processes and environmental conditions, that contribute to the canopy convector effect is important for understanding and modeling these dry ecosystems.

The turbulent exchange within the canopy sublayer has been conceptualized as a dominant eddy structure of two linked hairpin-vortices (Finnigan et al., 2009), which facilitates a more efficient transport of momentum and scalars, supported by weaker mean gradients compared to the atmospheric surface layer (Raupach, 1979; Raupach et al., 1996). Furthermore, the canopy sublayer is characterised by an inflection point in mean velocity profiles at the canopy top (h_c) , a decay of second order moments within the canopy towards the surface, and larger streamwise and vertical skewnesses, compared to the surface layer, up to a height of $2h_c$ (Katul et al., 2013). Modeling the relevant processes of

these surface-atmosphere interactions for a semi-arid forest canopy is important for predicting the impact of such ecosystems on the regional and global climate. Models with fine grid resolutions can resolve a forest canopy (e.g. large-eddy simulations), but coarser meso-scale models need to rely on parametrizations of these effects with aerodynamic resistance approaches. In case of the kinematic sensible heat flux this approach is given by

$$\overline{w'T'} = \frac{\overline{T}_s - \overline{T}_a}{r_H}, \tag{1}$$

where bars indicate averages and primes turbulent fluctuations , $\overline{T}_s - \overline{T}_a$ is the difference between surface and air temperature, and r_H the aerodynamic resistance to heat transfer. In the frame of this work temporal averages are used assuming ergodicity.

Previous research on the canopy convector effect with large-eddy simulations showed a decrease of the aerodynamic resistance with more unstable stratification for a homogeneous forest canopy (Banerjee et al., 2017). Studies of the isolated Yatir forest in Israel, an example of such a semi-arid ecosystem (detailed description in section 2.1), showed the influence of secondary circulations due to the differences in the net radiation between the Yatir forest and the surrounding desert-like shrubland (Eder et al., 2015; Kröniger et al., 2018). However, these studies have not investigated the underlying micrometeorlogical processes or the influence of the diurnal patterns, which includes a daily recurring sea-breeze during the summer dry season.

Therefore, this article aims to answer the following research questions: (1) What are the important turbulent transport properties for heat and momentum in terms of efficiency and magnitude across scales at the Yatir forest in comparison to its surrounding shrubland? (2) How does the presence of a diurnal cycle and sea-breeze affect the surface-atmosphere exchange at the Yatir forest? This improved understanding will help to identify the important aspects of surface-atmosphere interactions of semi-arid forests that need to be accounted for in modeling.

2. Methods

In the following subsections the research site, the measurement instruments and data processing steps used to obtain the results are described.

2.1. Research site and measurement setup

The study area is the Yatir forest and its surrounding desert-like shrubland (Fig. 1) located in central Israel with an annual mean precipitation of 285 mm and a global radiation of 238 W m^{-2} (Rotenberg and Yakir, 2010). The Yatir forest is an isolated, artificially planted pine forest at the dry timberline with *Pinus halepensis* as the dominant tree species. The surrounding shrubland consists of bare soil with scattered herbaceous annual and perennial species (mainly *Sarcopoterium spinosum* with heights of $0.3-0.5$ m). The distinct differences of albedo and roughness between the two vegetation types lead to a larger sensible heat flux and net radiation at the forest compared to the shrubland (Rotenberg and Yakir, 2011; Eder et al., 2015) and a modified turbulence structure near the surface (Brugger et al., 2018). Our measurement setup featured two measurement sites, one at the oldest part of the forest (latitude 31.3757°, longitude 35.0522°, and 660 m above sea level) and one upwind of the forest in the shrubland (latitude 31.3453°, longitude 35.0242°, and 620 m above sea level), each equipped with an ultrasonic anemometer and a Doppler wind lidar. The measurements were conducted in the second half of August 2015 during the summer dry season, when the synoptic scales are controlled by the subtropical ridge leading to cloud-free and stationary weather conditions with a radiation driven diurnal cycle of the atmospheric boundary layer.

2.2. Ultrasonic anemometer measurements and data processing

Ultrasonic anemometers were used to measure the sonic temperature (T) and the three components of the wind vector (u, v and w) from travel times of sound waves along the three transducer axes at a frequency of 20 Hz. The ultrasonic anemometer at the forest site (R3-50 from Gill Instruments, Lymington, Hampshire, UK) was mounted 19 m above the ground (mean tree height at the

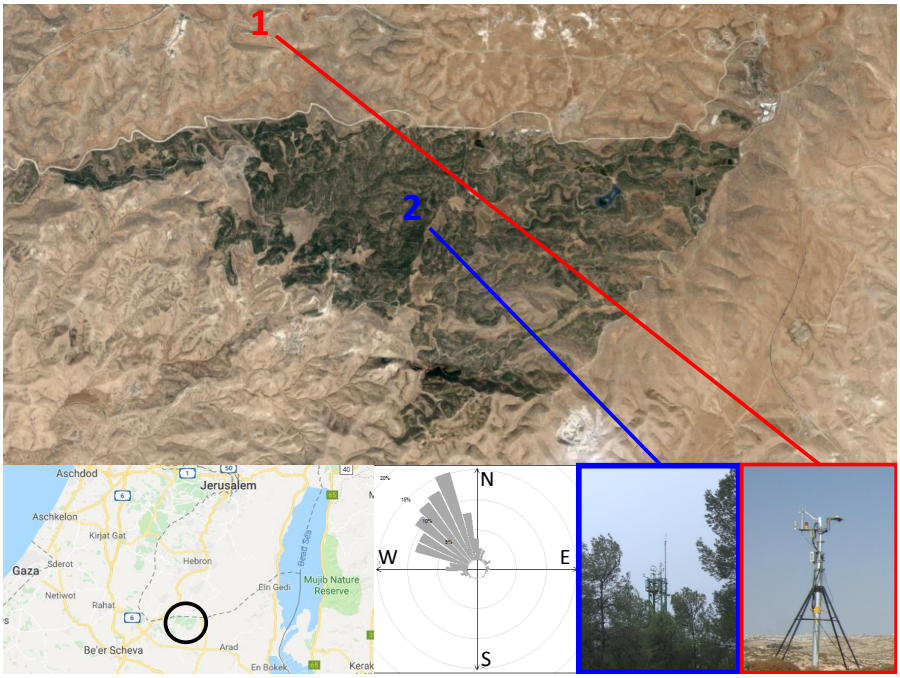

Figure 1: Top: Satellite image of Yatir forest in Israel at the northern edge of the Negev desert with the location of the shrubland site (1, red) and forest site (2, blue). Bottom left to right: Map of the area between Dead Sea and Mediterranean Sea with the location of Yatir forest indicated with a black circle, frequency-of-occurrence wind-rose of the 300 m a.g.l. wind speed from Doppler lidar measurements at the forest site, and photos of the two eddy-covariance stations. Source of satellite image and map: Google.

site is 10 m, placing it 9 m above the canopy). The instrument at the shrubland site (R3-100 from Gill Instruments, Lymington, Hampshire, UK) was mounted 9 m above the ground until 23 August 2015, when it was raised to 15 m to increase the flux footprint.

The first step in post-processing of the raw data was to apply a quality control scheme and to compute turbulence statistics at 30-min intervals. This was done with the TK3 software (Mauder and Foken, 2015), which includes despiking (Mauder et al., 2013), unit conversions (Schotanus et al., 1983), a transformation of the coordinate system according to the planar-fit method (Wilczak et al., 2001), and block averaging. The quality control scheme included steady-state tests and integral turbulence characteristic tests (Foken and Wichura, 1996), after which we discarded low-quality 30-min intervals based on the flag system of Mauder et al. (2013).

For the successful 30-min intervals we analysed the high frequency data as follows. First we removed implausible values, applied a despiking routine, linear interpolation of gaps up to a cumulative gap length of 1%, coordinate rotation, and demeaning. Then the signal was decomposed into contributions from small and large eddies based on the energy content for which the Fourier transform and the power spectrum were computed and Fourier coefficients with less energy than the mean energy content of the 30-min interval were set to zero. Subsequently, the inverse Fourier transform was applied to yield the time series of the large eddies and the small eddies were computed from the residual of the original time series and large eddies. The fraction of zeroed coefficients for large eddies on a campaign average over all 30-min intervals is shown in Table 1. This procedure led to similar results as an ensemble empirical mode decomposition and a separation with a critical frequency of 0.02 Hz as suggested by Gao et al. (2017). However, we believe that the mean energy threshold as used in the first method is a more rigorous criterium, because it directly relates to the aim of separating the energetic scales.

In a third step, the mean amplitudes and phase differences were computed from the uw-, vw- and wT-cross-spectra for large and small eddies separately.

	Forest	Shrubland
u	0.96 ± 0.01	0.97 ± 0.01
v	0.95 ± 0.02	0.97 ± 0.02
w	0.92 ± 0.02	0.91 ± 0.03
T	0.97 ± 0.01	0.97 ± 0.02

Table 1: The fraction of Fourier coefficients retained for small eddies for u, v, w and T (top to bottom) for the Yatir forest (left) and for the surrounding shrubland (right).

Therefor, the analytical signal $x_a(t)$ of the time series $x(t)$ was constructed from

$$x_a(t) = x(t) + i\mathcal{H}\{x(t)\} = A(t)e^{i\phi(t)}, \tag{2}$$

where $i^2 = -1$ is the imaginary unit, $A(t)$ is the instantaneous amplitude, $\phi(t)$ is the instantaneous phase, and $\mathcal{H}\{x(t)\}$ is the Hilbert transformation of $x(t)$ given by

$$\mathcal{H}\{x(t)\} = \frac{1}{\pi}\text{p.v.}\int_{-\infty}^{\infty}\frac{x(\tau)}{t-\tau}d\tau. \tag{3}$$

In analogy to the cross-spectra of Fourier (Stull, 1988) and wavelet (Torrence and Compo, 1998) transformation, the Hilbert cross-spectrum (HCS) of two time series $x(t)$ and $y(t)$ is given by

$$HCS_{xy}(t) = x_a^*(t)y_a(t), \tag{4}$$

where the asterisk denotes the complex conjugate (frequency dependency of HCS is still implied) . From the HCS a mean amplitude and a phase difference can be computed by

$$A_{xy} = \overline{(\Im(HCS_{xy}(t))^2 + \Re(HCS_{xy}(t))^2)^{1/2}} \tag{5}$$

and

$$\phi_{xy} = \overline{|\arctan\left(\frac{\Im(HCS_{xy}(t))}{\Re(HCS_{xy}(t))}\right)|}, \tag{6}$$

where $\Im$ and $\Re$ denote the imaginary and real part respectively. ϕ_{xy} is a proxy for the transport efficiency e_t defined as $e_t = |(F_{direct} - F_{back})F_{direct}^{-1}|$ where F_{direct} is the accumulation of all events in the flux contributing quadrants

and F_{back} the accumulation of the opposing quadrants (Francone et al., 2012). $\phi_{xy} \neq 0$ introduces time lags between x and y, which increases contributions from opposing quadrants, and weakens the correlation (Gao et al., 2017). A_{xy} is correlated to $\sigma_x \sigma_y = \overline{x'y'} r_{xy}^{-1}$, where σ is the standard deviation and r is the correlation coefficient, and therefore a measure of the transport energetics or hypothetical strength, independent of the efficiency or the phase difference between x and y (Stull, 1988).

2.3. Doppler Lidar measurements and data processing

Two Doppler wind lidars (Stream Line, Halo Photonics Ltd., Worcester, UK) were deployed near the ultrasonic anemometers at the shrubland and the forest site. The systems emit laser pulses, which are scattered by aerosols in the atmosphere. The line-of-sight velocity along the optical-axis is extracted from a Doppler shift in the backscattered light. Both wind lidars were operated in a vertical stare mode, from which vertical velocity profiles with a frequency of 1 Hz and a resolution of 18 m were obtained. A velocity-azimuth-display scan was performed each 30 min from which a profile of the horizontal wind speed and direction was computed with the algorithm of Browning and Wexler (1968). We averaged 15000 pulses per estimate and discarded range gates with a signal-to-noise ratio < -17 dB or below the range of 60 m to remove low quality data.

2.4. Radiation measurements

The net radiation was computed at 30-minute intervals with

$$R_n = S_\downarrow - S_\uparrow + L_\downarrow - L_\uparrow, \tag{7}$$

where $S_\uparrow$ and $S_\downarrow$ are the up- and down-welling shortwave radiation and $L_\uparrow$ and $L_\downarrow$ are the up- and down-welling longwave radiation. $S_\uparrow$ and $S_\downarrow$ were measured with two pyranometers (CMP21, Kipp & Zonen, Netherlands at both sites). $L_\uparrow$ and $L_\downarrow$ were measured with two pyrgeometers (CGR4, Kipp & Zonen at the forest site and PIR, Eppley Lab, USA at the shrubland site). The instruments at the shrubland site were positioned at the same height as the ultrasonic

anemometer (9 m a.g.l. until 23 August 2015, when it was raised to 15 m a.g.l.). At the forest site they were installed 3 m below the ultrasonic anemometer (16 m a.g.l.).

3. Results and Discussion

We compare ultrasonic anemometer measurements from the canopy sublayer of the Yatir forest with the surface layer of the surrounding shrubland to analyze differences of the turbulent transport properties. In the following, we will use superscripted l for large eddies and s for small eddies. Subscripted f refers to the forest and d to the shrubland.

3.1. Mean diurnal cycle of amplitudes and phase differences

The mean diurnal cycle of amplitudes and phase differences of small eddies for the vertical heat and momentum transport are shown in Fig. 2. At both sites the amplitudes show a pronounced diurnal cycle, while the phase difference features a constant value of 45° without a diurnal cycle. The diurnal cycle of the amplitudes is explained with stronger turbulence during the day for a radiation driven boundary layer. The phase differences are explained by isotropic turbulence at small scales (Brugger et al., 2018), which randomly distributes the phase shift between 0° and 90°, and gives further confidence in the method of determining the critical frequency. Table 2 shows, that the mean day-time amplitudes in the forest are larger than in the surrounding shrubland, which is in accordance with the expectation of stronger turbulence for the rougher surface of the forest. On the other hand the phase-difference ratio is close to unity, thus, the transport of momentum and heat at small scales is equally efficient at both sites and the larger heat fluxes of the forest site at small scales are solely caused by stronger turbulence.

The diurnal cycles of amplitudes and phase differences for large eddies are shown in Fig. 3 and the resulting day-time ratios of forest to shrubland are also given in Table 2. The vertical transport of stream-wise momentum at large

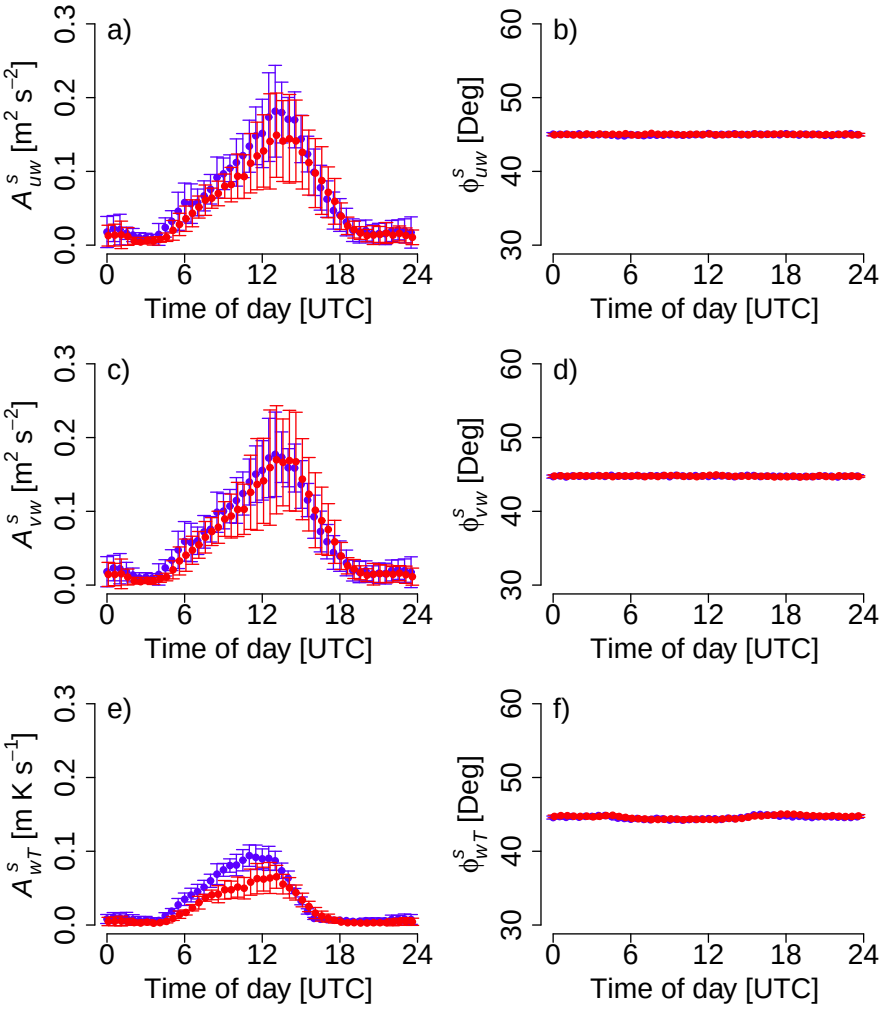

Figure 2: Comparison of the mean diurnal cycle of amplitude (left column) and phase difference (right column) for small eddies between forest (blue) and shrubland (red) from the ultrasonic anemometers. The top row shows vertical transport of stream-wise momentum, the middle row the vertical transport of cross-stream momentum, and the bottom row the vertical transport of heat. The mean values are illustrated by points and the standard deviation (a measure of the day-to-day variability) are shown as error-bars.

	$A^s_{xy,f}/A^s_{xy,d}$	$A^l_{xy,f}/A^l_{xy,d}$	$\phi^s_{xy,f}/\phi^s_{xy,d}$	$\phi^l_{xy,f}/\phi^l_{xy,d}$
$x = u$, $y = w$	1.45 ± 0.71	1.71 ± 0.75	1.00 ± 0.01	0.91 ± 0.05
$x = v$, $y = w$	1.35 ± 0.71	1.50 ± 0.67	1.00 ± 0.01	1.01 ± 0.03
$x = w$, $y = T$	1.68 ± 0.84	2.18 ± 0.81	1.00 ± 0.01	0.98 ± 0.06

Table 2: Mean ratio of the amplitudes and phase differences of forest to shrubland with standard deviation. Only day time values between sunrise and sunset were used for the calculation.

scales has larger amplitudes and smaller phase differences at the forest compared to the shrubland, indicating a more energetic and more efficient momentum transport over the forest canopy. For the cross-stream momentum the efficiency is the same for shrubland and forest, but the forest has larger amplitudes. In case of the sensible heat flux the amplitudes are larger at the forest, while the phase differences have similar values for both sites with a pronounced diurnal cycle. The decrease in ϕ^l_{wT} during the day could be explained by convective turbulence with rising warm air parcels, where positive w' and T' occur together. This result shows, that the canopy convector effect of the Yatir forest cannot be explained with a more efficient transport process for heat, but is solely generated by a more energetic transport due to stronger turbulence.

3.2. Effect of momentum transport on aerodynamic resistance

Our results indicate that a more efficient transport of heat can be ruled out as reason for the reduced r_H of the forest canopy. Therefore, we will investigate how a larger $A_{uw,f}$ and $A_{vw,f}$, and smaller $\phi^l_{uw,f}$ contribute to a reduction in r_H. The numerous parametrisations of r_H (an overview is presented by Liu et al. (2007)) feature an indirect proportionality to $\overline{u}$, which can be linked to the friction velocity (u_*) with Monin-Obukhov similarity theory ($r_H \propto u_*^{-1}$). With decreasing ϕ or increasing A of the momentum transport the u_* will increase and affect r_H subsequently. In order to quantify these effects separately relative to the reference of a hypothetical surface layer we assume (effects of small eddies are neglected):

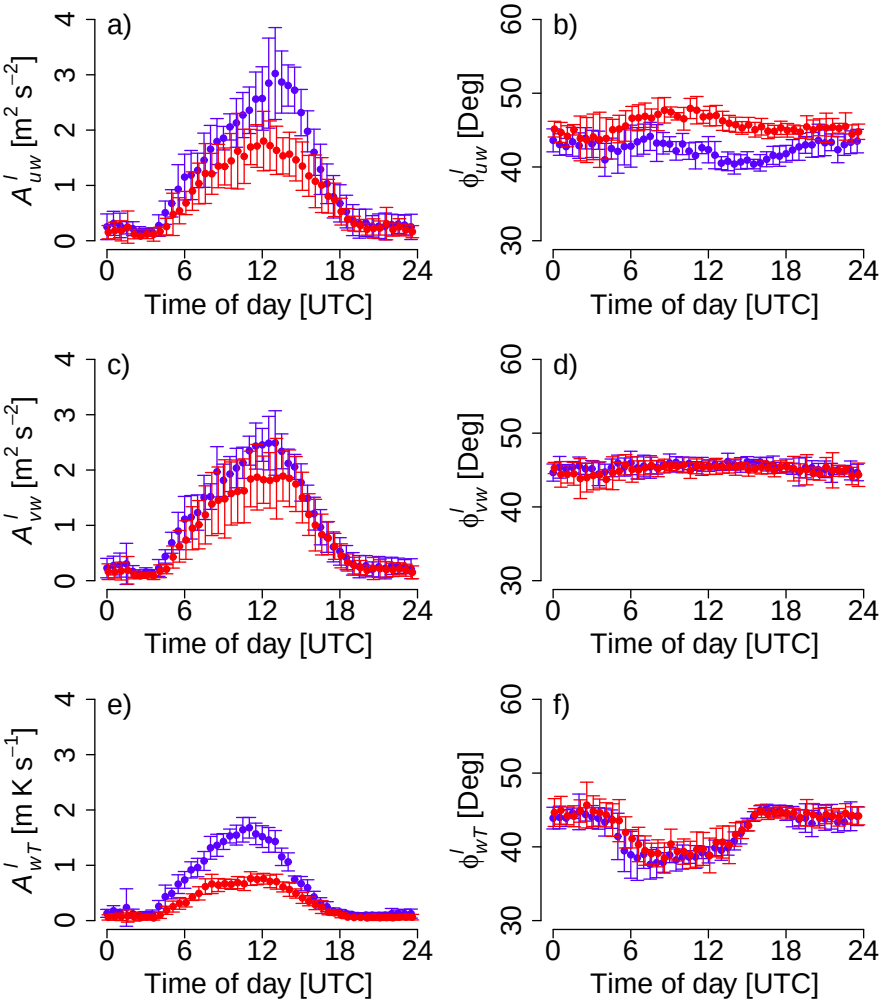

Figure 3: Comparison of the mean diurnal cycle of amplitude (left column) and phase difference (right column) for large eddies between forest (blue) and shrubland (red) from the ultrasonic anemometers. In analogy to Fig. 2, the top row shows vertical transport of streamwise momentum, the middle row the vertical transport of cross-stream momentum, and the bottom row the vertical transport of heat. The mean values are illustrated by points and the standard deviation is shown as an error-bar.

1. The forest has the same amplitudes for the momentum transport as the shrubland ($A^l_{uw,f}$ was set to $0.58 \cdot A^l_{uw,f}$ and $A^l_{vw,f}$ to $0.66 \cdot A^l_{vw,f}$) .
2. The forest has the same phase differences as the shrubland ($\phi^l_{uw,f}$ was decreased by 4.1°).

The effect on the aerodynamic resistance was then computed for each day-time 30-min interval by reconstructing a time series of $w'(t)$ that corresponds to the new A or ϕ with

$$w'(t)_{mod} = \Re\left(\frac{\widetilde{HCS}}{HCS}\mathcal{H}\{w'(t)\}\right), \tag{8}$$

where the subscribed "mod" indicates the artificially changed argument and modulus of $\widetilde{HCS}_{uw}$ (or $\widetilde{HCS}_{vw}$). Then, a corresponding u_* was computed as

$$\tilde{u}_* = (\overline{u'w'}^2_{mod} + \overline{v'w'}^2_{mod})^{1/4}, \tag{9}$$

and, lastly, the change of the aerodynamic resistance relative to a characteristic value of $r_H = 16$ s m^{-1} for the Yatir forest (Rotenberg and Yakir, 2011) was calculated based on the parametrisation of Yang et al. (2001) with the assumption of unchanged stratification and shape of the logarithmic wind profile with

$$r_H = \frac{Pr}{\kappa u_*}\left[\ln\left(\frac{z-d}{z_{0h}}\right) - \psi(\zeta, \zeta_{0h})\right] = \frac{\text{const.}}{u_*}, \tag{10}$$

where $\zeta = z/L$ is the stability parameter, d the displacement height, z_0 the roughness length, κ the von Kármán constant, and Pr the Prandl constant. On average the results of the two cases were:

1. The effect of the amplitudes reduces u_* by 23%, which in turn would increase the aerodynamic resistance by 30% . This cumulates in an increased difference between surface and air temperature by 3.5 K in order for the sensible heat flux to balance the net radiation during noon time (Eq. 1 with $\overline{w'T'} = 0.73$).
2. The effect of the phase difference of the Yatir forest to shrubland values would result in a u_* reduction by 5% and a r_H increase by 5%, which results in an increase in surface-to-air temperature difference of 0.6 K.

This finding shows that for modeling the effect of this semi-arid forest on the atmosphere, it is more important to reproduce the turbulence intensification due to the higher roughness of the canopy than the changes in turbulence structure.

3.3. Influence of the sea-breeze on the diurnal cycle

Careful inspection of the peak times of the amplitudes in Fig. 2 and Fig. 3 reveals that those are located at different times of the day. A systematic investigation of the peak times of turbulence statistics (mean, variances and covariances) allows to identify four groups (Table 3):

1. $\overline{T}$, σ_T^2, and $\overline{w'T'}$ with a peak between $1000 - 1200$ UTC (1200 - 1400 local time).
2. $\overline{u}$, σ_w^2, and $\overline{u'w'}$ with a peak between $1300 - 1500$ UTC (1500 - 1700 local time).
3. σ_v^2, $\overline{u'T'}$, and $\overline{v'w'}$ as a group in between those peaks.
4. σ_u^2 (Fig. 5a) has an especially interesting behaviour as its peak is in the early group for the shrubland site, but in the late group for the forest site.

This behaviour can be explained with the forcings by the net radiation and the background wind in combination with the different turbulence production regimes at the Yatir forest and shrubland. The net radiation reaches peak values close to the local noon time at 1000 UTC in accordance with maximum zenith angle of the sun (Fig. 4a). The surface layer wind speed has an asymmetric diurnal cycle with the maximum in the afternoon (Fig. 4b), which can be explained by a super-position of downward mixing of the north-western geostrophic wind and the delayed arrival of a sea-breeze due to the distance from the Mediterranean sea (Fig. 4c). The contribution from the geostrophic wind is assumed to be downward mixing of that constant background wind above the boundary layer, which was observed to follow the diurnal cycle of the surface temperature for a radiation driven boundary layer and weak horizontal pressure gradients (Zhang and Zheng, 2004). Therefore, we assume the background-wind contri-

Quantity	Forest	Shrubland
u	1330	1400
T	1130	1100
σ_u^2	1300	1100
σ_v^2	1130	1200
σ_w^2	1300	1430
σ_T^2	1030	0900
$\overline{u'v'}^*$	1200	1200
$\overline{v'w'}^*$	1130	1130
$\overline{u'w'}$	1300	1330
$\overline{u'T'}$	1300	1200
$\overline{v'T'}^*$	1000	0800
$\overline{w'T'}$	1100	1200

Table 3: Times of the maximum of the (absolute) mean diurnal cycle of turbulence statistics (left) for forest (middle) and shrubland site (right). The asterisks indicate quantities were day-to-day variations (standard deviation of mean diurnal cycle) were of similar magnitude as the diurnal cycle and, therefore, the maximum could be erroneous.

bution to follow a bell-shaped curve given by

$$u_{bg} = 1.5 + 2.8 * \exp\left(-\frac{(t - t_{bg})^2}{\sigma_{bg}^2}\right) \tag{11}$$

centered at temperature maximum ($t_{bg} = 11.25$, see Table 3) with a width corresponding to the length of the day ($2\sigma_{bg} = 13.2$) and empirically chosen height and off-set to match the measurements at the shrubland site (black dashed line in Fig. 4c). Alpert and Rabinovich-Hadar (2003) found that the sea-breeze arrives after 1 to 2 hours at Kirjat Gott, which is one third of the distance from the Mediterranean sea to Yatir forest. Assuming linear travel speed, the sea-breeze arrives after 4.5 hours at Yatir forest. Further, it is reported by Miller et al. (2003) that the magnitude of the sea-breeze is connected to the temperature difference between land and sea. Therefore, we assume that the contribution

from the sea-breeze follows a narrower bell-shaped curve given by

$$u_{sb} = 4.0 * \exp\left(-\frac{(t - t_{sb})^2}{\sigma_{sb}^2}\right) \tag{12}$$

with $3\sigma_{sb} = 13.2$, a maximum that is delayed by 4 hours to the temperature maximum ($t_{sb} = t_{bg} + 4$), and empirically chosen height to match the measurements (black dotted line in Fig. 4c).

Those driving mechanisms affect the four groups differently:

1. Quantities closely linked to the surface heating and buoyant production of turbulence have an early peak driven by the net radiation with possible delays due to heat storage in soil and by canopy.
2. Quantities connected to the wind speed and resulting mechanical production of turbulence have an late peak due to the delayed arrival of the sea breeze.
3. Quantities which are driven by both (wind speed and surface heating) or the redistribution of turbulent kinetic energy have their peak in the middle group.
4. The special case of σ_u^2 can be explained by the different turbulence production regimes of shrubland and forest. At the shrubland the production is buoyancy driven and redistribution of turbulent kinetic energy from the vertical is larger than the mechanical production and leads to an early peak. At the forest the mechanical production is the main source of turbulent kinetic energy and the peak is therefore in the afternoon with the arrival of the sea breeze.

3.4. Evening transition at Yatir forest

The late wind speed maximum in combination with the importance of mechanical turbulence production for the canopy convector effect lead to a faster evening transition of the boundary layer at the forest compared to the shrubland. The forest features stronger turbulence throughout the mixed layer during the day until 1300 UTC in the afternoon due to lower albedo and higher roughness

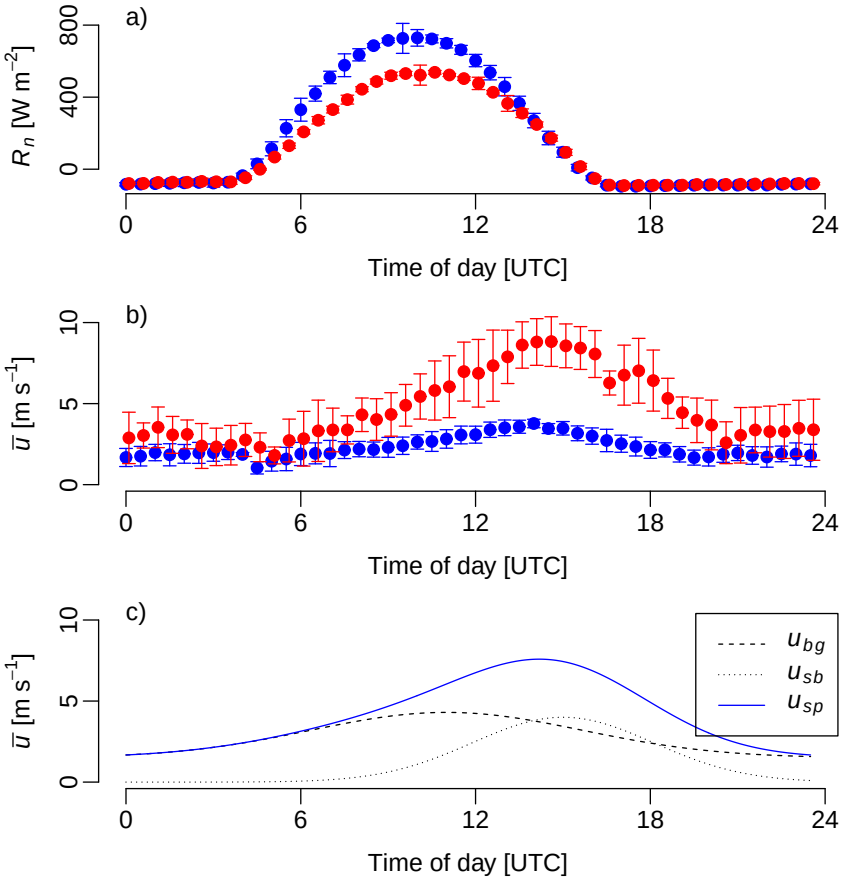

Figure 4: Top (a): Mean diurnal cycle of net radiation with the standard deviation as error-bars. The forest site is shown in blue and the shrubland site in red. Middle (b): Mean diurnal cycle of the wind speed with the standard deviation as error-bars from the eddy-covariance stations of the forest site (blue) and the shrubland site (red). Bottom (c): Simple model to explain the diurnal cycle of the wind speed (solid blue) as superposition of the downward mixing of the synoptic-background wind (black dashed) and the sea-breeze (black dotted).

(Fig. 5b). However in the afternoon the shrubland shows stronger turbulence in the mixed layer, while near the surface higher velocity variances are observed at the forest (σ_u^2 is shown in Fig. 5a, σ_v^2 is similar throughout the day for forest and shrubland (not shown), and σ_w^2 is always larger at the forest (not shown)). Moreover, the triple moment $\overline{w'w'T'}$ becomes negative at the forest in the afternoon (Fig. 5c), which can be linked to the vertical gradient of the sensible heat flux, if a gradient diffusion approximation is assumed (Katul et al., 2013):

$$\overline{w'w'T'} = -C\tau\sigma_w \frac{\partial \overline{w'T'}}{\partial z}, \tag{13}$$

where C is a similarity constant and τ is a relaxation time scale defined by the ratio of turbulent kinetic energy and its mean dissipation rate. A negative triple moment is then connected to a positive $\overline{w'T'}$ increasing with height or a negative $\overline{w'T'}$ decreasing with height. Both cases lead to a cooling of canopy sublayer at the forest and, possibly, the formation of an inversion at the interface to the advected boundary-layer from the shrubland leading to a residual layer above. This could explain the larger vertical velocity variances in the upper boundary-layer observed at the shrubland in the afternoon (Fig. 5b) and also the cooler nighttime temperatures at forest compared to its surroundings reported by Yosef et al. (2017).

4. Conclusion

A comparison of turbulent transport efficiency and energetics of the canopy sublayer of the semi-arid Yatir forest and the surface layer of its surrounding shrubland from ultrasonic anemometer measurements was presented. Based on our analysis, we draw the following conclusions:

(1) The canopy convector effect balances most of the net radiation with the sensible heat flux, while maintaining a low surface temperature at the forest site. This appears to be driven by a more energetic, but not a more efficient turbulent transport of heat at all scales compared to the shrubland. The sensible heat flux of the forest benefits from a lowered aerodynamic resistance to heat transfer due

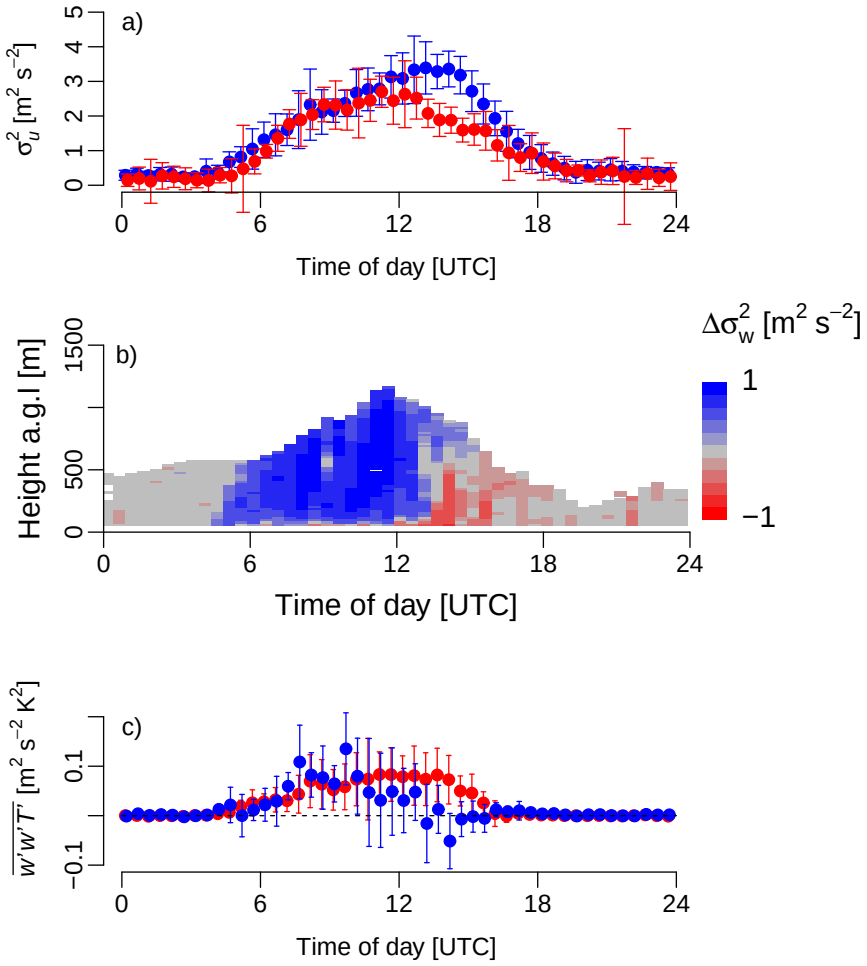

Figure 5: Top (a): Mean diurnal cycle of stream-wise velocity variance (σ_u^2) from the ultrasonic anemometer measurements with the standard deviation as error-bars. The forest site is shown in blue and the shrubland site in red. Middle (b): Time-height plot of the difference in vertical velocity variance between forest and shrubland ($\Delta\sigma_w^2 = \sigma_{w,f}^2 - \sigma_{w,d}^2$) from the Doppler wind lidar measurements. Red colors indicate larger σ_w^2 at the shrubland site and blue colors at the forest site (logarithmic spacing of the color bar to emphasis the differences). Bottom (c): Mean diurnal cycle of the triple moment $\overline{w'w'T'}$ with standard deviations as error-bars. The forest site is shown in blue and the shrubland site in red.

to a large-scale momentum transport, which has a higher energy magnitude and efficiency. However, the effect of the efficiency is smaller than the effect of the energy magnitude, thus, modelling of the surface–atmosphere exchange above the forest primarily needs to account for the increased turbulence strength that follows from higher surface roughness. The effects of the modified turbulence structure by the canopy are less important to include in modelling.

(2) The surface-atmosphere exchange of the Yatir forest is influenced by a sea-breeze that helps to delay the wind speed maximum into the afternoon. This accelerates the cooling of the forest in the afternoon and facilitates the earlier formation of a residual layer compared to the surrounding shrubland. A side effect of this temporal off-set between mechanical and buoyant turbulence production are earlier peak times for σ_T^2 and $\overline{w'T'}$ than for σ_w^2 and $\overline{u'w'}$, in case of the σ_u^2 even different between the Yatir forest (driven directly by mechanical production) and the surrounding shrubland (driven by redistribution from the buoyant production).

5. Acknowledgments

We are grateful to Gabriel G. Katul for his advice on decomposition based on the Lorenz curve. This research was supported by the German Research Foundation (DFG) as part of the German-Israel collaborative project Climate feedbacks and benefits of semi-arid forests (CliFF; grant no. YA 274/1-1 and SCHM 2736/2-1).

References

P. Alpert and M. Rabinovich-Hadar. Pre- and post-sea-breeze frontal lines – a meso-γ-scale analysis over south Israel. *Journal of the Atmospheric Sciences*, 60(24):2994–3008, 2003. doi: 10.1175/1520-0469(2003)060⟨2994:PAPFLM⟩2.0.CO;2.

T. Banerjee, F. De Roo, and M. Mauder. Explaining the convector effect in

canopy turbulence by means of large-eddy simulation. *Hydrology and Earth System Sciences*, 21(6):2987–3000, 2017. doi: 10.5194/hess-21-2987-2017.

R. A. Betts. Offset of the potential carbon sink from boreal forestation by decreases in surface albedo. *Nature*, 408(6809):187–190, 2000. doi: 10.1038/35041545.

K. A. Browning and R. Wexler. The determination of kinematic properties of a wind field using doppler radar. *Journal of Applied Meteorology*, 7(1):105–113, 1968. doi: 10.1175/1520-0450(1968)007⟨0105:TDOKPO⟩2.0.CO;2.

P. Brugger, G. G. Katul, F. De Roo, K. Kröniger, E. Rotenberg, S. Rohatyn, and M. Mauder. Scalewise invariant analysis of the anisotropic reynolds stress tensor for atmospheric surface layer and canopy sublayer turbulent flows. *Phys. Rev. Fluids*, 3:054608, 2018. doi: 10.1103/PhysRevFluids.3.054608.

E. J. Burke, S. J. Brown, and N. Christidis. Modeling the recent evolution of global drought and projections for the twenty-first century with the hadley centre climate model. *Journal of Hydrometeorology*, 7(5):1113–1125, 2006. doi: 10.1175/JHM544.1.

F. Eder, F. De Roo, E. Rotenberg, D. Yakir, H. P. Schmid, and M. Mauder. Secondary circulations at a solitary forest surrounded by semi-arid shrubland and their impact on eddy-covariance measurements. *Agricultural and Forest Meteorology*, 211-212:115 – 127, 2015. doi: 10.1016/j.agrformet.2015.06.001.

J. J. Finnigan, R. H. Shaw, and E. G. Patton. Turbulence structure above a vegetation canopy. *Journal of Fluid Mechanics*, 637:387–424, 2009. doi: 10.1017/S0022112009990589.

T. Foken and B. Wichura. Tools for quality assessment of surface-based flux measurements. *Agricultural and Forest Meteorology*, 78(1):83 – 105, 1996. doi: 10.1016/0168-1923(95)02248-1.

C. Francone, G. G. Katul, C. Cassardo, and R. Richiardone. Turbulent transport efficiency and the ejection-sweep motion for momentum and heat on sloping

terrain covered with vineyards. *Agricultural and Forest Meteorology*, 162-163: 98 – 107, 2012. doi: 10.1016/j.agrformet.2012.04.012.

Z. Gao, H. Liu, G. G. Katul, and T. Foken. Non-closure of the surface energy balance explained by phase difference between vertical velocity and scalars of large atmospheric eddies. *Environmental Research Letters*, 12(3):034025, 2017. doi: 10.1088/1748-9326/aa625b.

U. Högström and A.-S. Smedman. Accuracy of sonic anemometers: Laminar wind-tunnel calibrations compared to atmospheric in situ calibrations against a reference instrument. *Boundary-Layer Meteorology*, 111(1):33–54, 2004. doi: 10.1023/B:BOUN.0000011000.05248.47.

G. G. Katul, D. Cava, M. Siqueira, and D. Poggi. *Scalar turbulence within the canopy sublayer*, pages 73–95. John Wiley & Sons, Ltd, 2013. ISBN 9781118527191.

K. Kröniger, F. De Roo, P. Brugger, S. Hug, T. Banerjee, J. Zinsser, E. Rotenberg, D. Yakir, S. Rohatyn, and M. Mauder. Effect of secondary circulations on surface-atmosphere exchange of energy at an isolated semi-arid forest. *Boundary-Layer Meteorology*, ?(?):Under Review, 2018.

S. Liu, L. Lu, D. Mao, and L. Jia. Evaluating parameterizations of aerodynamic resistance to heat transfer using field measurements. *Hydrology and Earth System Sciences*, 11(2):769–783, 2007. doi: 10.5194/hess-11-769-2007.

M. Mauder and T. Foken. *Documentation and Instruction Manual of the Eddy-Covariance Software Package TK3 (update)*. Universität Bayreuth/Abteilung Mikrometeorologie, Bayreuth, 2015.

M. Mauder, M. Cuntz, C. Dre, A. Graf, C. Rebmann, H. P. Schmid, M. Schmidt, and R. Steinbrecher. A strategy for quality and uncertainty assessment of long-term eddy-covariance measurements. *Agricultural and Forest Meteorology*, 169:122 – 135, 2013. doi: 10.1016/j.agrformet.2012.09.006.

S. T. K. Miller, B. D. Keim, R. W. Talbot, and H. Mao. Sea breeze: Structure, forecasting, and impacts. *Reviews of Geophysics*, 41(3):1–31, 2003. doi: 10.1029/2003RG000124.

M. R. Raupach. Anomalies in flux-gradient relationships over forest. *Boundary-Layer Meteorology*, 16(3):467–486, 1979. doi: 10.1007/BF03335385.

M. R. Raupach, J. J. Finnigan, and Y. Brunet. *Coherent Eddies and Turbulence in Vegetation Canopies: The Mixing-Layer Analogy*, pages 351–382. Springer Netherlands, Dordrecht, 1996. doi: 10.1007/978-94-017-0944-6_15.

E. Rotenberg and D. Yakir. Contribution of semi-arid forests to the climate system. *Science*, 327(5964):451–454, 2010. doi: 10.1126/science.1179998.

E. Rotenberg and D. Yakir. Distinct patterns of changes in surface energy budget associated with forestation in the semiarid region. *Global Change Biology*, 17 (4):1536–1548, 2011. doi: 10.1111/j.1365-2486.2010.02320.x.

P. Schotanus, F. T. M. Nieuwstadt, and H. A. R. De Bruin. Temperature measurement with a sonic anemometer and its application to heat and moisture fluxes. *Boundary-Layer Meteorology*, 26(1):81–93, 1983. doi: 10.1007/BF00164332.

M. Sprintsin, A. Karnieli, P. Berliner, E. Rotenberg, D. Yakir, and S. Cohen. Evaluating the performance of the modis leaf area index (lai) product over a mediterranean dryland planted forest. *International Journal of Remote Sensing*, 30(19):5061–5069, 2009. doi: 10.1080/01431160903032885.

R. B. Stull. *An introduction to boundary layer meteorology*. Kluwer Academic Publishers, Dordrecht, 1988. doi: 10.1007/978-94-009-3027-8. 670 pp.

C. Torrence and G. P. Compo. A practical guide to wavelet analysis. *Bulletin of the American Meteorological Society*, 79(1):61–78, 1998. doi: 10.1175/1520-0477(1998)079⟨0061:APGTWA⟩2.0.CO;2.

J. M. Wilczak, S. P. Oncley, and S. A. Stage. Sonic anemometer tilt correction algorithms. *Boundary-Layer Meteorology*, 99(1):127–150, 2001. doi: 10.1023/A:1018966204465.

K. Yang, N. Tamai, and T. Koike. Analytical solution of surface layer similarity equations. *Journal of Applied Meteorology*, 40(9):1647–1653, 2001. doi: 10.1175/1520-0450(2001)040⟨1647:ASOSLS⟩2.0.CO;2.

G. Yosef, P. Alpert, C. Price, E. Rotenberg, and D. Yakir. Using eof analysis over a large area for assessing the climate impact of small-scale afforestation in a semiarid region. *Journal of Applied Meteorology and Climatology*, 56(9):2545–2559, 2017. doi: 10.1175/JAMC-D-16-0253.1.

D.-L. Zhang and W.-Z. Zheng. Diurnal cycles of surface winds and temperatures as simulated by five boundary layer parameterizations. *Journal of Applied Meteorology*, 43(1):157–169, 2004. doi: 10.1175/1520-0450(2004)043⟨0157:DCOSWA⟩2.0.CO;2.

Erklärung

Hiermit erkläre ich, dass ich die vorliegende Dissertation selbst verfasst habe, nur die angegebenen Hilfsmittel verwendet habe und die Grundsätze des Karlsruher Instituts für Technologie zur Sicherung guter wissenschaftlicher Praxis beachtet habe.

Garmisch-Partenkirchen, den 9. July 2018

Peter Brugger